Lee waves in IDEMIX: the effect and sensitivity of implementing a lee wave module in an internal wave model

Dissertation with the aim of achieving a doctoral degree
at the Faculty of Mathematics, Informatics and Natural
Sciences
Department of Earth Sciences
at Universität Hamburg

Submitted by
Thomas Søndergaard Eriksen

Hamburg, 2021

Department of Earth Sciences

Date of Oral Defense:

15.12.2021

Reviewers:

Prof. Dr. Carsten Eden
Prof. Dr. Dirk Olbers

Members of the examination commission:

Chair Prof. Dr. Carsten Eden
Prof. Dr. Dirk Olbers
Prof. Dr. Nedjeljka Žagar
Pd Dr. Thomas Pohlmann
Prof. Dr. Armin Iske

Chair of the Subject Doctoral Committee Earth System Sciences:

Prof. Dr. Dirk Gajewski

Dean of Faculty MIN:

Prof. Dr. Heinrich Graener

Versicherung an Eides statt | Declaration on Oath

Hiermit erkläre ich an Eides statt, dass ich die vorliegende Dissertationsschrift selbst verfasst und keine anderen als die angegebenen Quellen und Hilfsmittel benutzt habe |
I hereby declare upon oath that I have written the present dissertation independently and have not use further resources and aids than those stated

Hamburg, den	Unterschrift
16/02-2022	Thomas Eriksen

Zussamenfassung

Interne Schwerewellen bilden einen Schlüsselfaktor der Ozeanzirkulation, da ihre Brechung Impulse und Energie großskaliger Bewegungen auf kleinskalige Turbulenzen überträgt. Die internen Schwerewellen bilden so eine Hauptquelle für die Vermischung des inneren Ozeans und wirken umgekehrt auch selbst als Antrieb großskaliger Bewegungen wie etwa der meridionalen Umwälzzirkulation selbst. Hieraus resultiert ihre wesentliche Bedeutung im Klimasystem sowie weiter die Notwendigkeit ihrer Abbildung in Klimamodellen. Den größten Beitrag zur internen Wellenenergie im Innenozean leisten die barotropen Gezeiten, die durch Gezeitenströmungen am Meeresboden erzeugt werden, sowie außerdem die niederfrequenten Schwerewellen, die an der Oberfläche aufgrund von Windspannungsschwankungen entstehen. Eine andere Gattung interner Wellen, sind Leewellen, die in jüngerer Vergangenheit eine erhebliche Aufmerksamkeit erfahren haben. Leewellen werden durch geostrophische Strömungen über rauer Topographie am Meeresboden ausgelöst. Während interne Gezeiten und Trägheitswellen bereits in vielen Ozeanmodellen als Grenzantrieb verwendet werden, bilden moderne Ozeanmodellen den Leewellenantrieb nicht ab, obwohl angenommen wird, dass er erhebliche Energiemengen für die Durchmischung in Schlüsselregionen des Ozeans liefert.

Die mit der internen Schwerewellenbrechung verbundene vertikale Vermischung findet jedoch auf zu kleinen Skalen statt, um in Ozeanmodellen aufgeschlüsselt zu werden und muss daher parametrisiert werden. Das interne Wellenmodell IDEMIX (Internal Waves, Dissipation, Energy and MIXing) beschreibt die Erzeugung, Ausbreitung und anschließende Brechung interner Schwerewellen basierend auf der Erhaltung der Wellenwirkung. Es berechnet damit direkt Diffusivität und Dissipationsraten der turbulenten kinetischen Energie (TKE) aus der internen Schwerewellenenergetik unter Berücksichtigung aller Energiequellen und -senken des Prozesses. Das Modell eignet sich so ideal als Bestandteil von Ozeanmodellen, die nach Energiekonsistenz streben. Diese Doktorarbeit zielt auf eine Beschreibung der Implementierung, Auswirkungen und Empfindlichkeit einer Leewellenkomponente in IDEMIX ab. Das Leewellenfeldist in IDEMIX als ein eigenes Energieabteil implementiert, gekoppelt an das "hintergründige" interne Wellenfeld und den mittleren Fluss über Energieübertragung. Der Vergleich der Ergebnisse eines nichtwirbelauflösenden Modells mit denen eines wirbelauflösenden Modells zeigt eine große Empfindlichkeit der Lee-Wellenerzeugung gegenüber der Modellauflösung.

Eine Erhöhung des Leewellenenergieflusses am Boden um einen Faktor von 25 resultiert/korreliert in einer Zunahme der horizontalen Modellauflösung von 2° auf 1/10°.Dies resultiert (Grund hierfür o.ä.) in großen Teilen aus erhöhten Meeresbodengeschwindigkeiten und somit auf einem Leewellenenergiefluss in Regionen, welche mit dem aufgelösten Wirbelfeld? verbunden sind.

In hochauflösenden Modellen ist das Leewellenfeld in der Lage, Impulse aus der mittleren Strömung zu extrahieren, was zu Geschwindigkeitsabnahmen von bis zu $0,1 m/s$ in Bodennähe führt, von denen einige über einen Großteil der Wassersäule anhalten können. Darüber hinaus können die Leewellen durch die Erhöhung der internen Hintergrundwellenenergie um bis zu einem Faktor von fünf in einigen Regionen die Diffusivität um eine ganze Größenordnung erhöhen. Obwohl der Großteil der Leewellenenergie unterhalb von $3000 m$ Tiefe liegt, treten solch großen Diffusivitätszunahmen hauptsächlich im Inneren und nicht in Bodennähe auf.

Obwohl die Leewellen einen signifikanten Einfluss auf die mittlere Strömung und Diffusivität haben, zeigen Sensitivitätsexperimente, dass die Leewellenerzeugung sowohl von Vereinfachungen in der Darstellung der Topographie als auch von kritischen Begrenzerfunktion im Leewellenmodul weitgehend unbeeinflusst ist. Eine Ausnahme davon bildet die Bodenspannung, aber hier werden die Unterschiede zwischen den Experimenten gemildert, wenn die vertikale Dimension der Spannung berücksichtigt wird. Während Variationen dieser sogenannten Topographieparameter das Leewellenfeld nicht wesentlich beeinflussen, ist es sehr empfindlich gegenüber Variationen in den IDEMIX-Schlüsselparametern, die den Energietransfer vom Leewellenfeld zum internen Hintergrundwellenfeld bestimmen. Ein starker Anstieg der vertikal integrierten Leewellenenergie aufgrund von Änderungen der IDEMIX-Parameter führt auch zu einem starken Anstieg der durch die Leewellen verursachten vertikal integrierten Spannung.

Darüber hinaus beeinflussen Wechselwirkungen zwischen Leewellen und mittlerer Strömung im Südlichen Ozean das vertikale Profil der Leewellenenergie, was die Behauptungen früherer Studien untermauert, dass Schwerenwelle-mittlerer Strömungswechselwirkungen ein Grund für die Diskrepanzen zwischen vorhergesagter und beobachteter Durchmischung im Südlichen Ozean sein können. Die von IDEMIX modellierten Dissipationsraten von TKE im Südlichen Ozean stimmen mit den Schätzungen aus Beobachtungen überein.

Abstract

Internal gravity waves are a key component in ocean circulation, because of their ability to transfer momentum and energy from large scale motions to small scale turbulence via their breaking. As such, they constitute a major source of interior ocean mixing, and thus in turn act as a driver of large scale motions, such as the meridional overturning circulation, themselves. They are therefore of great importance in the climate system, and hence is also their representation in climate models. The largest contributors of internal wave energy in the interior ocean are the internal tides generated by tidal flow at the bottom, and inertial waves generated at the surface due to wind stress fluctuations, but another class of internal waves, which has received substantial attention in recent years, are lee waves. These are formed by geostrophic currents over rough topography at the bottom. While internal tides and inertial waves are used as boundary forcing in many ocean models, lee wave forcing is not included in even state of the art ocean models, despite being hypothesized to provide significant amounts energy for mixing in key regions.

This mixing associated with internal gravity wave breaking takes place on scales to small to be resolved in ocean models, though, and it must therefore be parameterized. The internal wave model IDEMIX (Internal waves, Dissipation, Energy and MIXing) describes the generation, propagation and subsequent breaking of internal gravity waves based on the conservation of wave action, and thereby calculates diffusivity and dissipation rates of turbulent kinetic energy (TKE) directly from internal wave energetics, accounting for all energy sources and sinks in the process. This makes the model an ideal component ocean models striving for energy consistency.

In this PhD thesis, I aim to describe the implementation, effects, and sensitivity of a lee wave component in IDEMIX. The lee wave field is implemented as an energy compartment in its own within the framework of IDEMIX, coupled to the "background" internal wave field and the mean flow via energy transfer terms. Comparing results from a non-eddy resolving model with those from an eddy-resolving one reveal a large sensitivity of lee wave generation to model resolution. An increase in lee wave energy flux at the bottom by a factor of 25 is found with an increase in the horizontal model resolution from 2° to $1/10^\circ$. This is in large part due to increased bottom speeds and thus lee wave energy flux in regions associated with the resolved eddy field.

In high-resolution models the lee wave field is able to extract momentum from the mean flow resulting in velocity decreases of up to $0.1 m/s$ near the bottom, some of which can persist throughout much of the water column. Furthermore, by in-

creasing the background internal wave energy by up to a factor of five in some regions, the lee waves are able to increase the diffusivity by an entire order of magnitude. Even though the bulk of the lee wave energy is situated below $3000m$ depth, such large diffusivity increases occur mainly in the interior and not near the bottom.

Despite the lee waves having a significant impact on the mean flow and diffusivity, sensitivity experiments indicate, that lee wave generation is largely unaffected by both simplifications in the representation of topography and by the critical limiter function in the the lee wave module. An exception to this is the bottom stress, but differences across experiments here are alleviated if the vertical dimension of the stress is taken into account. While variations in these so-called topography parameters do not significantly affect the lee wave field, it is highly sensitive to variations in key IDEMIX parameters determining the energy transfer from the lee wave field to the background internal wave field. A large increase in the vertically integrated lee wave energy due to changes in the IDEMIX parameters, also results in large increases in the vertically integrated stress caused by the lee waves.

Additionally, lee wave-mean flow interactions in the Southern Ocean affects the vertical profile of lee wave energy, substantiating claims by previous studies that wave-mean flow interactions can be a reason for the discrepancies between predicted and observed mixing in the Southern Ocean. Dissipation rates of TKE in the Southern Ocean modelled by IDEMIX are in accordance with observational estimates.

Contents

Chapter 1

Introduction

The purpose of this section is to familiarize the reader with both the theoretical concepts and the background knowledge, which is important to set the research carried out into perspective. It will focus on why the study of lee waves is important, what the current state of knowledge is, and what further research should elucidate. Upon reading this section, it should therefore be clear why the field of lee waves remains an important research topic, but also why we already know they play a role in the world oceans.

1.1 Overturning circulation

The meridional overturning circulation is an important component of the large scale ocean circulation. Energy exchange between the ocean and the atmosphere, and the ability of the ocean to ventilate itself are the primary ways in which the ocean affects global climate. In the Atlantic Ocean the northward heat transport reaches $1.2PW$ ($1PW = 10^{15}W$) at $25°N$ (Hall and Bryden, 1982). This heat contributes substantially in shaping the climate of northern and western Europe through interaction with the lower atmosphere (Toggweiler and Key, 2003). North Atlantic Deep Water (NADW) is formed at specific locations in the Northern Atlantic and Labrador Sea is then transported southward again through the Deep Western Boundary Current (DWBC). Although the overturning circulation is a mathematical definition, and therefore doesn't say anything about its own controlling physical mechanisms, it is a key component of the understanding of the role of the ocean in global climate. The concept of an overturning circulation is most easily understood by Sandström's theorem. Sandström made tank experiments using heating and cooling sources at different places on the tank. He found that a (vertical) circulation cannot take place if the heating and cooling sources are located at the same depth. For a circulation to form the cooling must be located at a lower pressure (i.e. shallower depth) than the heating. In the real ocean, however, the water is warmed and cooled at same depth; at the surface. The stability of an overturning was examined by the classic Stommel box model (Stommel, 1961). In this study it was found that the circulation can be driven by buoyancy differences caused either by temperature or salinity differences. An interesting aspect about the Stommel box model is that it assumes the boxes to be mixed already by an external force (Stommel himself explicitly calls the boxes "stirred vessels" and has drawn propellers in his diagram). Such an external force does not exist in the real world, but the study shows that an overturning circulation needs a mixing force, even though this was not the intention of Stommel himself. Stommel and Sandström thus have in common that they did not account for internal mixing of the ocean (they were probably not aware of its existence). The imposing question is then: how is the water vertically mixed or ventilated?

Two theories are central to the answer to that question. The first one is that the Ekman transport driven by the wind stress over the Southern Ocean causes the upwelling to outcrop in the southern part of the Southern Ocean (Toggweiler and Samuels, 1995). This is due the specific topography and geography of the Southern Ocean. It is the only place on Earth (except the Arctic Ocean) where there are no zonal boundaries in the form of land. The curl of the wind stress dictates that no net meridional transport can occur above the highest point of the ocean bottom (which is in the Drake Passage) (Pedlosky, 2013). The second theory is that diapycnal mixing, which is omnipresent in the interior of the ocean, stirs the ocean to be vertically mixed. This diapycnal mixing is largely due to the breaking of internal gravity waves (Munk and Wunsch, 1998; Kunze and Smith, 2004).

In the real world the vertical-meridional circulation is referred to as the meridional overturning circulation (MOC). It is, obviously, much more complicated than the idealized concepts described above. First and foremost, it is a three dimensional system made up by distinct currents and bodies of water. The wind driven upwelling in the Southern Ocean plays a substantial part of it, but so does diapycnal mixing across the interfaces of the different water masses thereby transforming them. A detailed description of the global overturning and the driving mechanisms behind it can be found in Talley (2013) but a schematic overview of how different water masses and currents interact is shown in Fig. 1.1. The overturning here is centered on the Southern Ocean, which plays a key role by linking the Pacific, Atlantic and Indian Oceans. Both the deep water formed in the Pacific, Indian, and North Atlantic rise towards the surface in the Southern Ocean, while the Antarctic bottom water is formed here but flows into both Pacific, Indian and Atlantic Oceans, where it rises to more intermediate depths.

The Southern Ocean is thus recognized as a key region for the overturning. It is characterized by the aforementioned zonal boundary-free geography, the Antarctic Circumpolar Current (ACC) with its vigorous eddy field driven by strong westerlies, and its linkage of the Pacific, Atlantic and Indian Oceans (Talley, 2013; Rintoul and Garabato, 2013). An increase in the overturning circulation, as a response to stronger westerlies over the Southern Ocean and thus a stronger upwelling, has also been hypothesized (Toggweiler, 2009) along with an increase in heat and carbondioxide uptake by the SO (Russell et al., 2006). An increase in eddy activity rather than a stronger overturning have also been argued as a more likely result of a higher Southern Ocean wind stress (Jochum and Eden, 2015; Munday et al., 2013). This phenomenon of an increase in eddy kinetic energy as a response to stronger wind

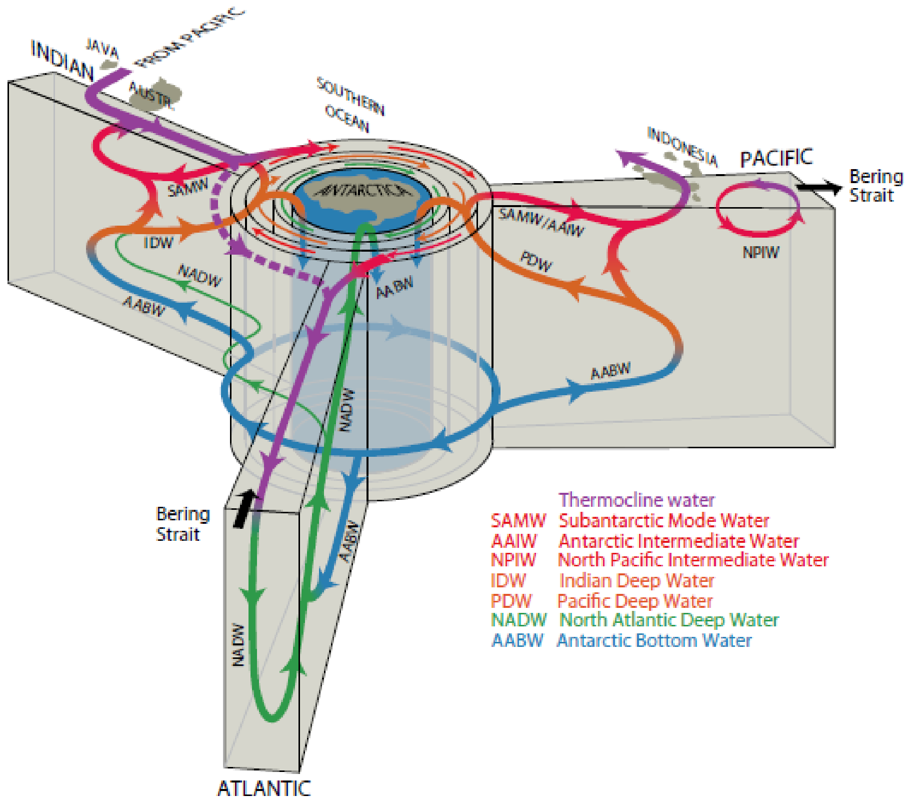

Figure 1.1: The global overturning circulation centered on the Southern Ocean (Talley, 2013), where both Pacific, Indian and North Atlantic Deep water rises towards the surface, and Subantarctic MODE Water flows into the three oceans, and Antarctic Bottom Water is formed. In the Pacific, Atlantic, and Indian Ocean the Antarctic Bottom Water mixes with the respective deep water via internal mixing.

forcing is known as eddy compensation (Johnson and Bryden, 1989).

Which of the two proposed mechanisms, the Ekman driven upwelling or the internal wave driven mixing, controls the MOC as the main driver is still under debate, but the overall consensus is that both add a significant contribution (Kuhlbrodt et al., 2007; Talley, 2013)

1.2 Internal gravity waves

Internal gravity waves are oscillatory motions in a (density-)stratified ocean. In the ocean they are omnipresent and can be excited in a number of different ways. They are characterized by a vertical wavelength ranging from a few meters to a few kilometers (horizontal wavelengths can reach a few hundred kilometers), and a frequency between the local Coriolis frequency, f, and the local buoyancy frequency, N. The dispersion relation sets the relation between the wave number and the frequency

$$\omega^2 = \frac{N^2 k^2 + f^2 m^2}{k^2 + m^2}$$

where ω is the frequency, $k = \sqrt{k_1^2 + k_2^2}$ is the magnitude of the horizontal wavenumber vector, and m is the vertical wavenumber. The frequency is set by the angle of propagation with the horizontal plane, and given the generation site as a point source the group velocity will be directed along the surface of a cone with the phase velocity perpendicular to the surface (Sarkar and Scotti, 2017). The presence of internal gravity waves is, as mentioned, a substantial factor in shaping the overturning circulation, but also affects such diverse fields as nutrient transport (Wong et al., 2012; Leichter et al., 2003) and the shaping of continental slopes by sediment transport (Cacchione et al., 2002).

Despite their broad range of wavenumbers and ways to be excited, the energy density spectrum of internal gravity has been observed to have a near universal shape; the so-called Garrett-Munk (GM) spectrum after Garrett and Munk (1972). Although the GM model is used as a reference in many studies, pitfalls in its methods and deviations from the spectrum have also been put forward (for instance by Wunsch (1975) and Polzin and Lvov (2011)). The reason we can observe this near universal shape is still debated among oceanographers today, although it is believed largely to be the result of non-linear wave-wave interactions (McComas, 1977; Lvov and Tabak, 2001), which tend to transfer energy from small to high wavenumbers (Olbers, 1976). When the horizontal velocity, U, becomes sufficiently large or the vertical scale of the flow becomes comparably small the local stratification will become unstable, $N^2 < 0$, which results in convective instability, or the shear of the flow becomes large enough to infer a shear instability. In both instances this leads to turbulent mixing (Sarkar and Scotti, 2017). A way to think of internal gravity waves is therefore as a bridge between motions taking place on large and small scales respectively.

1.2.1 Generation of internal gravity waves

Two sources of internal wave energy in the ocean, which have received a lot of research attention, are the fluctuating winds at the surface and the tides at the bottom. Fluctuations in wind stress at the ocean surface generate inertial motions in the mixed layer ocean, which in turn leads to pressure gradients at the mixed layer base. This produces near-inertial gravity waves propagating downwards into the interior ocean (D'Asaro, 1985; Gill, 1984). The winds at the surface ocean produce an estimated energy input of $0.3 - 1.4 TW$ (Alford, 2001; Watanabe and Hibiya, 2002; Jiang et al., 2005; Rimac et al., 2013), but only a small fraction of about $10 - 15\%$ of it leaves the mixed layer for the interior ocean as near-inertial internal waves (Rimac et al., 2016). The tidal energy depends on both the gravitational pull of the Moon and the Sun, why the most clear signals are called the M2 and S2 tides. When the Moon and the Sun are aligned (roughly every 14 days) their combined pull produces very strong tides, and when they are at a right angle the tides are not so strong (spring-neap-cycle). Flowing over topographic obstacles at the seafloor, these barotropic tides generate disturbances in the density field, which radiate away from the obstacles as internal waves. Jayne and St. Laurent (2001) estimate a dissipation of $1TW$ at depths greater than $1000m$ using a parameterization of internal waves, Nycander (2005) directly calculated a tidal forcing of $1.2TW$ at depths greater than 500 meters using linear wave theory, while Jayne and St. Laurent (2001) estimated about $1TW$ of tidal energy to be dissipated in the deep ocean from satellite altimeter data. An estimate of about $1TW$ of tidal bottom forcing, thus seems like a robust estimate. Another way in which internal gravity waves are generated is when not the tidal, but the geostrophic current flows over such topographic features. In the same manner as the tidal current, this also creates density perturbations on the lee side of such an obstacle, hence the name lee waves. Pioneering work on this subject was made by Bell (1975). When a water parcel flows geostrophically upwards along a slope and thereafter downwards on the lee side, its velocity will be lower on upward side, since it is doing work against a buoyancy force, and higher on the lee side, since it moving in the same direction as the buoyancy force. This difference in velocity creates a pressure difference; higher pressure on the upward side and lower pressure on the lee side. So over the hill there is a net horizontal force. This results in an equal force from the bottom on the water parcel, which manifests itself in a vertical flux of horizontal momentum away from the bottom. A schematic (although simplified) overview of internal wave generation is shown in Fig. 1.2.

1.2.2 Lee waves

From the linearized equations of motions Bell (1975) calculated wave stress and wave energy flux associated with such a geostrophic current flowing over topographic obstacles. A boundary condition to the linearized equations, is that the flow at the bottom must be along the (sloping) bottom and therefore the solution to the equations will always be a linear transformation of the bottom topography.

In the atmospheric literature, these waves are called 'mountain waves' (Teixeira, 2014), and can be observed as downslope winds and lenticular clouds. Their importance in large-scale numerical weather prediction have long been recognized (Palmer et al., 1986). The interest in oceanic lee waves began to increase after near bottom intensification of ocean mixing was observed by Naveira Garabato et al. (2004), who highlighted the interplay of deep-reaching currents and rough bottom topography. In a regional high-resolution model forced by winds Nikurashin et al. (2013) estimates an energy density (in wavenumberspace) two orders of magnitude larger compared to that of a flat bottom using a randomly generated, multichromatic representation of the bottom topography. Compared to their flat bottom experiment, where the wind energy input is removed by and large by a quadratic bottom drag, the energy in the rough topography simulation is removed by subgrid

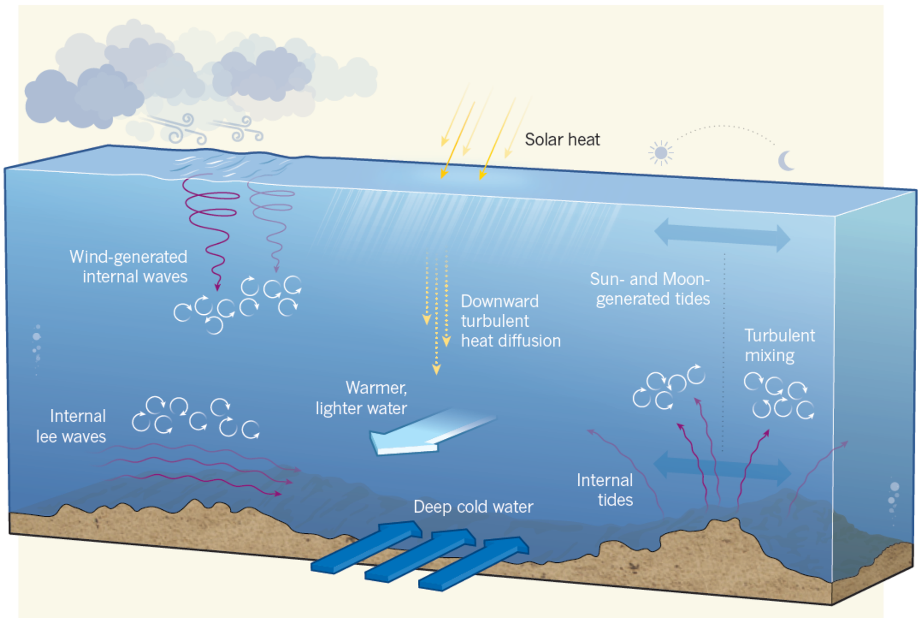

Figure 1.2: A schematic overview of sources of internal wave generation and interior ocean mixing taken form MacKinnon (2013).

scale processes, i.e. turbulent mixing.

Properly mapping of the bottom topography is thus a crucial part in assessing the contribution of lee waves (and therefore internal waves in general) in interior diapycnal mixing in global ocean general circulation models. Bell (1975) notes that geostrophic currents are mostly modulated by topographic features characterized by a horizontal extent of less than a few tens of kilometers; those classified as abyssal hills. Goff and Jordan (1988) propose a so-called topography spectrum to capture the distribution of such features. The spectrum is based on a statistical model and is characterized by a few parameters; the topographic wavelength in both horizontal directions (or inversely, the topographic wavenumbers), the root-mean-square height of the abyssal hills, and the so-called strike angle measured from true North. Indeed, following the work of Bell (1975) a measure of the height, breadth, and width of a given topographic feature on the ocean floor is needed in order to estimate the energy transferred from the mean flow impinging on such a feature into the generated lee waves. Goff and Arbic (2010) used an empirical relationship between paleo-spreading rate data and abyssal hill roughness to determine these parameters. This would need to be modified by a sedimentation data, since sedimentation acts to smoothen rough seafloor topography (Goff and Jordan, 1988; Whittaker et al., 2013). On the other hand Goff (2010) used small-scale altimetric gravity variability which also accounts for sedimentation over time. This latter approach has the advantage of already taking sedimentation cover into account, and it turns out that it is also able to map an area roughly 45% larger than the spreading rate based one.

Another parameter important for lee wave generation is the Froude Number, defined as the ratio of the geostrophic velocity to the buoyancy frequency times the height of the topography, $Fr = U/HN$. In a 2D high-resolution, idealized setup with parameters representing Drake Passage, Nikurashin and Ferrari (2010b) investigate the effect of lee wave generation as a function of the Froude Number (they refer to the Froude Number as the steepness parameter, since it also indicates the ratio of the topographic slope to the slope of the internal wave phase lines). They conclude that internal waves generated by a geostrophic rather than tidal current over rough topography can infer diapycnal mixing rates increased by more than two orders of magnitude near the bottom. This work was extended by an accompanying study where the theoretical work was applied to lowered acoustic Doppler current profiler, CTD, and topography data from the Southern Ocean (Nikurashin and Ferrari, 2010a). They estimate a total energy dissipation of $0.5-3.9mWm^{-2}$ in a section roughly 35° west of Drake Passage and $14-42mWm^{-2}$ in a section in Drake Passage, with roughly half of this energy dissipates locally in the bottom kilometer of the ocean. Application of the Bell theory to the global ocean GCM's has estimated the global integrated energy flux from the mean flow to lee waves at $0.2-0.79TW$ (Nikurashin and Ferrari, 2011; Scott et al., 2011; Trossman et al., 2013; Wright et al., 2014). The fairly large differences between these estimates are mostly due to the different bottom velocities and different topographic spectrum used to predict the energy flux. Integrating the Goff and Jordan (1988) spectra over the second topographic wavenumber to obtain a one-dimensional spectrum and fitting it to echo sounding data, Nikurashin and Ferrari (2011) arrive at a global energy flux of 0.2TW. Using a 1/12 degree resolution ocean GCM along with the Goff and Arbic (2010) topography data Trossman et al. (2013) obtains a global energy flux of roughly 0.45TW. Assuming all energy dissipate locally, they compare two different schemes of lee wave energy; the Bell scheme mentioned previously and the Garner scheme (Garner, 2005). The difference in energy flux between the two are roughly 10% with a very similar spatial pattern. Comparing the lee wave drag on the mean flow with a quadratic bottom drag, they find an increase of about 55% when using both rather than only the bottom drag. This has significant effect on the bottom kinetic energy and stratification. Furthermore, their offline estimate of the lee wave energy flux calculated from the average velocities in the bottom 500m in the simulation without lee wave drag amounts to 1.2TW when globally integrated. This suggests two things; first of all that bottom velocities have a larger effect on lee wave energy flux than stratification, second of all that there is an internal negative feedback in the lee wave generation process. This feedback is relatively straight forward: a stronger bottom flow leads to a higher lee wave generation, which extracts the kinetic energy from the mean flow and consumes it by vertically mixing the water column, so that the stratification is lowered. Both of these effects (lower kinetic energy and lower stratification) will in turn lower the lee wave generation itself. This mechanism is also mentioned by Melet et al. (2015) who investigate future lee wave energy flux as a response to different climatic scenarios. They use a non-eddy resolving GFDL climate model and a parameterization of eddy kinetic energy (Eden and Greatbatch, 2008;

Marshall and Adcroft, 2010) to calculate the lee wave energy flux, and find first of all an overall decrease in lee wave energy flux in future climate scenarios as compared to preindustrial conditions and second of all a clear seasonal cycle with maximum in southern hemisphere summer.

The Southern Ocean has frequently been highlighted for its importance in lee wave driven mixing (Nikurashin and Ferrari, 2010a; Melet et al., 2014). The deep reaching eddies provide a strong bottom flow and the topographic data suggests a rough bottom with plenty of abyssal hill structure (Goff, 2010) which generate lee waves. With the previously mentioned reported increase in the westerlies the future of lee wave driven mixing in the Southern Ocean poses a relevant research topic. Lee waves have also been shown to affect the overturning circulation significantly by providing energy for a sustained water transformation in the lower cell of the MOC (Nikurashin and Ferrari, 2013), and by a lightening and increase in strength of the lower cell of the MOC along with a warming of $0.2° - 0.3° C$ of the abyssal ocean (Melet et al., 2014). The combined findings of Melet et al. (2014), Melet et al. (2015) and Scott et al. (2011) clearly calls for an inline calculation of lee wave energy flux in ocean models rather than an offline diagnostic.

Despite these calls for the inclusion of lee waves in ocean models, direct observations of lee waves are extremely sparse due to their complex nature and their intermittency in both time and space. Due to the lack of observational data, the route from lee wave generation to ocean mixing is poorly understood and likewise constrained in models (Legg, 2021). Most efforts to observe them or their effect have been dedicated to the Southern Ocean.

1.2.3 Energy transfer and dissipation

Once internal gravity waves have been generated, they freely propagate in the ocean, as long as their frequency is larger than the local Coriolis frequency, f, and smaller than the local stability frequency, N. Along the way they can exchange energy with both other waves and the mean flow. The exchange with the mean flow can have either sign and is reversible if the wave is reflected at surface or bottom, as long as the wave does not brake underway (Boyd, 1976), whereas the exchange with other waves are usually non-linear and very complex (Eden et al., 2019). These interactions infer a downward cascade of energy transfer within the internal wave spectrum from large to small scale motions, and non-linear theory predicts a transfer of energy between three interacting waves when the conditions

$$\omega_0 = \omega_1 \pm \omega_2$$
$$\mathbf{k_0} = \mathbf{k_1} \pm \mathbf{k_2}$$

are met. Three mechanisms were identified by McComas and Bretherton (1977) for this downward energy cascade to take place. One is parametric subharmonic instability (PSI). This refers to a triad wave interaction, where energy is transferred from a wave with large frequency and small wavenumber to two waves with nearly half the frequency and opposite wavenumbers. The amount of energy transferred is proportional to the energy of the larger wave. MacKinnon et al. (2013) presented observational evidence of this from the Pacific Ocean near $29° N$ where the tidal frequency is close to the double of the inertial frequency. Induced diffusion (ID) describes the transfer of energy from a high frequency, large wavenumber wave encountering a low frequency, small wavenumber second wave to a nearly identical large wavenumber, high frequency third wave. The third mechanism, elastic scattering, transfers energy between an upward and a downward propagating wave with nearly the same frequencies and nearly opposite vertical wave numbers encountering a third low frequency, nearly vertical wave. Eden et al. (2019) numerically evaluate energy transfers in wavenumber space by nonlinear wave-wave interaction with three different methods (of increasingly computational costs) and finds reasonable agreement with the parameterization by McComas and Müller (1981) derived for PSI and ID only.

As energy is transferred towards higher and higher wavenumbers, the velocity shear over the wave amplitude can become so large that it leads to shear instability (this is depicted as Kelvin-Helholtz billows by Smyth et al. (2001)), or the local stability frequency becomes negative leading to convective instability (Sarkar and Scotti, 2017); in other words, the wave will break and the water column will be mixed.

1.3 Ocean Mixing

Ocean mixing is usually defined as the irreversible process through which two or more water masses are mixed to one. Before the mixing there are two (or more) water masses and after the mixing there is one. At the molecular scale mixing is characterized as molecular diffusion, which is an inherent physical quality of all fluids. If you leave two water masses of different density at rest but in contact, eventually they will mix because of molecular diffusion.

If a large body of water is moving with the right flow characteristics, however, mixing can also take place within the body of water as an inherent consequence of the flow characteristics. A usual distinction in fluid dynamics is that between laminar and turbulent flows. In the former the flow is smooth and constant and it is dominated by internal viscous forces, whereas in the latter the flow is chaotic, produces swirling motions called eddies and is dominated by inertial forces. The distinction between these two types of flow is done via the Reynold's Number, which signifies the ratio of inertial forces to internal viscous forces. Turbulent flows thus have a high Reynold's Number, whereas laminar flows have a low one. The eddies associated with turbulent flows act to increase (velocity and tracer) gradients and therefore also molecular mixing. An intrinsic effect of turbulent flow is thus, that it increases both the molecular mixing (via sharper gradients) and also introduces turbulent mixing itself. Another distinct feature of the eddies associated with turbulent flows is that they easily become unstable, breaking up into smaller eddies thereby transferring their energy to smaller and smaller scales and in the end to internal energy, i.e. heat (Richardson, 1920).

Mixing can also be obtained from a mechanical input, though. In the real world oceans, winds mix the surface layers and, as mentioned, tides and geostrophic motions provide energy at the bottom. In the interior ocean, mixing is commonly associated with the breaking of internal gravity waves (Polzin et al., 1997; Wunsch and Ferrari, 2004). In contrast to molecular mixing, the mixing produced by eddies and internal gravity waves is referred to as turbulent mixing. It can be observed through fine- and microstructure measurements (Polzin et al., 1995; Oakey, 1982), in which disciplines the most important quantities to be familiar with are the dissipation rate of turbulent kinetic energy (TKE) - - ϵ, and the diapycnal diffusivity, κ_ρ. Microstructure processing provides centimeter-scale measurements of the vertical shear of velocity, from which the dissipation rate of turbulent kinetic energy is calculated as

$$\epsilon = \frac{15}{2}\nu\overline{\left(\frac{\partial u}{\partial z}\right)^2}$$

where ν is the molecular viscosity and u is the velocity (Oakey, 1982; Sheen et al., 2013; Waterman et al., 2013). Finestructure measurements are obtained from CTD (conductivity, temperature and depth) and LADCP (lowered acoustic Doppler current profiler) casts and have a vertical resolutions of $\mathcal{O}(1m)$ and $\mathcal{O}(10m)$ capturing internal waves, and they calculate the TKE dissipation rate based on the velocity shear and the vertical change of isopycnal displacement; the strain. As such the finestructure method of calculating implicitly assume internal gravity waves to be the source of TKE dissipation. The diapycnal diffusivity, κ_ρ, is calculated using the dissipation rate

$$\kappa_\rho = \frac{\Gamma\epsilon}{N^2}$$

where Γ is the mixing efficiency, i.e. the amount of energy effectively acting to mix the fluids. The mixing efficiency is usually taken to be $\Gamma = 0.2$, although the notion that this value is constant throughout the entire ocean is contested (De Lavergne et al., 2016). This equation is known as the Osborn-Cox relation after Osborn and Cox (1972). It relates a shear production of TKE with a turbulent buoyancy flux and the dissipation rate of TKE by assuming a steady state conservation. The turbulent buoyancy flux is assumed downgradient, and assuming a fixed mixing efficiency amounts to assuming the ratio of the shear production and the buoyancy flux constant. As such, the Osborn-Cox relation can be interpreted as a local budget of turbulent kinetic energy.

In addition to mixing caused by internal waves generated from the interaction between the bottom geostrophic current and abyssal hills, Klymak (2018) estimates a dissipation resulting from mean flow over large scale topographic features. Under linear theory, topographic features with $k < f/u_0$ will not generate internal waves because the topographic wavenumber is not sufficiently large (or the flow not sufficiently strong), the disturbances in the velocity and buoyancy fields are evanescent. But for flows with inverse Froude number larger than unity (the so-called large-scale abyssal hills) Klymak (2018) argues that dissipation due to these evanescent perturbations is underestimated by up to a factor of two in high resolution models.

1.3.1 Observations of ocean mixing

Munk (1966) found that if diapycnal diffusion is to sustain a deepwater formation of $30Sv$ ($1Sv = 10^6 m^3/s$), an ocean average value of $\kappa_\rho = 10^{-4} m^2/s$ is needed.

Later observational campaigns were not able to find diffusivities in the interior ocean so large. Values that were an order of magnitude lower than the canonical Munk value were common (Ledwell et al., 1993, 1998). Diapycnal diffusivities larger than $K_\rho = 10^{-3} m^2/s$ near the ocean floor have later been observed while in the process highlighting the breaking of internal gravity waves as the main source of the mixing (Polzin et al., 1995, 1997; Ledwell et al., 2000; Naveira Garabato et al., 2004). The observational data contributed to form the idea that vertical mixing by internal wave breaking played a larger role in ocean circulation than previously assumed.

St. Laurent et al. (2012) find enhanced turbulent dissipation rates as large as $10^{-8} W kg^{-1}$ and diapycnal diffusivity rates of $10^{-4} m^2 s^{-1}$ near the bottom in two frontal regions in the Drake Passage characterized by high near bottom mean velocity. They suggest the generation of lee waves as the driving mechanism for the enhanced dissipation. Sheen et al. (2013) extend this analysis to dissipation and diffusivity rates and internal wavefield properties at four transects going from the southeast Pacific to the Scotia Sea. They observe turbulent dissipation rates increase from $\mathcal{O}(10^{-10}) W kg^{-1}$ in the southeast Pacific to $\mathcal{O}(10^{-9}) W kg^{-1}$ in the Scotia Sea. They, too, credit the enhanced bottom diapycnal mixing to the breaking of lee waves, although they observe a discrepancy between the increased turbulent dissipation and the theoretical predicted lee wave energy input. Large dissipation and diffusivity rates have also been reported over the bottommost $1000m$ of the Kerguelen plateau by Waterman et al. (2013). In this study TKE dissipation rates on the order of $\mathcal{O}(10^{-9}) W kg^{-1}$ are accompanied by turbulent mixing rates on the order of $\mathcal{O}(10^{-3}) m^2 s^{-1}$. Although this study shows a qualitative match between observed dissipation rates and predicted lee wave energy flux, there is a quantitative discrepancy as the observed near-bottom dissipation is about an order of magnitude smaller than the theoretical prediction of the lee wave generation. A possible explanation of this discrepancy is hypothesized to be the energy transfer from the lee waves to the mean flow via nonlinear wave-mean flow interaction. Similarly Meyer et al. (2015b) report diffusivities larger than $10^{-3} m^2 s^{-1}$ at $1400m$ depth at the Kerguelen Plateau and credit the internal waves generated by interaction between strong bottom currents and rough bottom topography for the large mixing. Furthermore, they infer a water masss transformation of $17Sv$ in the Subantarctic/-Subtropical front at the Upper Circumpolar Deep Water/Antarctic Intermediate Water boundary. All in all, the observational evidence of the effects of lee wave driven mixing in the Southern Ocean is substantial with several reports of turbulent diffusivity and dissipation rates reaching orders of magnitude of $\mathcal{O}(10^{-3}) m^2 s^{-1}$ and $\mathcal{O}(10^{-8}) W kg^{-1}$ respectively. Cusack et al. (2017) document the first unambiguous observation of a lee wave near the Shackleton Fracture Zone in the Drake Passage. They report a vertical wave amplitude of $120 \pm 20m$ and an associated estimation of TKE dissipation on the order of $\mathcal{O}(10^{-7}) W kg^{-1}$. In the Atlantic Ocean observations are more sparse, although Köhler et al. (2014) document increased diapycnal diffusivity where the deep western boundary current meets the continental shelf in the western Atlantic, and suggests breaking lee waves as an explanation due to the combination of strong currents and rough topography.

1.4 Ocean mixing in models and IDEMIX

The mixing takes place on scales far to small for ocean models to resolve it directly. Instead mixing must be parametrized. Traditionally, though, diapycnal diffusivity has been set as constant value in ocean models, and later as a function simply of depth (Munk, 1966; Bryan and Lewis, 1979) or of the stability frequency (Cummins et al., 1990). While a depth-varying function is more realistic than a constant value, both approaches serve as a best guess with the inherent problem that they are neglecting the physical mechanism, which actually causes the mixing. A parametrization of diapycnal diffusivity ought thus to be based on the energetics of internal gravity waves. Olbers and Eden (2013) developed the energetically consistent internal wave model IDEMIX. An in-depth explanation of the model is not the scope of this section, but a quick recap of the governing principles and of the way in which the diffusivity is calculated on the basis of internal wave energetics is provided following Olbers and Eden (2013). The model is based on the radiative transfer equation for weakly interacting oceanic internal gravity waves (Hasselmann, 1967) and by exploiting the conservation of wave action, $A = E/\omega$, rather than energy (Olbers et al., 2012). This is valid for waves propagating in a medium, where the length and time scales of the mean field quantities are much larger than the length- and timescales of the waves; the so-called WKB approximation named after Wentzel, Kramers and Brillouin. In WKB theory all changes in wave action must happen due to a specific source or sink. The radiative transfer equation thus take the form

$$\frac{\partial A}{\partial t} + \nabla \cdot (\dot{\mathbf{x}} A) + \frac{\partial}{\partial z}(\dot{z} A) + \nabla_{\mathbf{k}} \cdot (\dot{\mathbf{k}} A) + \frac{\partial}{\partial m}(\dot{m} A) = S_{gen} + S_{ww} + S_{diss} \tag{1.1}$$

where $\dot{x} = \nabla_k \Omega$ and $\dot{z} = \partial\Omega/\partial m$ are the lateral and vertical group velocity, $\dot{\mathbf{k}} = -\nabla\Omega$ and $\dot{m} = -\partial\Omega/\partial z$ are the lateral and vertical wave refraction, and $\Omega = \Omega(\mathbf{k}, m, \mathbf{x}, z, t)$ is the local dispersion relation of the wave. The three terms on the right hand side constitutes the changes caused by wave action generation by external processes, wave action generated by resonant wave-wave interactions, and wave action dissipation. If one assumes a horizontal homogeneous ocean in the WKB sense the lateral refraction and propagation, i.e. the second and fourth term on the left hand side, vanishes from the radiative transfer equation.

From this an advection-diffusion scheme of internal gravity wave energy is developed by integrating over all wavenumbers. The scheme splits the wave energy in up- and downward propagating parts, which then still contain a dissipation and a wave-wave interaction term. The wave-wave interaction term in Eq. 1.1 conserves the total wave energy and is assumed to relax the wave field toward a symmetry in m, whereas the dissipation term is specified by using a steady-state equation of the conservation equation of turbulent kinetic energy (TKE) on the form

$$0 = -\overline{\mathbf{u}'_h w'}\frac{\partial \overline{\mathbf{u}}_h}{\partial z} + \overline{b' w'} - \epsilon$$

Here primed quantities refer to turbulent fluctuations, and the overbar indicates wave field values. The first term on the right hand side is the shear production of TKE, the second term is the vertical buoyancy flux (exchange of potential energy) and the third term is the heat exchange. The core of IDEMIX is thus centered around a local conservation of TKE. The shear production term is assumed to be generated by wave breaking, and as such the dissipation of internal wave energy integrated over wavenumbers is given by

$$\int_{\mathbf{k}}\int_{m} S_{diss} = F_{diss} = -\overline{\mathbf{u}'_h w'}\frac{\partial \overline{\mathbf{u}}_h}{\partial z}$$

There is thus a balance in TKE generated by wave breaking, heat generation, and the turbulent buoyancy flux, which is assumed to be negatively proportional to the density gradient as $\overline{b' w'} = -\kappa_\rho N^2$. Here, the proportionality factor κ_ρ is the vertical diffusivity and N is the local buoyancy or Brunt-Väisälä frequency. This renders the equation

$$F_{diss} = \epsilon + \kappa_\rho N^2$$

which states that the dissipation of turbulent kinetic energy caused by the breaking of internal gravity waves is consumed by a downward buoyancy flux and heat generation. It is worth noticing here, that if the ratio between F_{diss} and $\kappa_\rho N^2$ is constant here, we are left with exactly the Osborn-Cox relation described in section 1.3.

By using a combination of parameterizations, found by McComas and Müller (1981) and Henyey et al. (1986), which describe the energy transfer from low to high wavenumbers due to parametric subharmonic instability (PSI) and induced diffusion (ID), the dissipation caused by the breaking of internal gravity waves is given by

$$F_{diss} = \mu_0 f_e \frac{m_\star^2}{N^2} E^2 \tag{1.2}$$

(Olbers and Eden, 2013). Here F_{diss} is described as the energy flux from the high wavenumber roll-off in internal gravity wave domain to the turbulent mixing domain, $m_\star = N/c_\star$ is the bandwidth of the GM-spectrum, f_e is an "effective" Coriolis frequency, and E is the internal wave energy. An attempt to parameterize diffusivity from internal wave energy was already made by Müller and Natarov (2003), but the partial differential equation ends up being a function of six variables (space and wavenumber coordinates), which leaves it computationally very heavy. IDEMIX seeks to remedy this problem by integrating in wavenumber space. As such, it is important to notice that E in Eq. 1.2 is the internal wave energy integrated in wavenumber space. If the ratio between the shear production term and the buoyancy flux is assumed constant, i.e. $\kappa_\rho N^2/F_{diss} = C$, which as mentioned amounts to using the Osborn-Cox relation or assuming a constant mixing efficiency, an expression for the diffusivity can be reached

$$\kappa_\rho = \frac{\delta}{1+\delta}\frac{F_{diss}}{N^2} = \frac{\delta}{1+\delta}\mu_0 f_e \frac{E^2}{c_\star^2 N^2} \tag{1.3}$$

where $\delta = C/(1-C)$. $c_\star$ is related to the spectral bandwidth of the GM-model via one of the three central tunable parameters in the model, $j_\star$, and is dependent on the vertical integral of the buoyancy frequency N. The other two tunable parameters are the constant μ_0, and the vertical decay scale of internal wave energy asymmetry, τ_v. As such the vertical diffusivity scales with the square of the internal wave energy, but because of the complex dependency of $c_\star$ on N, the dependence of the diffusivity on the buoyancy frequency is not straightforward (this will be elaborated in section 2).

$$\kappa_\rho \sim E^2$$

The model was further developed to include wave-mean flow interaction first by Olbers and Eden (2017) in an idealized model with a prescribed stability frequency and unidirectional mean flow as functions of depth, and afterwards by Eden and Olbers (2017) in an ocean general circulation model which shows wave-mean flow interaction (or wave-drag) as a significant sink of mean flow energy in the North Atlantic. The wave-mean flow energy exchange is calculated in accordance with the non-acceleration theorem by Boyd (1976) and Andrews and Mcintyre (1976), which states that gravity waves cannot exchange energy with a mean flow in the absence of critical layers and dissipation. The predicted energy and dissipation levels was evaluated against Argo float and CTD data by Pollmann et al. (2017) in order to estimate values for tunable parameters in the model.

1.4.1 Energy consistency and pyOM

One of the strengths of IDEMIX is, as mentioned, the fact that it is energetically consistent to numerical precision. Such a construction relies upon the interaction of the energy of the mean variables with all parameterized quantities. In general, this is not the case for ocean models (Eden and Olbers, 2014). In parameterizations of unresolved processes, many closures do not account for the energy used in the process (for instance the widely used parameterization of Gent and McWilliams (1990)). A common way to deal with this problem is to reinject the lost energy to an appropriate dynamical regime. In an energetically consistent model, all energy compartments would be linked, and terms adding energy to one compartment would be removed in another. Such an approach would ensure no energy is neither gained nor lost in the model, but special attention would have to be paid to the resolved and unresolved parameterized dynamical regimes. Decomposing the ocean circulation into three different regimes - the geostrophically quasi-balanced motions, the internal gravity wave range, and the small-scale turbulence domain - Eden and Olbers (2014) calculate energy transfers and estimate the internal wave field to provide $2-3TW$ for mixing, and $1.8TW$ wind work on the large scale circulation.

In the work laid out in this thesis, IDEMIX is coupled to the ocean general circulation model pyOM (Olbers and Eden (2013), source code can be found at https://github.com/ceden/pyOM2), which solves the primitive equations in Boussinesq approximation.

The energy budget in pyOM is based on the enthalpy (the internal energy plus gravitational potential energy), $h = u+\phi$. This is a sophisticated implementation because an intrinsic feature of the Boussinesq approximation is that the gravitational potential energy is not given by the geopotential, but it is rather a thermodynamic quantity. The enthalpy is comprised of two contributors; the dynamic enthalpy, h^d, representing reversible energy changes and the potential enthalpy, h°, representing irreversible energy changes, $h = h^d + h^\circ$ (McDougall, 2003; Young, 2010; Nycander, 2011). In pyOM the energy of the mean field is described by the mean dynamic enthalpy plus the mean kinetic energy. The first one is forced by solar radiation and the latter by winds, and energy exchange between the two is reversible. Both have an energy sink to a meso-scale eddy domain and to an unresolved turbulent kinetic energy (TKE) domain. The energy fluxes to the meso-scale eddy domain is given by the eddy mixing from the mean dynamic enthalpy and by a lateral friction from by the mean kinetic energy, and they are governed by the closure of Eden and Greatbatch (2008) drawing upon Gent and McWilliams (1990). The fluxes to the TKE domain are governed by the closure of Gaspar et al. (1990) with vertical friction accounting for the flux from mean kinetic energy the to TKE and dianeutral friction accounting for the flux from the mean dynamic enthalpy to the TKE. Subsequently the eddy kinetic energy (EKE) has an energy sink to the internal gravity wave (IGW) domain (Eden and Olbers, 2014). The IGW domain is governed by IDEMIX, and this is where the new lee wave compartment is added. The original version of IDEMIX is forced by an energy flux from barotropic tides from Jayne (2009) at the bottom and at the surface by an energy flux from the mixed layer into the interior in the near-inertial band, i.e. wind-forcing, from Rimac et al. (2013). IDEMIX contains an energy sink to the TKE domain, which therefore has sources from both the internal wave domain and from the mean field. There is an irreversible energy exchange from the TKE domain to the potential enthalpy domain, which accounts for heat gain.

All variables are calculated on the staggered Arakawa-C grid (Arakawa and Lamb, 1977), where the density and pressure are calculated on the center of the grid and the (three-dimensional) velocity on the eastern, northern and upper boundary of the grid box. The model keeps track of all energy exchange between external forcing, dissipation to heat and exchange between resolved and unresolved (parameterized) processes.

1.5 Outline

The concepts and results laid out in the former paragraphs form the background knowledge required to put this thesis into a scientific context. Hopefully, it will equip the reader with the understanding of why the research carried out here is important. In chapter 2 the formulation of a lee wave module in IDEMIX is developed. The chapter also contains some important considerations about its implementation in an internal wave model is presented. Chapter 3 will narrow the research topic further and present the central key questions, which the thesis will try to answer. Here the model and experimental setups in which the research has been carried out will also be elucidated. The results of the research analysis starts in chapter 4, is further expanded in the main analysis in chapter 5, and ends with a regional focus in chapter 6. The results are discussed and put into a greater scientific perspective with the base in recent research in chapter 7. Final conclusions are presented in chapter 8.

Chapter 2

Developing a lee wave module in the internal wave model IDEMIX

This section will lay out the theoretical framework required to understand the implementation of lee waves in the internal wave model IDEMIX. The starting point will be the incompressible equations of motions in Boussinesq approximation. From there follows first a simplified example of how the upward lee wave energy flux can be calculated and subsequently a more generalized derivation of the energy flux, which will form the basis the basis of the lee wave component of IDEMIX. The component will then be thoroughly elaborated, where the energy flux will be used in the context of IDEMIX. Key equations of IDEMIX, and the exact link between the lee wave component and the rest of the model will in this process be emphasized. In the end the boundary conditions will be formulated, and consequences for the implementation due to assumptions about the topography will be laid out.

2.1 A simple lee wave energy flux

Separating the motions in horizontal and vertical components, the incompressible equations of motions in Boussinesq approximations is given as

$$D\mathbf{u} + w\partial_z\mathbf{u} + f\underset{\neg}{\mathbf{u}} = -\frac{1}{\rho_0}\nabla p \tag{2.1}$$

$$Dw + w\partial_z w - b = -\frac{1}{\rho_0}\partial_z p \tag{2.2}$$

$$Db + w\partial_z b = 0 \tag{2.3}$$

$$\nabla\cdot\mathbf{u} + \partial_z w = 0 \tag{2.4}$$

where $\mathbf{u}$ is the horizontal velocity vector and ∇ is the horizontal gradient operator, w is the vertical velocity, ρ_0 is a reference density, f is the Coriolis frequency, p is the pressure, the material operator $D = \partial_t + \mathbf{u}\cdot\nabla + w\partial_z$, and the buoyancy $b = -g\rho/\rho_0$. The $\neg$ sign indicates a 90° counterclockwise rotation of a vector. Here I have neglected the forces induced by the horizontal component of the Coriolis force, as is traditional, why a rotational term only appears in the horizontal momentum equations. The bottom boundary condition is a no-normal flow

$$w|_{z=-h} = -\mathbf{u}|_{z=-h}\cdot\nabla h \tag{2.5}$$

All quantities can now be split into a mean component and a perturbation or wave component, as $w = \overline{w} + w'$, by space-time averaging, where the overbar mean quantity and the prime signifies the perturbation. The equations for the mean momentum and buoyancy thus become

$$\partial_t\bar{\mathbf{u}} + \bar{\mathbf{u}}\cdot\nabla\bar{\mathbf{u}} + \bar{w}\partial_z\bar{\mathbf{u}} + f\underset{\neg}{\bar{\mathbf{u}}} = -\frac{1}{\rho_0}\nabla\bar{p} - \mathbf{R} \tag{2.6}$$

$$\partial_t\bar{w} + \bar{\mathbf{u}}\cdot\nabla\bar{w} + \bar{w}\frac{\partial\bar{w}}{\partial z} - \bar{b} = -\frac{1}{\rho_0}\partial_z\bar{p} - R \tag{2.7}$$

$$\partial_t\bar{b} + \bar{\mathbf{u}}\cdot\nabla\bar{b} + \bar{w}N^2 = -B \tag{2.8}$$

where I have defined the the buoyancy frequency (or stratification) $N^2 = d\bar{b}/dz$. $\mathbf{R}$ and R contains the so-called Reynold's stresses, which appear in the space-time averaging of the second term on the left hand side of Eq. 2.1 and 2.2. B similarly contains the mean wave-induced buoyancy flux. The equations for the wave component comes about from subtracting equations for the mean components from the equations for the full field

$$(\partial_t + \bar{\mathbf{u}}\cdot\nabla + \bar{w}\partial_z)\,\mathbf{u}' + f\underset{\neg}{\mathbf{u}'} = -\frac{1}{\rho_0}\nabla p' - \mathbf{R} - \left(\mathbf{u}'\cdot\nabla - w'\partial_z\right)\bar{\mathbf{u}} \tag{2.9}$$

$$(\partial_t + \bar{\mathbf{u}}\cdot\nabla + \bar{w}\partial_z)\,w' - b' = -\frac{1}{\rho_0}\partial_z p' - R - \left(\mathbf{u}'\cdot\nabla - w'\partial_z\right)\bar{w} \tag{2.10}$$

$$\partial_t b' + \bar{\mathbf{u}}\cdot\nabla b' + w'N^2 = -B - \mathbf{u}'\cdot\nabla\bar{b} \tag{2.11}$$

where last two terms in Eq. 2.9 and 2.10 and the last term in Eq. 2.11 originate from the advective term on the right hand side. These are the wave-induced advection of mean momentum and mean buoyancy.

We can imagine a simplified case, where the mean wave-induced stresses and the wave-induced advection of mean momentum and buoyancy are neglected on the right hand, and we are left with equations for the wave components including a term with advection by the mean flow. If this mean flow is considered as a constant $\bar{\mathbf{u}} = (U_0, 0)$, the wave equations become

$$(\partial_t + U_0\partial_x)\,\mathbf{u}' + f\underset{\neg}{\mathbf{u}}' = -\frac{1}{\rho_0}\nabla p' \tag{2.12}$$

$$(\partial_t + U_0\partial_x)\,w' = -\frac{1}{\rho_0}\partial_z p' + b' \tag{2.13}$$

$$(\partial_t + U_0\partial_x)\,b' + w'N^2 = 0 \tag{2.14}$$

Here, assuming steady solutions, we can combine these into a single equation for w' (Legg, 2021).

$$U_0^2\partial_x^2(\nabla^2 + \partial_z^2)\,w' + f\partial_z^2 w' + N^2\nabla^2 w' = 0 \tag{2.15}$$

With a mean flow over, in this case, a simplified topography given by a sinusoidal

$$h = h_0 \sin(kx) \tag{2.16}$$

where k is the topographic wavenumber, the linearized bottom boundary condition in a generalized form becomes

$$w' = -U_0\partial_x h = -U_0 k h_0 \cos(kx) \tag{2.17}$$

In other words, such a mean flow at the bottom will generate lee waves, and since the mean flow does not have a time dependency, the frequency of encounter of these waves is equal to zero, but the Doppler-shifted frequency is equal to $\omega = -U_0 k$. In the water column the vertical wave velocity attains a generalized form associated with the bottom boundary condition

$$w' = -U_0 k h_0 \cos(kx + m(z+H))$$

From Eq. 2.12-2.14 we are now able to calculate the buoyancy and pressure associated with the lee waves.

$$b' = h_0 N^2 \sin(kx + m(z+H)) \tag{2.18}$$

$$p' = \rho_0 h_0 \frac{1}{m}\left(N^2 - U_0^2 k^2\right)\cos(kx + m(z+H)) \tag{2.19}$$

The waves induce a vertical energy flux given by pressure times the vertical velocity.

$$F = \langle w' p' \rangle = -\frac{k}{2m}\rho_0 h_0^2 U_0 \left(N^2 - U_0^2 k^2\right) \tag{2.20}$$

where m is negative, signifying an upqard energy flux, and the brackets indicate an average taken over one topographic wavelength. From Eq. 2.15 we can derive a dispersion relation, which can give us an estimate of the energy flux when used in Eq. 2.20

$$m^2 = k^2 \frac{N^2 - \omega^2}{\omega^2 - f^2} \tag{2.21}$$

The dispersion relation shows that lee waves can only have frequencies in the range between the Coriolis frequency and the local stability frequency, $f < U_0 k < N$. It also shows the limits of the topography which can create lee waves. If the bottom speed is $U_0 \sim \mathcal{O}(0.1 m/s)$ and $f \sim \mathcal{O}(10^{-4} s^{-1})$ the topographic wavenumber is $k \sim \mathcal{O}(10^{-3} m^{-1})$, or in other words the topographic wavelength is $\lambda \sim 1 km$. Of course, these are rough numbers, but in general the topographic wavelength is a few kilometers, and these are often called abyssal hills (Goff and Arbic, 2010).

2.2 Generalizing the basic example

In case we are not dealing with a simplified mean flow and topography as described above, the derivation of the upward energy flux generated by lee waves is a bit more complicated. Linearizing the equations of motions around a basic state gives equations for the perturbation or wave part (of the first three equations)

$$\partial_t \mathbf{u}' + \bar{\mathbf{u}} \cdot \nabla \mathbf{u}' + w' \partial_z \mathbf{u}' + f \underset{\neg}{\mathbf{u}}' = -\nabla p' \tag{2.22}$$

$$\partial_t w' + \bar{\mathbf{u}} \cdot \nabla w' + w' \partial_z w' - b' = -\partial_z p' \tag{2.23}$$

$$\partial_t b' + \mathbf{u}' \cdot \nabla b' + w' N^2 = 0 \tag{2.24}$$

Along with Eq. 2.4 these can be rearranged to form the equation for the vertical wave velocity w'

$$D^2 (\nabla^2 + \partial_z^2) w' + N^2 \nabla^2 w' + f^2 \partial_z^2 w' = 0 \tag{2.25}$$

The bottom boundary condition is still given as a no-normal flow, i.e. $w = -\mathbf{u} \cdot \nabla h$ at $z = -H$. We now wish to attain an expression for an upward energy flux at the bottom. Since the waves are generated by the mean flow at the bottom (i.e. no time dependency) they must have a frequency of encounter (or Doppler shifted frequency) equal to zero and an intrinsic frequency $\omega = -\mathbf{k} \cdot \mathbf{U_0}$, where $\mathbf{U_0}$ is the bottom velocity.

Generalizing to a two-dimensional topography spectrum and a bottom flow $\mathbf{U_0} = (U_0, V_0)$ Bell (1975) gives the bottom energy flux as

$$F_{bell} = \frac{\rho_0}{4\pi^2} \frac{\mathbf{U_0} \cdot \mathbf{k}}{\mathbf{k}} P(\mathbf{k}) \left(N^2 - (\mathbf{U_0} \cdot \mathbf{k})^2\right)^{1/2} \left((\mathbf{U_0} \cdot \mathbf{k})^2 - f^2\right)^{1/2}$$

where $P(\mathbf{k})$ is the so-called topography spectrum dependent on the topographic wavenumber in both horizontal directions. A correction to the Bell energy flux was considered by Nikurashin and Ferrari (2010b), since the linear theory only proved accurate until the ration

$$Fr = \frac{Nh_0}{|\mathbf{U_0}|} \approx 0.7$$

where h_0 is the amplitude of a sinusoidal topography. This ratio is called the inverse Froude Number and can be interpreted in several ways. First it represents the momentum, which a bottom mean flow must have in order to elevate a water parcel above a certain height, h_0, in a given environment, N. The interpretation is such that if the flow is not sufficiently strong (or the abyssal hill is to high), the current will not be able lift water parcel above the topographic hill, and flow will simply be blocked or the water will flow around the hill rather than above it (Smith, 1989). The ratio is also an approximation of the steepness of the topography relative to the ratio of the horizontal and the vertical wavenumbers. If we consider $f \ll U_0 k \ll N$

$$\frac{h_0/\lambda}{k/m} = \frac{h_0 k}{\sqrt{\frac{U_0^2 k^2 - f^2}{N^2 - U_0^2 k^2}}} \approx \frac{Nh_0}{U_0} \tag{2.26}$$

The interpretation of this is that lee waves are not allowed to travel at an angle (with respect to the horizontal) that is larger than topographic steepness; this steepness is referred to as the subcritical range. It is thus clear that the ratio Nh_0/k is important for lee wave characteristics. In a global estimate of the lee wave energy flux, it was introduced by Scott et al. (2011) as a simple limiter function (details explained subsequently). Such a function effectively limits the height from which a topographic obstacle can generate lee waves (Sarkar and Scotti, 2017).

From the bottom energy flux, the aim is to derive an energy equation for lee waves, which will govern the evolution of lee wave energy in the model. The lee wave energy will therefore act as its own energy compartment in the model, but it will be linked with both the mean flow and the background internal wave energy domain. Separating the lee waves from the background internal waves can seem arbitrary, but considering that they are stationary waves with a frequency of encounter, $\omega_{enc} = 0$, it actually makes sense to treat them as a separate entity, because in this sense they are different from other types of internal gravity waves.

Besides the energy equation for the lee waves, we want to derive momentum fluxes to/from the mean flow and thereby link the lee waves to the momentum equation. A special emphasis will also be put on the bottom energy flux and the way in which diapycnal diffusivity is coupled to the lee wave component.

2.3 Formulating an energy equation for lee waves

As mentioned, a geostrophic flow $\mathbf{U_0} = \mathbf{U}|_{z=-H}$ over topographic features at the ocean floor generates lee waves with intrinsic frequency $\omega = -\mathbf{U_0}\cdot\mathbf{k}$, vertical wavenumber $|m| = k\sqrt{N^2-\omega^2}/\sqrt{\omega^2-f^2}$, and vertical group velocity $\dot{z} = \sigma\dfrac{(\omega^2-f^2)^{3/2}(N^2-\omega^2)^{1/2}}{k^2|U_n|(N^2-f^2)}$ (Olbers et al., 2012). Here $U_n = \mathbf{U_0}\cdot\mathbf{n}$, where $\mathbf{n} = (\cos(\phi), \sin(\phi))$ is the horizontal unit vector, signifies the alignment of the mean flow with the horizontal wave angle ϕ, and $\sigma = \mathrm{sign}(m\cdot U_n)$

We express the energy contained in the waves as a density spectrum, which is given as $\mathscr{E}(m,k,\phi)$, where m and k are horizontal and vertical wavenumbers respectively, and ϕ is the propagation direction relative to true north. The energy density spectrum is governed by the radiative transfer equation (Olbers et al., 2012)

$$\partial_t\mathscr{E} + \partial_z(\dot{z}\mathscr{E}) + \partial_m(\dot{m}\mathscr{E}) = -(\dot{z}/\omega)\mathbf{k}\cdot(\partial_z\mathbf{U})\mathscr{E} + S \tag{2.27}$$

where $\dot{z} = \partial\omega/\partial m$ and $\dot{m} = -\partial_z\omega$ are the vertical group velocity and the refraction respectively. The first term on the right hand side represents wave-mean flow interaction (wave drag) and the S are all other sources and sinks of energy (e.g. forcing, dissipation and non-linear transfers of energy). The deductions made in the following section will use the definition of the vertical group velocity to obtain an expression for the wave mean flow interaction and thereby forming an energy equation. As is, however, the energy of the lee waves is dependent on both the vertical and horizontal wavenumber and the angle of propagation. In an ocean general circulation model this would of course be in addition to a dependency on the physical coordinates of the model constituting a total dependency on six variables. This would computationally extremely heavy and, although in itself interesting, an energy transfer in wavenumber space is not the scope of this study. Therefore we follow the derivation of Olbers and Eden (2013) to integrate the energy density over wavenumber (and later over angle) and split into up- and downward propagating waves, indicated by superscript $\pm$, defining

$$\epsilon^{\pm}(\phi) = \int_0^{\infty}\int_{-\infty}^{\infty}\max(\pm\sigma,0)\mathscr{E}(m,k,\phi)\partial k\partial m \tag{2.28}$$

as the wavenumber-integrated energy. Such an integration leaves Eq. 2.27 as

$$\partial_t\epsilon^{\pm} + \partial_z(c^{\pm}\epsilon^{\pm}) = -\mathbf{n}\cdot\partial_z\mathbf{U}\Lambda^{\pm}\epsilon^{\pm} + \int_0^{\infty}\int_{-\infty}^{\infty}\max(\pm\sigma,0)S\partial k\partial m \tag{2.29}$$

where the exchange with the mean flow is determined by the two so far unexplored parameters, $\Lambda^{\pm}$ and $c^{\pm}$. We call $\Lambda^{\pm}$ the mean flow exchange parameter. Using the relation $\omega = -kU_n$ this is defined as

$$\Lambda^{\pm}(t,z,\phi) = \int_0^{\infty}\int_{-\infty}^{\infty} \max(\pm\sigma,0)(\dot{z}/\omega)k\mathscr{E}\partial k\partial m/\epsilon^{\pm} \tag{2.30}$$

$$\Lambda^{\pm}(t,z,\phi) = -|U_n|^{-1}\int_0^{\infty}\int_{-\infty}^{\infty} \max(\pm\sigma,0)\dot{z}\mathscr{E}\partial k\partial m/\epsilon^{\pm} \tag{2.31}$$

$c^{\pm}$ is a wave energy-averaged vertical group velocity, which is given as

$$c^{\pm}(t,z,\phi) = \int_0^{\infty}\int_{-\infty}^{\infty} \max(\pm\sigma,0)\dot{z}\mathscr{E}\partial k\partial m/\epsilon^{\pm} = -|U_n|^{-1}\sigma_U\Lambda^{\pm}$$

2.4 Spectral shape, exchange parameter and vertical group velocity

We wish now, of course, to obtain suitable expressions for the mean flow exchange parameter Λ and thereby also the vertical group velocity c. This will allow us to determine the interaction between lee waves and the mean flow, given by the first term on the right hand side of Eq. 2.29, and the vertical propagation of lee wave energy, given by the second term on the left hand side. After this we only need to close the energy equation by the source/sink term. In the above equations the rather complicated formulation involving the max-function is necessary since $\sigma = \text{sign}(m{\cdot}U_n)$ not only depends on the vertical wavenumber, but also the direction of the mean flow. We assume in the model that the energy density anywhere in the water column stays close to that generated at the bottom

$$\mathscr{E}(m,k,\phi) = A(k,\phi)\left(\epsilon^{+}(\phi)\delta(m-\sigma_U|m_{lee}|) + \epsilon^{-}(\phi)\delta(m+\sigma_U|m_{lee}|)\right) \tag{2.32}$$

where $A(k,\phi)$ is a shape function determined by the energy flux at the bottom and is normalized such that Eq. 2.32 matches exactly the definition of Eq. 2.28. This is an assumption which leaves out such phenomena as critical layers and wave capture. Using this form and the definition of the vertical group velocity in Eq. 2.31 we get for the mean flow exchange parameter and the vertical group velocity

$$\Lambda^{\pm}(t,z,\phi) = \mp|U_n|^{-1}\sigma_U\int_0^{\infty} A|\dot{z}|\partial k, c^{\pm} = \pm\int_0^{\infty} A|\dot{z}|\partial k \tag{2.33}$$

where $\sigma_U = \text{sign}(U_n)$. So, the exchange of energy between the lee waves and the mean flow is throughout the water column governed by the energy flux at the bottom, and in order to formulate exchange term it is necessary (and sufficient) to evaluate the integral $\int_k A|\dot{z}|\partial k$. In the case of lee waves the energy flux at the bottom is given by Bell (1975) as

$$F_{bell}(k,\phi) = 4\pi^2|U_n|(N^2-k^2U_n^2)^{1/2}(k^2U_n^2-f^2)^{1/2}L(Fr)F_{top}(k,\phi) \tag{2.34}$$

The Bell energy flux is a function of wavenumber and direction of propagation. The factor $L(Fr)$ was introduced by Scott et al. (2011) to account for the increased blocking by topography in the case of large topographic heights or buoyancy or smaller velocities. The idea is, that in the case of such obstacles or flow properties, the water will to a larger extent flow around instead of over obstacles and thus generate waves to a lesser extent. The factor is thus a function of the (inverse) Froude Number, $Fr^{-1} = HN/U$, that limits the energy flux derived by Bell (1975). It is defined as

$$L(Fr) = \begin{cases} 1 & \text{if } Fr^{-1} \leq Fr_c^{-1} \\ \dfrac{Fr}{Fr_c} & \text{if } Fr^{-1} > Fr_c^{-1} \end{cases}$$

An appropriate value of the critical Froude Number Fr_c is examined in greater detail in Aguilar and Sutherland (2006), but here we will test two different values $Fr_c = 0.75$ and $Fr_c = 0.5$. The shape of the topographic spectrum F_{top} is given by Goff and Jordan (1988) and values of the parameters, which characterizes the spectrum, by Goff (2010). The topographic spectrum takes the form

$$F_{top}(k,\phi) = \frac{h_{rms}^2 \nu}{\pi k_n k_s} k(1 + k^2/k_s^2 \cos^2(\phi - \phi_s) + k^2/k_n^2 \sin^2(\phi - \phi_s))^{-(\nu+1)} \tag{2.35}$$

and the defining parameters are the topographic wavenumbers in so-called strike and normal direction, k_s and k_n, the rms-height, h_{rms}, and the angle of orientation, ϕ_s. The Hurst number, ν, is in our case set to $\nu = 0.9$. The topographic spectrum can be assumed isotropic, where $k_s = k_n$. This assumption simplifies both the deduction of the lee wave energy and momentum flux and the implementation in the model, since the dependence on ϕ vanishes because of the Pythagorean identity. With this assumption the topographic spectrum reduces to

$$F_{top,IS}(k) = \frac{h_{rms}^2 \nu}{\pi k_s^2} \frac{k}{(1 + k^2/k_s^2)^{\nu+1}} \tag{2.36}$$

The energy at the bottom is given by the flux

$$E_{bell}(k,\phi) = \frac{F_{bell}(k,\phi)}{\dot{z}} \tag{2.37}$$

and using Eq. 2.32 and 2.28 the shape function $A(k,\phi)$ takes the form

$$A(k,\phi) = E_{bell}(k,\phi)\left(\int_0^\infty E_{bell}(k,\phi)\partial k\right)^{-1} \tag{2.38}$$

With the isotropic topographic spectrum the shape function is then expressed as

$$A(k,\phi) = \left(\frac{|U_n|}{N}\right)^{-2\nu} J^{-1} \frac{k^2 U_n^2}{k^2 U_n^2 - f^2 + r^2} k^{-2\nu-1}, J = \int_{|f|/N}^{1} \frac{t^{-2\nu+1}}{t^2 - (f/N)^2 + (r/N)^2} \partial t$$

where the ϕ dependence enters via U_n. The r in the denominator is an artificial constant and is added to avoid singularity at $k^2 U_n^2 = f^2$, but note both that $r \ll f$ and that the mean exchange parameter, $\Lambda^\pm$, is only weakly dependent on r. Using the definition of $\dot{z}$, this formulation of the shape function gives the mean exchange parameter

$$\Lambda^\pm = \mp |U_n|^{-1} \sigma \int_0^\infty A|\dot{z}|\partial k$$
$$\Lambda^\pm = \mp \sigma_U \left(\frac{|U_n|}{N}\right)^{-2\nu} \frac{J^{-1}}{(N^2 - f^2)} \int_{|f|/|U_n|}^{N/|U_n|} (N^2 - k^2 U_n^2)^{1/2} (k^2 U_n^2 - f^2)^{1/2} k^{-2\nu-1} \partial k$$

where the boundaries of the integral has been set due to the expression $f \leq kU_n \leq N$. With the transformation $t = U_n k/N$ the integral can be converted into one which is independent on k (and ϕ) (see appendix)

$$\int_{|f|/|U_n|}^{N/|U_n|} (N^2 - k^2 U_n^2)^{1/2} (k^2 U_n^2 - f^2)^{1/2} k^{-2\nu-1} \partial k =$$
$$\left(\frac{N}{|U_n|}\right)^{-2\nu} N^2 \int_{|f|/N}^{1} t^{-2\nu-1} (t^2 - f^2/N^2)^{1/2} (1 - t^2)^{1/2} \partial t$$

which gives the expression for the exchange parameter

$$\Lambda^\pm = \mp \sigma_U \frac{N^2}{N^2 - f^2} \frac{I}{J} \tag{2.39}$$

where $I = \int_{|f|/N}^{1} t^{-2\nu-1} (t^2 - f^2/N^2)^{1/2} (1 - t^2)^{1/2} \partial t$. Here it is also clear that the only angular dependency of $\Lambda^\pm$ enters via σ_U. It is shown in the appendix of Eden et al., 2020 (under review) that suitable expression for I and J are

$$I \approx 0.65 \left(\frac{N}{f}\right)^{\nu}, J \approx \left(\frac{N}{f}\right)^{2\nu} \log(f/r)$$

If we assume for practical reasons $N^2 \gg f^2$ and $\nu = 1$, we obtain the final expression for the exchange parameter, which enters Eq. 2.29

$$\Lambda^\pm = \mp \sigma_U \Lambda_0 \approx \mp 0.65 \sigma_U \frac{f}{N} \log(f/r) \tag{2.40}$$

where we have defined $\Lambda_0 = I/J$. This very neat expression for the mean exchange parameter is only possible when using the isotropic topography spectrum, but it allows for a simple expression of the interaction between the mean flow and the lee waves given by the first term on the right hand side of Eq. 2.29. It also determines the vertical group velocity

$$c^{\pm} = \pm|U_n|\Lambda_0 \tag{2.41}$$

which allows the deduction of an expression for the vertical propagation as given by the second term on the left hand side of the energy equation.

2.5 Finalizing the energy equation

We now need to finalize the energy Eq. 2.29 by calculating second term on the right hand side $\partial_z(c^{\pm}\epsilon^{\pm})$ and the first term on the right hand side - the mean flow exchange - given by $-\mathbf{n}\cdot\partial_z\mathbf{U}\Lambda^{\pm}\epsilon^{\pm}$, and to close it by specifying the source/sink term. The energy contained in the lee waves is allowed to propagate, dissipate and exchange energy with the background wave field (which is assumed to take a GM shape) and the mean flow. In order to obtain an expression for the total energy of the wave, we integrate Eq. 2.29 over angle as well

$$E^{\pm}_{lee} = \int \epsilon^{\pm} d\phi \tag{2.42}$$

The integral of the vertical propagation term over angle becomes $\int_0^{2\pi} c^{\pm}\epsilon^{\pm}d\phi$, and here we use the following approximation

$$\int_0^{2\pi} c^{\pm}\epsilon^{\pm}d\phi \approx \pm\frac{2}{\pi}\Lambda_0\int_0^{2\pi}|\mathbf{n}\cdot\mathbf{U}_0|d\phi\int_0^{2\pi}\epsilon^{\pm}d\phi = \pm\frac{2}{\pi}\Lambda_0|\mathbf{U}_0|E^{\pm}_{lee} \tag{2.43}$$

Here we can define the angular integrated vertical group velocity $c_{lee} = 2/\pi\Lambda_0|\mathbf{U}_0|$, so that the approximation of the angular integrated vertical propagation term gives

$$\int_0^{2\pi} c^{\pm}\epsilon^{\pm}d\phi \approx \pm c_{lee}E^{\pm}_{lee} \tag{2.44}$$

The integration of the mean flow exchange over angle is thus similarly approximated by

$$\int_0^{2\pi}\mathbf{n}\cdot\partial_z\mathbf{U}\Lambda^{\pm}\epsilon^{\pm}d\phi = \mp\Lambda_0\partial_z\mathbf{U}\cdot\int_0^{2\pi}\mathbf{n}\sigma_U\epsilon^{\pm}d\phi \approx \mp\frac{2}{\pi}\Lambda_0\frac{\mathbf{U}_0}{|\mathbf{U}_0|}\partial_z\mathbf{U}E^{\pm}_{lee} = \mp\mathbf{e}_{lee}\partial_z\mathbf{U}E^{\pm}_{lee} \tag{2.45}$$

where we have defined $\mathbf{e}_{lee} = 2/\pi\Lambda_0\mathbf{U}_0/|\mathbf{U}_0|$. This gives us final expression for the two terms in the lee wave energy equation representing vertical propagation and exchange with the mean flow. These are given in terms of the mean exchange parameter Λ_0 and the vertical group velocity c_{lee}. The last thing we need is to formulate a closure for the source/sink term. Here we choose to include a symmetrization term with a tuneable timescale, and a term accounting for the interaction of the lee wave compartment with the background internal wave compartment. As mentioned, the separation of the lee wave compartment and the background internal wave compartment is justified because of the different spectral shapes. This leaves us with a final equation governing the evolution of the lee wave energy of the form

$$\partial_t E^{\pm}_{lee} = \mp\partial_z\left(c_{lee}E^{\pm}_{lee}\right) \pm \tau^{-1}_{lee}E^{\pm}_{lee} \mp \frac{\tau_s^{-1}}{2}\Delta E_{lee} - \alpha_{ww}E_{GM}E^{\pm}_{lee} \tag{2.46}$$

Here ΔE is the energy difference between up- and downward propagating waves, $\tau^{-1}_{lee} = \mathbf{e}_{lee}\partial_z\mathbf{U}$ and τ_s are the wave drag and the vertical symmetrization time scales, respectively. The second term on the right hand side represents the interaction with the mean flow, while the third term on the right hand side represents the vertical symmetrization of up- and downward propagating waves. τ_{lee} is set in the model to 3 days, which is the same as the interior wave drag timescale of the background wave field. The last term on the right hand side represents the interaction between the background IW field, where

$$\alpha_{ww} = \mu_0\frac{\operatorname{arccosh}(N/f)|f|}{c_\star^2} = \mu_0\frac{|f_e|}{c_\star^2} \tag{2.47}$$

is defined in Olbers and Eden (2013), and $c_\star$ is related to the bandwith of the GM spectrum and defined as

$$c_\star = \frac{1}{j_\star\pi}\int_h^0 N dz \tag{2.48}$$

The particular scaling given by α_{ww} is the parameterizations of induced diffusion and parametric subharmonic instability mechanisms described by McComas and Müller (1981).

2.6 Pseudo-momentum fluxes and the effect on the mean flow

The waves also exert a drag on the mean momentum. It turns out, however, that using the residual momentum instead of the Eulerian momentum, it is possible to combine the vertical flux of momentum and the lateral buoyancy flux into a single term dubbed the pseudo-momentum flux.

Eden and Olbers (2017) showed how, in wavenumber space, the pseudo-momentum flux is given by

$$\tau = \overline{\mathbf{u}'w'} + \overline{\mathbf{u}'b'fN^{-2}} = \dot{z}\mathbf{k}\mathscr{E}/\omega$$

where the overline signifies an average over one entire wave period. Integration over the allowed vertical and horizontal wavenumbers give

$$\mathbf{t}^{\pm}(\phi) = \int_0^{\infty}\int_{-\infty}^{\infty} \dot{z}\mathbf{k}\mathscr{E}/\omega \partial m \partial m = \mathbf{n}\epsilon^{\pm}\Lambda^{\pm}$$

which is the angular dependent pseudo-momentum flux. Here we have used the definition of Λ given by Eq. 2.31. In order to arrive at the full momentum flux we then need to integrate over the propagation angle and sum over the two contributions from the upward and downward waves. The dependence on ϕ of Λ is only determined by $sign(U_n)$ and we therefore get the integral

$$\tau = \sum_{\pm}\int_0^{2\pi} \mathbf{t}^{\pm}\partial\phi = \sum_{\pm}\int_0^{\infty} \mathbf{n}\epsilon^{\pm}\Lambda^{\pm}\partial\phi$$

Using the same approximation as in Eq. 2.45 we then get.

$$\boldsymbol{\tau} = -\mathbf{e}_{lee}(E^{+}_{lee} - E^{-}_{lee}) = -\mathbf{e}_{lee}\Delta E_{lee} \tag{2.49}$$

The vertical divergence of the pseudo-momentum equation enters the mean residual momentum equation, where it acts as an exchange term. However, the exchange can be in either direction dependent on the mean flow and difference in energy of the upward- and downward propagating waves.

2.7 Coupling to the internal wave compartment

The parameters μ_0 and $j_\star$ are tunable parameters in the model. The separation of the lee wave energy and the background internal wave energy can seem somewhat arbitrary, but the justification lies and the spectral shape of the two. Whereas the internal wave energy spectrum is assumed to attain a GM-shape (an assumption which is widely accepted in the literature, although arguments for regional deviations are too (Polzin and Lvov, 2011)), the lee wave energy attains spectral shape given by the Bell flux at the bottom (2.34).

The diapycnal diffusivity κ_ρ is calculated by IDEMIX according to equation 18 in Olbers and Eden (2013). The addition of lee waves to the model brings about an exchange of energy between background internal wave field and the lee waves. This exchange is represented by the fourth term on the right hand side of Eq. 2.46, where a similar term is added to the general internal wave field. As such, at every grid point and time step the internal wave energy, from which the diffusivity is calculated, will thus receive a contribution from the lee wave field

$$\partial_t E_{iw}^{\pm} = ... + \alpha_{ww} E_{GM} E_{lee}^{\pm}$$

before any propagation and dissipation of energy is taken into account at said grid point. The rest of the terms governing the internal wave energy has here been left out to focus on the coupling with the lee wave model. Whereas the diapycnal diffusivity is directly proportional to the square of the internal wave energy, its dependency on the stability frequency is not as straightforward, since it involves the vertical integral over the stability frequency as given by $c_\star$ in Eq. 2.48

$$\kappa_\rho \sim \frac{E_{iw}^2}{c_\star^2 N^2}$$

where E_{iw} is the total internal wave energy, i.e. the GM shape-assumed energy plus the contribution from the lee waves. In our model the lee waves therefore directly affect both the mean momentum equation, the mean flow and the internal wave field, while they indirectly affect the diapycnal diffusivity.

2.8 Bottom boundary conditions and anisotropic spectrum

The bottom boundary conditions for the energy and (residual) momentum equation is given by the bottom energy flux and the bottom stress. The bottom energy flux F_{bell} given by equation 2.34 is integrated over k and ϕ to arrive at the bottom energy flux. Using the isotropic spectrum and the substitution $t = |U_n|k/N$, this can be written as

$$F_{bell}(\mathbf{x}, k, \phi) = 4\pi \frac{h_{rms}^2 N^3}{k_s} L\nu \left(\frac{|U_n| k_s}{N}\right)^{2\nu+1} \frac{|U_n|}{N} \sqrt{1-t^2} \sqrt{t^2 - f^2/N^2}\, t^{-2\nu-1} \quad (2.50)$$

where $U_n = \mathbf{U} \cdot \mathbf{n}$. Here the dependence on k enters via t and the ϕ dependence via U_n. Integrated over k this gives

$$\int_{f/|U_n|}^{N/|U_n|} F_{bell} dk = 4\pi \frac{h_{rms}^2 N^3}{k_s} L\nu \left(\frac{|U_n| k_s}{N}\right)^{2\nu+1} I \quad (2.51)$$

using the previously defined I. In order to arrive at the full bottom boundary condition for the energy flux the integration over ϕ gives

$$\int_{f/|U_n|}^{N/|U_n|} \int_0^{2\pi} F_{bell} d\phi dk = 8a\pi \frac{h_{rms}^2 N^3}{k_s} L\nu \left(\frac{|U_n| k_s}{N}\right)^{2\nu+1} I \quad (2.52)$$

where $a = \int_{-\pi/2}^{\pi/2} \cos^{2\nu+1}\phi d\phi$ and takes values $\pi/2 < a < 4/3$ for $1/2 < \nu < 1$. In our model we choose $\nu = 0.8$ and $a = 4/3$. From the relation $\tau_{bell} \cdot U_0 = -F_{bell}$ we are able to calculate the bottom stress as

$$\int_{f/|U_n|}^{N/|U_n|} \int_0^{2\pi} \tau_{bell} d\phi dk = -8a\pi \frac{h_{rms}^2 N^3}{k_s} L\nu \frac{\mathbf{U_0}}{|\mathbf{U_0}|^2} \left(\frac{|U_n| k_s}{N} \right)^{2\nu+1} I \tag{2.53}$$

These two make up the bottom boundary conditions using the isotropic spectrum. If the topographic spectrum is not assumed isotropic, i.e. k_s is in general not equal to k_n, the derivation leading to the very neat expression of the exchange parameter, Λ in Eq. 2.40 is not possible. Both the bottom lee wave flux and stress must therefore be calculated by numerically integrating over both wavenumber and propagation angle. They are in each case given by the boundary conditions at the bottom. The bottom energy flux (integrated over wavenumber and propagation angle) is added to the upward minus the downward energy propagation to form the bottom boundary condition for the energy. The bottom stress is still defined by 2.49 and bottom flux and stress is thus calculated from

$$F_{bot}(x,y) = \int_k \int_\phi F_{bell} d\phi dk = \int_k \int_\phi 4\pi^2 U_n (N^2 - k^2 U_n^2)^{1/2} (k^2 U_n^2 - f^2)^{1/2} L(Fr) F_{top}(k,\phi) d\phi dk \tag{2.54}$$

$$\tau_{bot}(x,y) = \int_k \int_\phi \sigma_U \cdot \mathbf{n} F_{bell} \frac{1}{\mathbf{n} \cdot \mathbf{U_0}} d\phi dk \tag{2.55}$$

where the topographic spectrum $F_{top}(k,\phi)$ is given by Eq. 2.35, and the vector $\mathbf{n} = (\cos\phi, \sin\phi)$ such that it vanishes in when calculating the magnitude of the stress.

Chapter 3

Research Questions

As outlined in the previous chapter, lee waves are believed to have a significant impact on ocean circulation via their contribution to vertical mixing and their interaction with (and energy extraction from) the mean flow. Despite this, questions about their role in this regard are still open (MacKinnon et al., 2017; Legg, 2021). Including lee waves in an internal wave model will therefore facilitate an investigation into this role. The current model implementation allows for an examination of the effect of several parameter values on lee wave generation and their subsequent effect on the ocean.

In the original IDEMIX model three intrinsic parameters needs to be specified in order to finalize the diffusivity parameterization, μ_0, $j_\star$, and τ_v. The first two determine the link between internal wave energy and diffusivity and the third set the vertical decay scale of internal wave energy asymmetry. These three parameters also determine the link between the background internal wave compartment and lee wave compartment via the exchange coefficient α_{ww}, and as such also the effect of lee waves on the diffusivity. Because of the uncertainty about the magnitude of this effect in the real ocean (Waterman et al., 2013; Legg, 2021), this formulation is still based on a theoretical approach rather than observational constraints. In other words, more observational data is still needed to elucidate the route from lee wave energy to turbulent mixing. Nevertheless, the formulation used here is based on parameterizations of the transfer of internal gravity wave energy in wavenumberspace (Eden and Olbers (2014) and references therein), which have been evaluated against ARGO-derived estimates of internal gravity wave energy with great success (Pollmann et al., 2017).

In the new lee wave compartment, described above, assuming the topography isotropic leads to a simplified but approximated bottom energy flux. In the model setup the topography spectrum can be set either as isotropic or anisotropic. The value of the critical inverse Froude Number, Fr_C, is also specified in the setup allowing two main parameters, which can be varied. The combined effects of the different choices of IDEMIX parameters and lee wave approximations on both lee wave generation itself and its subsequent role in shaping mean flow, diffusivity and stratification are unknown, and a thorough investigation of these effects is therefore needed to determine how the lee wave component should be set up in an actual ocean general circulation model. The thesis will therefore analyze the effect of different choices of parameter values on these quantities.

As mentioned, several authors (Nikurashin and Ferrari, 2010a; Scott et al., 2011; Trossman et al., 2013; Wright et al., 2014) have estimated the bottom lee wave energy flux with varying results. These studies differ in their use of bottom velocity and topography data, but it applies for all of them, that all of them have *i*) used the isotropic topography spectrum and *ii*) estimated the bottom flux as a non-integrated part of an ocean model. To the author's knowledge no study on the effect of using the anisotropic topography spectrum rather than the isotropic one has been carried out. Furthermore, the lee waves are likely to be a part of feedback mechanisms (such as lee waves extracting energy from and thus weakening the bottom flow, resulting less available energy for the lee waves themselves), and an investigation of their effect on the ocean state should therefore be done with them fully integrated in the model. We have done this in IDEMIX.

If the generation and subsequent breaking of lee wave have a significant effect on the mean flow and on vertical mixing, this would be relevant to include in long term simulations as well. The hypothesized effect of lee waves on the overturning circulation for example (Melet et al., 2014; De Lavergne et al., 2016) warrants consideration of lee waves in representations of the overturning. But for long term simulations coarser model resolution is preferred (for computation time purposes), and the sensitivity of lee wave generation to model resolution is therefore also investigated in this study. Because eddies have been suggested as a major contributor for strong bottom flows needed to generate lee waves, it is likely that the ultimate aim for coarse resolution models should be to include a lee wave energy flux parameterized on the eddy kinetic energy. Comparisons between coarse and high resolution models should help elucidate this topic.

Taking these factors into consideration this thesis will investigate lee wave generation and its effect on the mean flow, diffusivity and stratification. This will be done using models with different resolution and with different choices of parameter values using one specific model. The aim is to clarify the effect of model resolution on lee wave generation, and to determine what difference the choice of IDEMIX parameter values and topography spectrum have on lee wave generation and subsequently on the mean flow and diffusivity. Additional energy available for mixing (the lee wave energy) should result in an increased diffusivity. The interconnected effects of lee waves, mean flow, and stratification adds further complexity, and renders questions of where and by how much the mixing would increase in the different experiments yet open. Key questions which the thesis will seek to answer are therefore

- What effect does model resolution have on lee wave generation?
- How sensitive is the lee wave generation to using an anisotropic topography spectrum rather than an isotropic one, and what is the subsequent effect on the mean flow, diffusivity and stratification?
- What effect does varying the critical inverse Froude Number have on these

quantities?

- How sensitive is the lee wave generation and the lee wave field to changes in the IDEMIX parameters, μ_0, $j_\star$, and τ_v?
- To what extent is the lee wave field able to alter the background internal wave field, and how does this fit with previous estimates of internal wave energy?
- How big of a role does the interaction with the mean flow and the interaction with the background internal wave field play in shaping the lee wave field?
- To what extent is the implementation of the lee wave module in IDEMIX able to explain the discrepancies between the observed dissipation and that predicted by lee wave theory in the Southern Ocean?
- How does the implementation of and the results from a lee wave compartment in an internal wave model advance the research on the role of lee waves in the ocean?

3.1 Models and experimental setups

In order to answer the above outlined research questions, IDEMIX is in this study coupled to the ocean circulation model pyOM - a hydrostatic model in Boussinessq approximation. This will facilitate an assessment of the implementation of a lee wave compartment in IDEMIX. The strengths of pyOM lies in its energy consistency. All forcing, dissipation and interaction between resolved motions and unresolved parameterizations are accounted for in an energy budget, and as such energy of all unresolved motions are carried as prognostic variables in the model to keep track of the energy.

The energy budget contains dynamic and potential terms representing reversible and irreversible energy changes respectively. The mean kinetic energy is forced by winds at the surface, and it has a constant sink of energy to a meso-scale eddy domain via lateral friction and to an unresolved turbulent kinetic energy (TKE) domain. The meso-scale eddy sink term is governed by the closure of Eden and Greatbatch (2008) drawing upon Gent and McWilliams (1990), and the sink to the TKE domain uses the parameterization of Gaspar et al. (1990). Subsequently the eddy kinetic energy (EKE) has an energy sink to the internal gravity wave (IGW) domain (Eden and Olbers, 2014). The IGW domain is governed by IDEMIX, and this is where the new lee wave compartment is added. The original version of IDEMIX is forced by an energy flux from barotropic tides from Jayne (2009) at the bottom and at the surface by an energy flux from the mixed layer into the interior in the near-inertial band, i.e. wind-forcing, from Rimac et al. (2013). IDEMIX contains an energy sink to the TKE domain, which therefore has sources from both the internal wave domain and from the mean field. Additionally there is an irreversible energy exchange from the TKE domain to the potential energy domain, which accounts for heat gain. An overview of this structure of energy stocks and flows is useful for understanding the implementation of lee waves in IDEMIX. Although the lee waves are implemented within IDEMIX, they constitute an energy compartment of its own linked with the mean flow and with the background internal wave field ('background' here meaning the internal wave field present prior to including lee waves) as determined by Eq. 2.46. Such an overview also helps to understand how a possible parameterization of lee wave energy would function in the model. If the lee wave energy is deemed to originate almost exclusively from eddies, a parameterized lee wave field would draw its energy from the meso-scale eddy field, whereas if the eddies were to play only a small part in lee wave generation, the energy would largely stem from the mean kinetic energy.

As a first consideration to investigate the effect of lee waves on the ocean state is the horizontal resolution of the model being used. The resolution could very well have an influence on the lee wave generation, since eddies have been reported to be of great importance in lee wave generation (Marshall and Naveira Garabato, 2008; Nikurashin et al., 2013). An eddy-resolving model could therefore naturally be assumed to have a higher lee wave energy flux than both an eddy-permitting and a coarse resolution model. Furthermore, Hogan and Hurlburt (2000) finds a significant increase in bottom velocity with an increasing model resolution. With the current formulation this also suggest a stronger lee wave generation in a higher resolution model. To test the effect of resolution on lee wave generation two different setups of pyOM have been used; first the global 2° horizontal resolution setup, originally based on the MITgcm, with the vertical dimension converted from 30 to 45 layers, and secondly the 1/3° horizontal resolution FLAME (Family of Linked Atlantic Model Experiments) setup of the North and tropical Atlantic spanning from 18°S to 70°N and has open boundaries at the northern and southern boundaries, and the same 45 vertical layers. While the 2° global model does not capture eddy characteristics at all, the 1/3° would be considered eddy-permitting, i.e. capturing some but not all of the eddy characteristics. The vertical grid spacing is 10m at the surface increasing to 250m below 2000m depth.

The main investigation, however, is carried out in the 1/12° FLAME setup. As opposed to the eddy-permitting setup, this would (by and large) be considered eddy-resolving. The vertical structure remains the same.

The model was first run 10 years spin-up without the lee wave module. After these 10 years the lee wave module was switched on with four different settings specified by the isotropic/anisotropic topographic spectrum and the critical Froude Number set to either $Fr_c = 0.75$ or $Fr_c = 0.5$. For these four different settings the IDEMIX parameters $j_\star = 10$, $\tau_v = 3$ days, $\mu_0 = 4/3$ were taken from Olbers and Eden (2013). A fifth and sixth experiment with the IDEMIX parameters found in Pollmann et al. (2017) ($j_\star = 5$, $\tau_v = 2$ days, $\mu_0 = 1/3$) was used with the isotropic and anisotropic spectrum and both with $Fr_c = 0.75$. Thus we have four topography parameter and two IDEMIX parameter sensitivity experiments using the 1/12° model; one experiment using the isotropic topography spectrum and $Fr_c = 0.75$ on the same model domain but with a coarser horizontal resolution of 1/3°; and one last experiment also using isotropic topography and $Fr_c = 0.75$ but using a global model in a decidedly coarse horizontal resolution of 2°. These last runs using coarser resolution will not be examined in depth, but mostly serve as a validation of the clear hypothesis that the lee wave generation should increase with resolution. The firs six experiments are

- I075, using the isotropic topography spectrum and a critical inverse Froude Number $Fr_c = 0.75$. When differences between the simulation *with* lee waves are discussed, this experiment will be used as a base experiment
- I05, using the isotropic topography spectrum and critical inverse Froude Number $Fr_c = 0.5$
- A075, using the anisotropic topography spectrum and critical inverse Froude Number $Fr_c = 0.75$
- A05, using the anisotropic topography spectrum and critical inverse Froude Number $Fr_c = 0.5$
- P17I, using the isotropic topograpy spectrum, critical inverse Froude Number $Fr_c = 0.75$, and IDEMIX parameters found by Pollmann et al. (2017)
- P17A, using the anisotropic topograpy spectrum, critical inverse Froude Number $Fr_c = 0.75$, and IDEMIX parameters found by Pollmann et al. (2017)
- $1/3°$, using isotropic topography spectrum and cirtical inverse Froude number of $Fr_c = 0.75$ on the $1/3°$ setup
- $2°$, using isotropic topography spectrum and cirtical inverse Froude number of $Fr_c = 0.75$ on the $2°$ setup

After the 10 year spinup the model was subsequently run for one year in each of the experiments. Additionally, one control run was made without the lee wave module. Common for all of the experiments including lee waves is that they use the topography data of Goff (2010). The data is based on satellite altimetry measurements and spans the entire globe, but in Fig. 3.1 it has been interpolated onto the model grid.

Four different topographic parameters are necessary to calculate the lee wave energy flux at the bottom if the full anisotropic spectrum is used. These are the root-mean-square height of the abyssal hills showed in the *upper left panel*. The height of the abyssal hills are large in the central subtropical Atlantic but also along the Mid Atlantic Ridge. Since the bottom energy scales as $F_{bell} \sim h_{rms}^2$, the geographical distribution is very much dependent on h_{rms}. The orientation angle, ϕ, showed in the *upper right panel* is mostly important for the directional distribution of lee wave energy. Since the lee wave energy is in this study integrated over propagation angle, the orientation angle should not be particularly important for the lee wave generation, but it is nonetheless a necessary parameter in the anisotropic topography spectrum. The topographic wavenumber in the strike direction, k_s, is showed in the *bottom left panel* and the topographic wavenumber in the normal direction, k_n is showed in the *bottom right panel*. In general $k_n > k_s$. If the topography is assumed isotropic, we set $k_n = k_s$ and only h_{rms} and k_s is used to calculate the bottom energy flux.

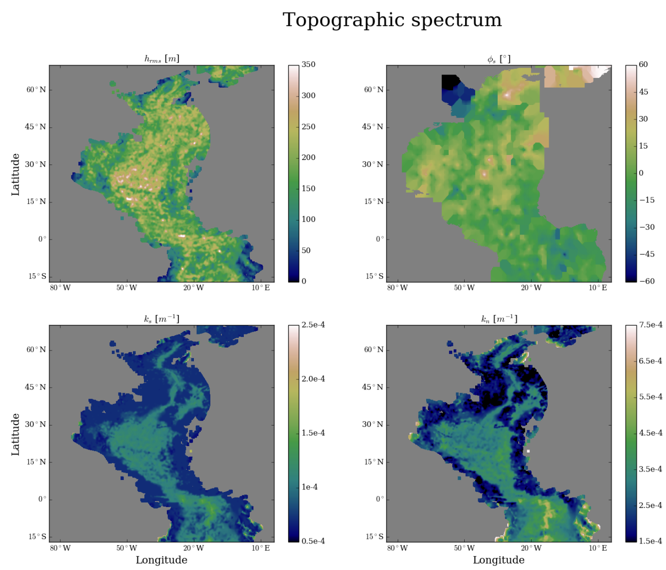

Figure 3.1: The four parameters of the topographic spectrum; *upper left* shows the root-mean-square topographic height, h_{rms}, in meters, *upper right* shows the strike-angle, ϕ_s in degrees, *bottom left* shows topographic wavenumber in strike direction k_s and *bottom right* shows the topographic wavenumber normal to the strike direction, k_n. Both *bottom left* and *bottom right* are in units of $1/m$, but take notice of the different colorbar range. In general $k_n > k_s$.

Chapter 4

Sensitivity to model resolution

The purpose of comparing results from models with different horizontal (and vertical) resolution is to shed light on the effect of model resolution on the magnitude and also distribution of lee wave generation. The major issue in this regard is the importance of the eddy field in contrast to the mean flow. It is still an open question to what extent the lee wave generation is caused mostly by deep reaching eddies or by the mean flow.

4.1 Comparison of two global models

Two experiments on global ocean models were carried out; one model setup using an eddy resolving horizontal resolution of $1/10°$ and one using a coarse horizontal resolution of $2°$. Both model runs have used the isotropic topography spectrum and a critical inverse Froude Number of $Fr_c = 0.75$.

The lee wave energy flux at the bottom (*left panel*) and the bottom speed (*right panel*) from the $2°$ model is plotted in figure 4.1. The lee wave energy flux is between 10^{-6} and $10^{-5} W/m^2$ many areas in the Southern Ocean, tropical Atlantic and central Pacific. In many parts of the midlatitude and northern Pacific, in the midlatitude and western Atlantic, and in the eastern Pacific (from roughly $90°E$ to $135°E$), however, the magnitude is below $10^{-7} W/m^2$. The lee energy flux coincide well with the bottom flow, which exhibits its largest magnitude in the Southern Ocean at around $0.1 m/s$. As already mentioned eddy structures are not visible in neither the bottom speed nor the energy flux.

The same quantities are shown for the $1/10°$ global model in Fig. 4.2. First of all, both the energy flux and the bottom speed is larger compared to that of the $2°$ model, the energy even by an entire order of magnitude in many regions (notice the scale on the colorbar). The energy flux is largest in the midlatitude and northern Atlantic and in the Southern Ocean with values around $10^{-4} W/m^2$; that in the Atlantic is in stark contrast to the energy flux in the $2°$ model with a difference of up to four orders of magnitude. Also the eastern part of the Southern Ocean has an energy flux between 10^{-5} and $10^{-4} W/m^2$ in most areas, which is also between two and three orders of

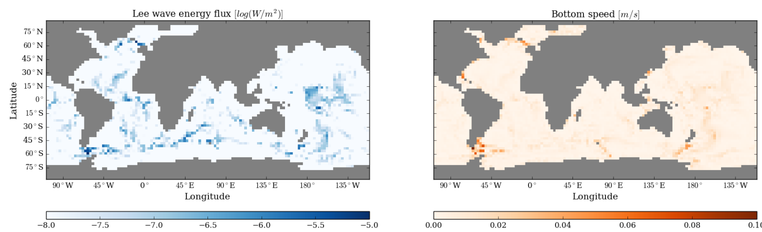

Figure 4.1: *Left panel* shows the bottom lee wave energy flux from the 2° global model. The flux is largest in the Southern Ocean and tropical Atlantic, where it reaches magnitudes between 10^{-6} and $10^{-5} W/m^2$. In the midlatitude Atlantic and Eastern Pacific magnitudes are often below 10^{-7} *Right panel* shows the bottom speed from the 2° global model. The strongest bottom flows occur in the Southern Ocean near Drake Passage with speeds close to $0.1 m/s$.

magnitude larger than that of the 2° model.

The bottom speed in these regions is between 0.1 and $0.2 m/s$. In the case of the North Atlantic this is more than an order of magnitude larger than the 2° model. Since values are averages over a year of simulation, single eddies do not clearly stand out, although an eddy field is clearly visible in both the Southern Ocean, Atlantic and Pacific Ocean. The bottom speed is in many regions twice as larger as that in the 2° model, and there is a visible correlation between the strong bottom flow and the lee wave energy flux in the Atlantic and in the eastern part of the Southern Ocean.

Fig. 4.1 and fig. 4.2 reveal that the discrepancy between the energy flux in the high- and the coarse resolution model is two-fold. First of all, the energy flux in the coarse resolution model is in general an order of magnitude lower in most regions. This goes for regions of both relatively low and high energy flux. Second of all, there are a few regions where the energy flux is several orders of magnitude larger in the high resolution model - the eastern part of the Southern Ocean and the midlatitude Atlantic are the most prominent examples. These are also regions in which the bottom flow is significantly larger in the high resolution model and which are characterized by a vigorous eddy field. As such, both the distribution and and magnitude of lee wave energy flux is significantly different in the high resolution model than in the coarse resolution model, and the difference is likely to linked with larger bottom velocities linked with the eddy field.

Integrated over the entire model domain the lee wave energy flux amounts to $F_{glob} = \int_x \int_y F_{bell} \partial x \partial y = 0.0114 TW$ in the 2° model and $F_{glob} = 0.262 TW$ in the 1/10° model, i.e. more than an order of magnitude larger. This result from the 1/10° resolution model is similar to what other studies of lee wave generation has found (Nikurashin and Ferrari, 2010a; Scott et al., 2011; Trossman et al., 2013; Wright et al., 2014).

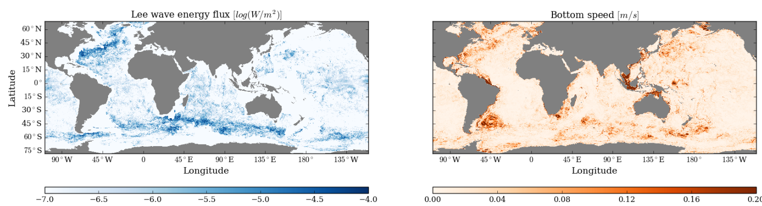

Figure 4.2: *Left panel* shows the bottom lee wave energy flux from the $1/10°$ global model. The flux is largest in the North Atlantic and in the Southern Ocean. Values here are roughly $10^{-4} W/m^2$. *Right panel* shows the bottom speed from the $1/10°$ global model. The strongest bottom flows occur in the Southern Ocean near Drake Passage with speeds close to $0.1 m/s$.

The vertically integrated lee wave energy for both global models is plotted in Fig. 4.3, where *left panel* shows that of the $2°$ model and *right panel* shows that of the $1/10°$ model.

In the $2°$ model the tropical Atlantic and Pacific stands out with vertically integrated lee wave energy of $10^1 m^3/s^2$. The Southern Ocean and the northern Atlantic has a vertically integrated lee wave energy of one or two orders of magnitude lower, which is contrasted to the energy flux, where these regions show the largest magnitudes. The energy thus to a higher degree tends to accumulate in the tropics than in the high latitudes in the $2°$ model. This image is not mirrored in the high resolution model. Here the midlatitude and northern Atlantic stand out with an vertically integrated energy of $10^2 m^3/s^2$, while the Southern Ocean shows magnitudes between 10^1 and $10^2 m^3/s^2$. There is no larger accumulation in the tropics than in the high latitudes. In comparison the energy in the tropical Atlantic and Pacific are of similar, or at least comparable, magnitude in the two models (the energy in the tropical Indian Ocean remains larger in the high resolution model). The image of a difference in the distribution of the lee wave energy flux between the two models is thus somewhat distorted, when it comes to the vertically integrated lee wave energy. Here the difference between the two models is even larger in the high latitudes, whereas the difference in the tropics is reduced.

Since the amount of lee wave energy depends on the balance between the energy flux at the bottom and the energy transfers away from the lee wave field (the energy transfer to the mean field and to the background internal wave field), as specified by Eq. 2.46 (where the transfer between up and downward propagating energy cancels out in the total energy), the large differences in vertically integrated energy the two models in between is not a given, even though the energy flux is larger in the high resolution model. The energy exchange with the mean flow can have either sign (from the lee wave energy field to the mean flow and vice versa), whereas the

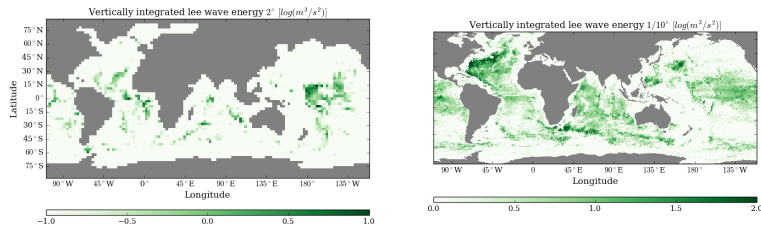

Figure 4.3: *Left panel* shows the vertically integrated lee wave energy from the 2° model. The energy is largest in the tropical Atlantic and Pacific, where values reach $10^1 m^3/s^2$. In most other regions the lee wave energy is two orders of magnitude lower than that. Compared to the energy flux itself, the energy tends to accumulate more in the tropical regions than in the mid- and high latitudes *Right panel* shows the vertically integrated lee wave energy from the 1/10° model. Contrary to the energy flux the largest energy levels are found in the Atlantic along the North Atlantic Current with values of $10^2 m^3/s^2$. In the high latitudes the energy is at least three orders of magnitude larger than that of the 2° model, wheres as the energy levels in the tropical Atlantic and Pacific are of similar magnitude. Notice that the different panel sizes are due to different data dimension and are chosen so as not to distort these dimensions.

energy exchange with the background internal wave field is only in one direction. The energy transfer to the background internal wave field have shown to be the far largest of these two, and is therefore shown for both models in Fig. 4.4.

In the 2° model the internal wave energy transfer remains very localized with magnitudes of $10^{-5} m^3/s^3$ in around the Drake Passage. The overflow regions between the Norwegian Sea and the Atlantic along with the coastal region of western South America also show hightened values, but almost every other region shows values two orders of magnitude lower. In contrast the 1/10° model shows the highest internal wave energy transfers in the midlatitude and North Atlantic and in the Southern Ocean with transfers of $10^{-4} m^3/s^3$. These regions of high energy transfer clearly follow the North Atlantic Current and the Antarctic Circumpolar Current (ACC), as opposed to the localized areas of high energy transfer shown by the 2° model. As such, both the magnitude and the distribution of this energy transfer is thus very different between the models. It is worth noticing that in both cases the the energy transfer does not necessarily show the same distributional pattern as the lee wave energy field itself. In both models the magnitude of the lee wave energy itself in tropical regions is comparable to that in the mid- and high latitudes, whereas regarding the energy transfer magnitudes are far larger in mid- and high latitudes than in tropical regions.

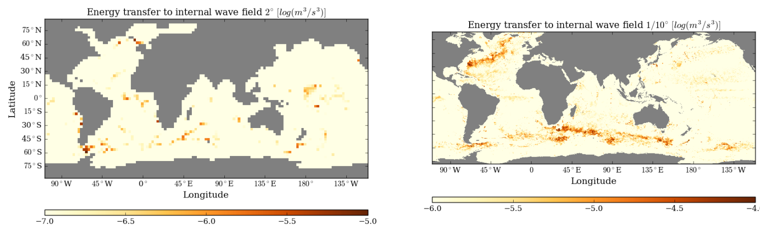

Figure 4.4: *Left panel* shows the vertically integrated energy transfer from the lee wave field to the background internal wave field in the 2° model. The largest energy transfer of $10^{-5} m^3/s^3$ is found around the Drake Passage. *Right panel* shows the same transfer for the 1/10° model. In the high resolution model the large energy transfer of magnitudes $10^{-4} m^3/s^3$ clearly follow the North Atlantic Current and the ACC, where in the coarse resolution model the energy transfer is more localized. In both models mid- and high latitudes show much larger energy transfer than tropical regions.

4.1.1 Conclusion on the comparison of coarse and high resolution models

Overall there are few similiarities and many differences in lee wave generation and dissipation between the coarse 2° resolution model and the high 1/10° resolution model. The bottom speed is in general at least twice as large in the high- than in the coarse resolution model, and large values also appear more localized in the coarse resolution model. The magnitude of both the energy flux, the vertically integrated lee wave energy field, and the energy transfer from lee waves to the background internal wave field are an order of magnitude or more lower in the coarse resolution model than in the high resolution model. This is well illustrated by the globally integrated energy flux of $F_{glob} = 0.274 TW$ in the coarse resolution model and $F_{glob} = 0.0114 TW$ in the high resolution model, i.e. an increase by a factor of roughly 25. There are also differences between the models in the distribution of these quantities. Most noticeable in this regard is the lack of energy and energy flux and transfers in the mid- and northern Atlantic and the eastern part of the Southern Ocean in the 2° model. These are the some of the most energetic regions in the high resolution model. Furthermore, they show bottom speeds of 0.1 to $0.15 m/s$ in the high resolution and only 0.01 - $0.02 m/s$ in the coarse resolution model, which also have clear signs of an eddy signal. It is thus concluded that the eddies generated in the North Atlantic Current and in the ACC have a significant impact on lee wave generation. As such, it is a stronger bottom flow and in particular the coincidence of strong bottom flow associated with eddies with rough bottom topography in the 1/10° model, which generates a much stronger lee wave field. The tropical Atlantic and Pacific, on the other hand, exhibits a lee wave energy flux which is comparable in magnitude in the two models. Another similarity in the two models is that the lee wave energy tends to accumulate more in the tropical regions than in the high latitudes.

If we take the impact of resolving eddies to increase the lee wave generation 25 times (although this cannot be concluded from the current analysis, since changes in mean flow, buoyancy stratification, and even in the interpolation of topography data onto the coarse resolution grid can also have an impact on lee wave generation), it is thus clear that a parameterized lee wave energy flux should be based to a very large extent on the eddy kinetic energy. A further analysis of the consequences of such a parameterization is not the scope of this study, but for elucidating the issue of the impact of lee waves on the overturning circulation for instance (where coarse resolution models are widely used, because of a lower computation time), it should be considered.

4.2 Comparison of an eddy-resolving and an eddy-permitting regional model

The regional FLAME model of the North Atlantic basin was used in two different setups; one being eddy-permitting with a horizontal resolution of 1/3° and one being eddy-resolving with a horizontal resolution of 1/12° (this setup will also be used to test the sensitivity to the lee wave and IDEMIX parameters, but this will be covered in chapter 3). Both setups have been used with the isotropic topography spectrum and a critical inverse Froude Number $Fr_c = 0.75$ in this investigation. The bottom lee wave flux (*left panel*) and the bottom speed (*right panel*) from the 1/3° experiments is shown in figure 4.5. The energy flux is largest in the Denmark Strait where it reaches $10^{-4}W/m^2$. A few areas in the midlatitude north Atlantic shows magnitudes of $10^{-5}W/m^2$, but besides this most areas have magnitudes of $10^{-6}W/m^2$ or lower. The bottom speed reaches $0.1m/s$ in many coastal seas, but in the central Atlantic it is mostly below $0.02m/s$. Some eddy activity along the North Atlantic Current is noticeable, but the translation of these into lee wave generation is minor compared to that in the Denmark Strait. In understanding the translation from bottom speed to the energy flux it needs to be mentioned, that lee wave generation in many coastal regions is inhibited because of the lack of topography data here. This is the reason why many coastal regions with strong bottom flows do not exhibit any lee wave generation. The lack of topography data can either be caused by heavy sedimentation smoothing out the ocean floor, or it can be caused by a limitation in the measuring method (or a combination of the two) (Goff, 2010). The total energy flux integrated over the entire model domain is $F_{glob} = 0.0117TW$ in the 1/3° model.

The same quantities are shown in Fig. 4.6 from the base experiment of the 1/12° model. The energy flux (*left panel*) remains larger than $10^{-4}W/m^2$ in the Denmark Strait, but the magnitudes in the central, western and northern part of the Atlantic are here also between 10^{-4} and $10^{-5}W/m^2$, i.e. at least an order of magnitude and in many areas close to two orders of magnitude larger than in the 1/3° model. Only in

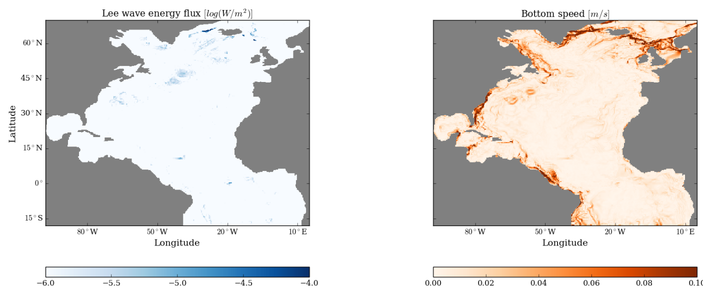

Figure 4.5: *Right panel* shows the bottom energy flux from the 1/3° model. The energy flux reaches $10^{-4} W/m^2$ in the Denmark Strait, but in the central Atlantic it remains at least one order of magnitude lower. *Left panel* shows the bottom speed from the 1/3° model. The bottom speed reaches $0.1 m/s$ in many coastal regions, but in the central Atlantic it is mostly below $0.2 m/s$. Some eddy activity is seen in the western Atlantic, which is also translated into lee wave generation, but the magnitude is small compared to that in the Denmark Strat.

the subtropical and in tropical Atlantic is the energy flux around $10^{-6} W/m^2$, which were common in the 1/3° model. The bottom speed (*right panel*) is also substantially higher than in the 1/3° model. Magnitudes of $0.1 m/s$ is simulated in many areas in the midlatitudes particularly along the North Atlantic Current and in the Western and northern Atlantic. Here the bottom speed also bears a characteristic eddying shape signifying a strong eddy field. Bear in mind here, that the colorbar range has been chosen so as to highlight differences in the central Atlantic rather than in coastal regions, where lee wave generation is inhibited nonetheless. As such, bottom speeds in coastal areas are larger than the maximum showed on the colorbar range. The integrated energy flux in the 1/12° model amounts to $F_{glob} = 0.0628 TW$. This is roughly six times larger than that in the 1/3° model. It shows well, that in many regions the energy flux is about an order of magnitude in the eddy-resolving model. These regions coincide very well with those which exhibit a bottom flow bearing a significant eddy signature. Despite a large difference in energy flux between the two models, this ratio of the two (globally integrated) energy flux is not nearly as large as that of the two energy fluxes from the 1/10° and 2° global models.

As was the case with the two global models, the vertically integrated lee wave energy field is shown for both the 1/12° and the 1/3° model in figure 4.7. In the 1/3° model (*left panel*) the vertically integrated lee wave energy reaches $10^2 m^3/s^2$ in a few areas in the subtropical and tropical Atlantic, whereas the western midlatitude Atlantic also shows significant lee wave energy. The energy thus accumulate a lot more in the tropical and subtropical regions, than in the midlatitudes, where the generation of lee waves is larger. In contrast the 1/12° model exhibits a much larger accumulation of lee wave energy in the western and central part of the Atlantic, but a much lower accumulation in the tropical Atlantic. The magnitudes of vertically

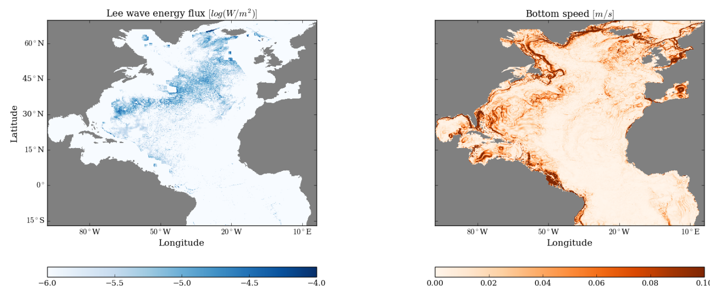

Figure 4.6: *Left panel* shows the energy flux from the base experiment using the 1/12° regional FLAME model. The energy flux reaches a magnitude larger than $10^{-4} W/m^2$ in the Denmark Strait and larger than $10^{-5} W/m^2$ in many areas in the midlatitude western, central and northern Atlantic. *Right panel* shows the bottom speed from the same experiment. Magnitudes between 0.05 and $0.1 m/s$ is not uncommon in many parts of the western and northern Atlantic. The bottom speed bears a significant eddying signature along the North Atlantic Current.

integrated lee wave energy which reached in the two models is actually quite similar, but the distribution of lee wave energy is very different. As was the case with the two global models, though, relative to the energy flux the accumulation of energy is larger in the tropics than in mid- and high latitude; the vertically integrated energy is shifted equator-ward compared to the bottom energy flux.

The energy transfer from the lee wave field to the background internal wave field is shown for both regional models in figure 4.8. The energy transfer is in both models largest in the Denmark Strait, where it reaches $10^{-4} m^3/s^3$. In the 1/3° model (*left panel*), however, the energy transfer does not exceed $10^{-5} m^3/s^3$ in many other parts of the Atlantic. As with the bottom energy flux, this is in stark contrast to the 1/12° model, where much of the midlatitudes exhibit energy transfers larger than $10^{-5} m^3/s^3$. There seems to be an almost one-to-one correlation between the bottom energy flux and the energy transfer in both models.

4.3 Final conclusions on the resolution sensitivity

The most important difference between the eddy-permitting 1/3° and the eddy-resolving 1/12° model setup, in terms of lee generation, energy and dissipation, is the amount lee wave energy generated (and thus also dissipated) in along the North Atlantic Current. Here the magnitude of the energy flux is almost everywhere at least an order of magnitude larger in the eddy-resolving model than in the eddy-permitting one. Although traces of eddy activity is visible in the bottom speed of the 1/3° model, the eddy signature is much more apparent and the bottom speed much larger in this region in the 1/12° model. Whereas the the two global models exhib-

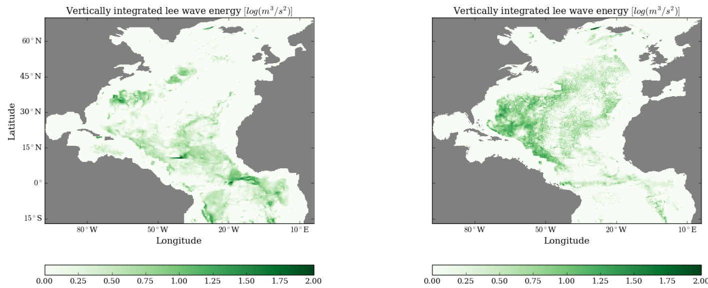

Figure 4.7: *Left panel* shows the vertically integrated lee wave energy from the 1/3° model. Lee wave energy reaches $10^2 m^3/s^2$ in the tropical Atlantic and $10 m^3/s^2$ in the subtropics and western Atlantic. *Right panel* shows the same for the 1/12° model. The highest vertically integrated lee wave energy has roughly the same magnitude of $10^2 m^3/s^2$, but is located in the western Atlantic. As such the increased resolution does not necessarily bring about a stronger lee wave field, but rather affects the geographical distribution of lee wave energy.

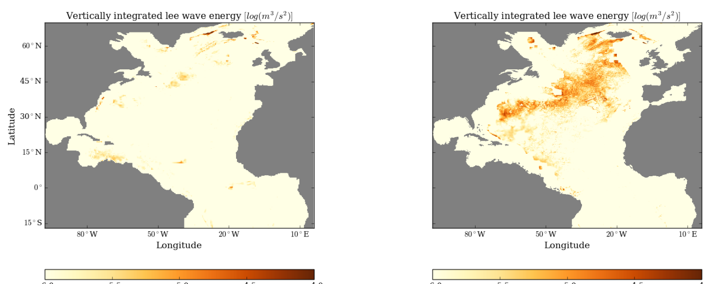

Figure 4.8: *Left panel* shows the vertically integrated energy transfer from the lee wave field to the background internal wave field from the 1/3° model. By far largest in the Denmark Strait the energy transfer is here $10^{-4} m^3/s^3$, whereas much of the rest of the model domain shows magnitudes smaller than $10^{-5} m^3/s^3$. *Right panel* shows the same for the 1/12° model. The highest energy transfer is also here in the Denmark Strait, but much of the central Atlantic also exhibits energy transfer larger than $10^{-5} m^3/s^2$.

ited large differences in both magnitude and distribution of lee wave generation, the difference between the two regional models seems to be mostly in magnitude; the lee waves are generated in the same regions, but in a larger amount in the high resolution model.

As to the question of what impact model resolution and at the same time eddies have on lee wave generation, the answer seems as follows: With a higher horizontal resolution a higher lee wave generation also follows, and the larger degree to which eddies are resolved, the stronger the link between eddy activity and lee wave generation. This is the overall picture on the global scale. In eddy-resolving models lee wave generation is clearly linked with the eddy activity itself, and as such both the magnitude and distribution of lee wave generation is substantially different in high- and coarse resolution models in the current lee wave scheme. Integrated on a global scale the magnitude of the lee wave energy flux is roughly 25 times larger in the eddy-resolving model, than in the coarse resolution model. When eddies are partly resolved the lee wave generation is increased in regions of eddy activity, but it remains lower than when eddies are fully resolved. In the regional model used with two different horizontal resolution the lee wave energy flux is roughly six times larger in the higher resolution model. This was in large part due to the increased lee wave generation along the North Atlantic Current, which also exhibited a clear eddy signature.

Chapter 5

Results from parameter sensitivty analysis in the regional FLAME model

Results and figures in the section below (from the six experiments including a lee wave compartment and the control experiment without lee waves) are all generated using quantities averaged over the last single year of simulation, unless explicitly stated otherwise. Calculating averages over exactly one year eliminates possible bias in magnitudes of different variables due to seasonal fluctuations. Several figures also contain only images from the base experiment with the isotropic spectrum and critical Froude number set to $Fr_c = 0.75$, i.e. the *I075*, but all these have been examined using all parameter settings. Zonally or vertically averaged quantities, for instance, show little difference between the four topography sensitivity experiments, and including images of all four in this section would seem repetitive. The chapter is structured as follows: firstly, results from the base experiment will be presented thoroughly; secondly, several quantities and results from the base experiment will be compared with with results from the control run in order to asses the effect of adding a lee wave module to IDEMIX; thereafter, differences between the four topography sensitivity experiments will be laid out in order to asses the sensitivity of the lee wave module to the topography variables; then follows a comparison of the results from base experiment with results from the two IDEMIX parameter experiments in order to asses the sensitivity the IDEMIX parameters; at last comes an overview and summary.

5.1 Description of base experiment

In this section I will present results from the experiment $I075$, i.e. using isotropic topography spectrum and a critical inverse Froude Number $Fr_c = 0.75$, which I also refer to as the base experiment. To begin with this particular experiment was chosen as a (or rather *the*) reference experiment, because the isotropic topography avoided the computationally expensive numerical integration of the energy flux, and because the critical inverse Froude Number traditionally taken a value close to $Fr_c = 0.75$ (Scott et al., 2011) due to experimental results (Aguilar and Sutherland, 2006). This particular setting has also proven to exhibit neither the largest nor the smallest energy flux and bottom stress. But any of the other four topography sensitivity experiments could have been used as the reference, without loosing the general conclusion, which I will present in due course.

5.1.1 Bottom lee wave energy flux, bottom flow, and bottom stress

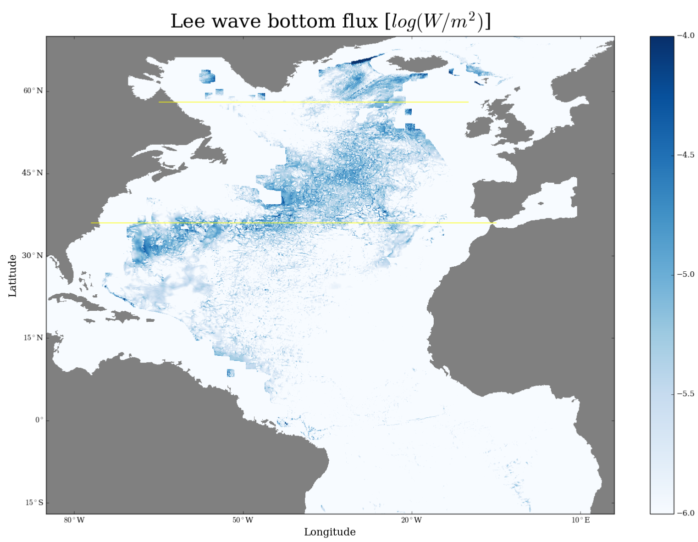

Figure 5.1: The bottom lee wave energy flux is largest along the North Atlantic current and especially in the Northern Atlantic and the Denmark Strait. Notice the logarithmic scale.

The bottom lee wave energy flux F_{I075} is shown in Fig. 5.1. The energy flux is large in the western Atlantic, along the North Atlantic Current, and in the northern Atlantic, with values between 10^{-5} and $10^{-4} W/m^2$ in many areas and in the Denmark Strait where values consistently are close to $10^{-4} W/m^2$. The eastern and especially the tropical Atlantic show very little lee wave generation. Few spots in the Labrador Sea also show fairly large energy flux. The contours of the topography data, which restricts lee wave generation, are clearly seen to influence the geographical distribution of the energy flux - especially in regions of large lee wave generation (for instance in the northeastern Atlantic and the Labrador Sea) - which intuitively seems somewhat arbitrary. The two yellow lines shown in Fig. 5.1 are lines along which transects have been made to show the dependency on depth of certain quantities. The transects of said quantities are drawn along latitudes of $37° N$ and $58° N$ and will be presented later.

The horizontally integrated bottom energy flux of the base experiments is, $F_{glob,IS75} = \int_x \int_y F_{bell} \partial x \partial y = 0.0628 TW$. Along with other main results and differences across the experiments the global energy flux is listed in table 5.1, which will be further elucidated later.

The bottom flow from which the lee wave flux is calculated is plotted in Fig. 5.2. The bottom flow is clearly strongest near coastal boundaries. It is worth mentioning in this regard, however, that Fig. 5.2 does not show the depth from which the bottom speed is taken, and it is to be expected that the bottom speed is larger in regions near land boundaries, where the sea is shallower. Secondly, it is important to keep in mind that the domain of the lee wave generation is restricted by the topography spectrum. Hence, the very strong bottom flow does in some regions not contribute to lee wave generation at all. In general the topography spectrum does not allow for lee wave generation close to land boundaries, although some regions the distance from land with which the topography data is available varies from region to region. These near coastal regions are in many cases also where the bottom flow is strongest. The discrepancy between the ocean domain of the model and the domain of the lee wave generation is visible in Fig. 5.2, since the *right panel* shows the bottom speed where the topography data mask has been applied. Much of both the western and eastern Atlantic, where bottom currents velocities are large, does not allow generation of lee waves due to the lack of topography data. It should be noted that the colorbar range has been selected so as to highlight the difference in bottom speed in the lee wave generation domain as opposed to the entire model domain. In practice, this means that the largest bottom speed in the entire model domain, i.e. the *left panel*, is not really captured here (since this has been deemed not of interest). The strong bottom speed of the Florida east coast and in the western Labrador Sea approaches $0.4 m/s$ rather than $0.1 m/s$, although this is not shown here.

From Fig. 5.2 it can still be seen that eddies modulate the bottom flow in areas away from coastal boundaries. Particularly in the midlatitude western Atlantic, where the bottom flow is around $0.1 m/s$, are the signature of eddies visible. This is of course the eddies in the North Atlantic Current, that are able to modulate even the bottom flow. Also in the North Eastern Atlantic are the eddy field visible, although lee wave generation in this area is largely inhibited due to the topography data. Although the eddy field seems able to affect the bottom flow, very few areas stand out as areas where a single or a very few eddies are able to determine the average flow speed over the entire one year simulation to a very large degree. The fact that the bottom flow bears an eddy signal is in accordance with eddy activity in general eing considered a requisite for lee wave generation (Ferrari and Wunsch, 2009). Over the time scale associated with an internal wave generation the speed with which an eddy passes over topography can be considered quasi-steady, which is why the strong bottom flows associated with deep reaching eddies can generate lee waves. The fact that no single eddy stands out in any areas is also a sign that differences in other quantities are not caused by a single eddy and thus more representative of an average stare.

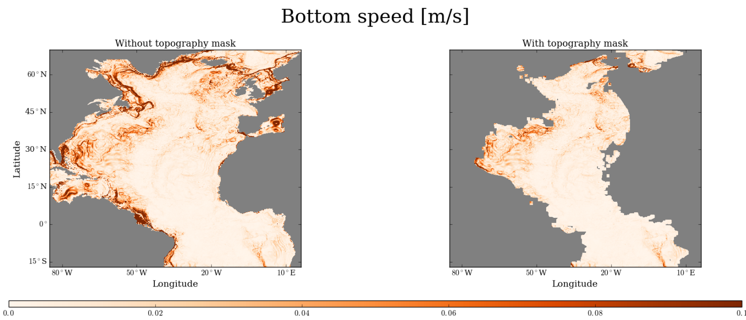

Figure 5.2: The bottom speed is naturally largest near the boundaries, where it is shallower. Large velocities associated with the eddy field is visible in the Western Atlantic and along the North Atlantic Current. Left panel shows the bottom speed in the entire model domain with only land shown in grey. *Right panel* shows the bottom speed with the mask from the topography data set applied greying out regions where lee wave generation is inhibited as well.

The magnitude of the accompanying bottom lee wave stress, $\tau = \sqrt{\tau_u^2 + \tau_u^2}$, is shown in Fig. 5.3. The stress is largest in the northern Atlantic and in the Denmark strait, where it reaches $10^{-3} m^2/s^2$, with significant magnitudes in the central part of the North Atlantic basin - along the Mid-Atlantic Ridge - and in the western Atlantic as well. Southward of 30° and east- and westward of the Mid-Atlantic Ridge the bottom stress in general decreases. The two black boxes in the Denmark Strait and the western Atlantic outline regions in which angle and magnitude of the bottom stress from all four topography sensitivity experiments will be closer examined in section 5.3.2.

Along with the horizontally integrated bottom energy flux, the x- and y-component and the magnitude of the stress, $\tau_{glob} = \int_x \int_y \tau \partial x \partial y$, are all summarized for all experiments in table 5.1.

As mentioned the the signal of a varying eddy field is visible in the bottom speed, why the eddies can to some extent be expected to modulate the bottom lee wave energy flux and hence also the bottom lee wave stress. The evolution of the bottom energy flux and bottom stress over time is thus of interest. Therefore the horizontally integrated bottom flux and bottom stress is plotted as a function of time in Fig. 5.4 (i.e. where other figures show an average over time of a certain quantity, this is not the case for Fig. 5.4). Indeed it can be seen that the bottom stress varies quite a lot over the course of the simulation, whereas the bottom energy flux is more stable. Neither of them exhibit any clear seasonal trend, though. Both the integrated flux and stress have been scaled by their respective maxima, and are thus shown as as a fraction of said maxima. As such, the bottom stress varies from 75% to 100% of its maximum, whereas the bottom stress varies from roughly 90% to 100% of its

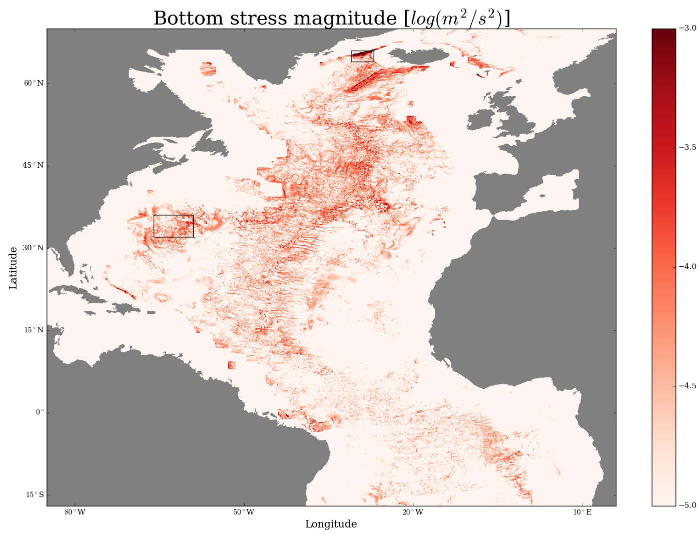

Figure 5.3: Magnitude of the bottom stress caused by lee waves are largest in the western Atlantic, the midlatitude Atlantic and in the Denmark Strait, where it reaches values between $10^{-3} m^2/s^2$ and $10^{-4} m^2/s^2$. In general the stress is large along the Mid-Atlantic Ridge and lower in the eastern and western part of the basin. Black boxes indicate two regions where the differences between experiments are examined.

maximum over the course of the experiment.

In general we can so far determine, that the geographical distribution of the lee wave flux and stress very much follow the strong bottom flow of the North Atlantic Current and the Denmark Strait, as well the rough bottom topography of the Mid-Atlantic Ridge.

5.1.2 The three dimensional lee wave field

A central part in understanding the role of lee waves in the model requires a thorough description of the lee wave field itself. So far, the focus has been on the generation at the bottom, but as the lee wave energy generated at the bottom propagates upwards in accordance with eq. 2.46, it exchange energy with the mean flow and transfers energy to the background internal wave field. The bottom energy flux and these energy transfers will shape the three dimensional lee wave energy field. To get an overview of the distribution of the lee wave energy and its effect on the mean flow, I choose here to focus on vertically integrated quantities.

The effect of the lee waves on the mean momentum is given by the pseudo-

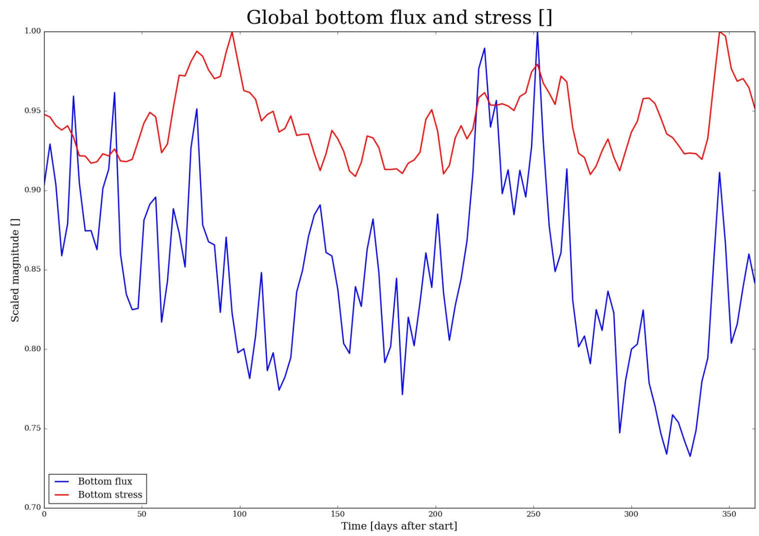

Figure 5.4: The integrated bottom energy flux varies somewhat with time, which could indicate that the eddy field is contributing to lee wave generation in some areas. The bottom stress on the other hand is remarkably steady over the course of the simulation. Notice that both the energy flux and stress have been scaled be their respective maxima and thus appear as dimensionless quantities.

momentum flux determined by Eq. 2.49 and depends on the difference in upward and downward propagating lee wave energy, and on the parameter λ_0. To give an overview of the magnitude and the geographical distribution of the lee wave energy and the pseudo-momentum flux the vertical integral of the these two are plotted in Fig. 5.5 and Fsg. 5.6, respectively. Although they are closely linked, there are also some differences. The lee wave field is very energetic in the western Atlantic, exhibiting magnitudes close to $10^2 m^3/s^2$, where the pseudo-momentum flux is very small. Both reach their maximum across the model domain in the Denmark Strait, with the vertically integrated lee wave energy also here reaching $10^2 m^3/s^2$ and the (vertically integrated) pseudo-momentum flux begin $1 m^3/s^2$, but the pseudo-momentum flux is also large in the far northern and mid-latitude Atlantic, where the lee wave energy is only moderate. Taking the logarithmic scale into consideration, it is worth noticing that both the lee wave energy and the pseudo-momentum flux points toward large local differences and hotspots of lee wave activity in the western and northern Atlantic, near the Mid Atlantic Ridge, and in the Denmark Strait, although the pseudo-momentum flux in general exhibits an even more "hotspot-like" distribution compared to the lee wave energy.

Although the distribution with depths is lost Fig. 5.5 easily give and overview of

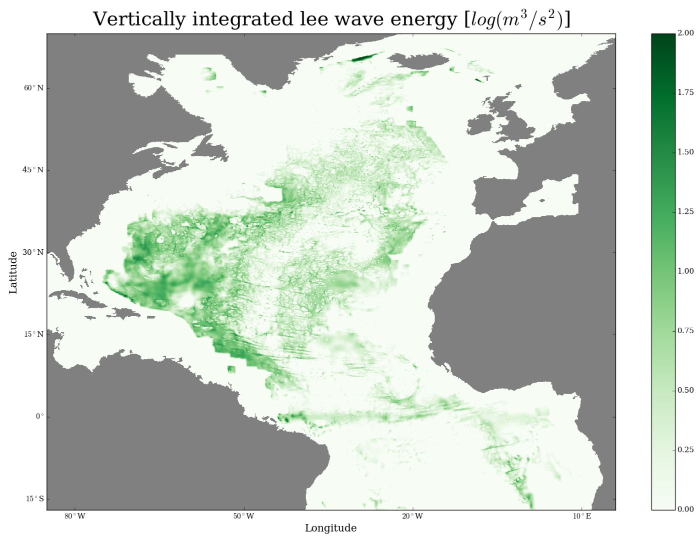

Figure 5.5: The vertically integrated lee wave energy is largest in the western Atlantic and in the Denmark Strait.

the geographical distribution of the lee wave energy.

To put the lee wave energy into perspective the (logarithm of the) ratio of vertically integrated lee wave to background wave energy, $R = \frac{\int_z E_{lee}\partial z}{\int_z E_{iw}\partial z}$ is plotted in Fig. 5.7. Here it is clear that in many regions, the lee wave energy constitute a major fraction of the total internal wave field. Only in a few regions in the North Atlantic where lee waves are generated, is the background wave field more energetic throughout the water column, and especially in the subtropical and mid-latitude Western Atlantic is the lee wave field stronger. In the Southern part of the Atlantic the background wave field seem more energetic than the lee wave field in general. In most areas where lee wave generation is inhibited due the topographic spectrum (i.e. near the coastal regions) the background internal wave field is much more energetic (in many of these regions the ratio is not even captured in the figure because it is outside the colorbar range), although this is not the case in subtropical Eastern Atlantic. A possible explanation for the lee wave energy in this region could be the waves generated at depths travelling to the Eastern Atlantic, but it could also be because of an energy transfer from the mean flow to the lee wave field (this subject will be covered in section 5.1.4). Besides the lee wave activity in the Eastern Atlantic it is noticeable that the lee wave field dominate the background near Iceland and in the Denmark Strait. The stronger lee wave field close to the British Isles and near the Eastern coast of Greenland is not reproduced in Fig. 5.5 and is thus considered to be the result of

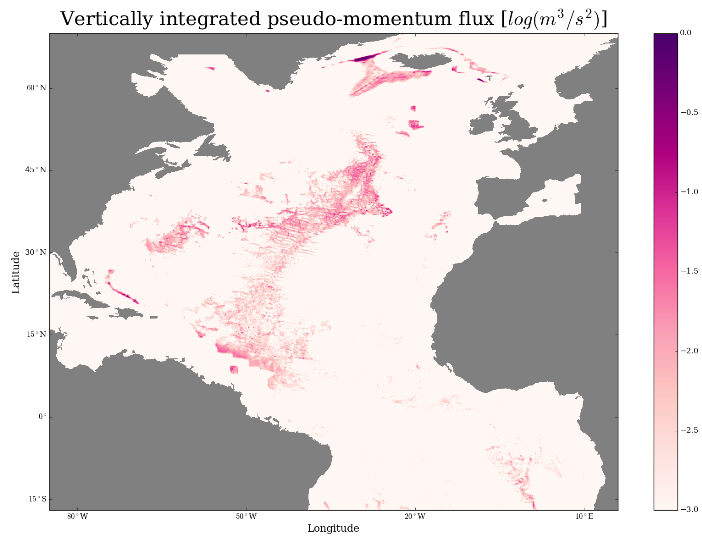

Figure 5.6: The vertically integrated pseudo-momentum flux is largest in the Denmark Strait and in the northern and mid-latitude Atlantic.

a particularly weak background internal wave field. The global (i.e. horizontal and vertical) integral of the lee wave energy $E_{lee,glob} = \int_z \int_y \int_x E_{lee} \partial x \partial y \partial z = 8.33 \cdot 10^{13} J$, and the background IW energy $E_{IW,glob} = \int_z \int_y \int_x E_{IW} \partial x \partial y \partial z = 6.32 \cdot 10^{13} J$, makes it clear that the lee wave field is a significant part of the total internal wave field.

In order to gain a perspective of the effect of lee waves as a function of depth the lee wave energy (*upper panel*) and the pseudo-momentum flux (*lower panel*) is shown in a transect at $37° N$ in Fig. 5.8. The lee wave energy reaches $10^{-2} m^2/s^2$ near the bottom in most of the transect. The vertical extent with which the lee wave energy is dissipated varies along the transect - in most of the western part the lee wave energy is by and large dissipated in the bottom most layer, whereas along the elevated topography (the rise of the Mid-Atlantic Ridge) in the central and eastern part the lee wave energy is dissipated in the bottom most $1000 - 1500 m$. This could be either due to a difference in the transfer to the background internal wave field or in the energy transfer to/from the mean flow (energy transfers will be elucidated in section 5.1.4)

Between roughly 40 and 25°W the rise of the Mid-Atlantic Ridge facilitates lee wave activity which results in a pseudo-momentum flux on the order of $\mathcal{O}(10^{-4}) m^2/s^{-2}$, but also minor topographic features close to 60°W are captured by both the model grid and the topographic spectrum, which give rise to a wave-mean flow momentum exchange. Both the lee wave energy and the pseudo-momentum flux remains, however, fairly localized and basically not present in a very large part of

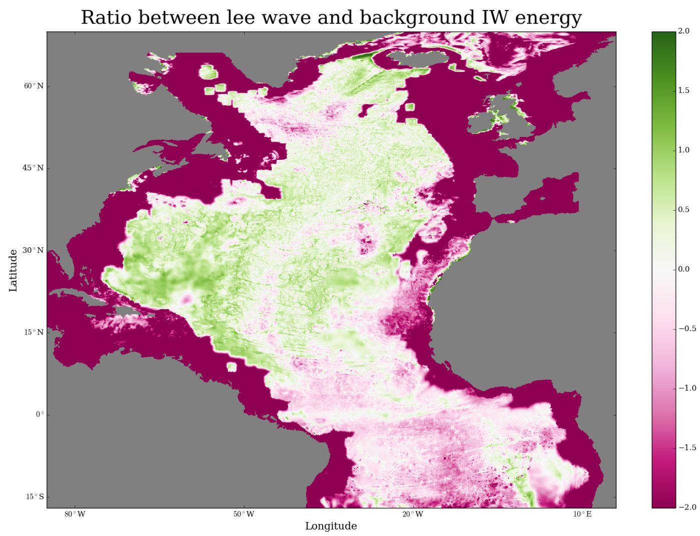

Figure 5.7: The ratio of vertically integrated lee wave and background energy shows the background internal wave field is in much of the ocean up to 10 times, but also that in few hotspots lee wave energy dominate by the same factor. Values are $log(R)$

the transect. It is also worth noticing that even though there is quite a lot of lee wave energy near the bottom both west and east of the Mid-Atlantic Ridge the pseudo-momentum flux remain basically non-existing in these regions.

Together with the vertically integrated lee wave energy Fig. 5.8 gives a good overview of the three dimensional lee wave field. The western Atlantic holds a great deal of lee wave energy, but it remains very concentrated near the bottom. Near and along the Mid-Atlantic Ridge the lee wave field is not as energetic, but the energy propagates farther upwards in the interior. In much of the eastern Atlantic the lee wave energy is negligible.

5.1.3 Zonally averaged quantities

Whereas Fig. 5.5 loses the variation of lee wave energy with depth, Fig. 5.8 remains an image at a single latitude. Showing quantities in two dimensional images (whether it is along the x-plane or z-plane) obviously reveals an inherent problem when trying to describe a three dimensional field. One ultimately loses the distribution or magnitude along the third axis. Because of the hypothesized role of lee waves driven vertical mixing as a potential driver of the overturning circulation (MacKinnon et al., 2017) an appropriate and potentially rewarding investigation is that which reveal the meridional and vertical distribution of lee wave energy and the effects

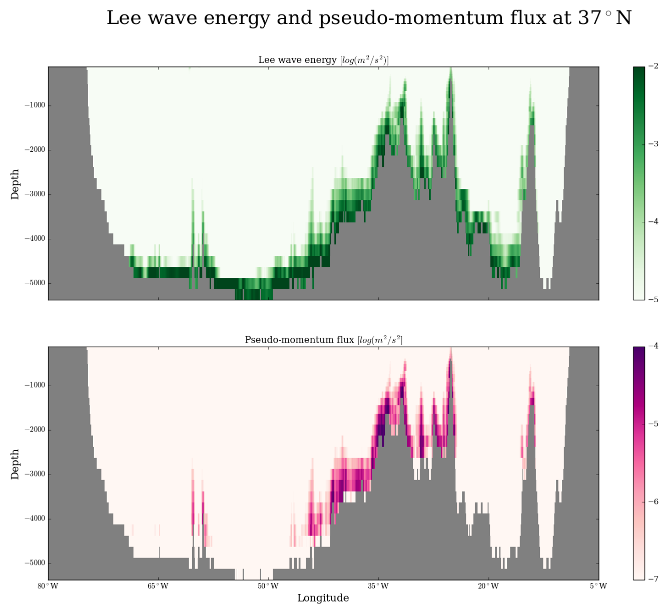

Figure 5.8: Lee wave energy and pseudo-momentum flux from lee waves in a transect at $37°N$. The lee waves itself is large near the bottom at all longitudes, but the pseudo-momentum flux only remove momentum from the mean flow between roughly 55° and $30°W$. Here the pseudo-momentum flux act on roughly the bottom $1000-1500m$ of the ocean at their generation site. Notice values are logarithmic values of actual energy and pseudo-momentum flux.

thereof. In the coming subsection I therefore neglect the zonal distribution of the quantities in question by zonally averaging them. This will provide insight to which latitude and at which depths lee wave generation will have the most influence on diffusivity and mean flow. The zonal average of the pseudo-momentum flux is depicted in Fig. 5.9. Here it is important to keep in mind the variation of the bottom topography with longitude, which is not visible. Therefor the visible bottom topography is also the *deepest* topography at the latitude in question. Along such latitude the topography varies. The lee wave generation and thus the pseudo-momentum flux follows the bottom topography and hence the pseudo-momentum flux is fairly evenly distributed throughout the water column between 5000 and $2000m$ depth. Close to $40°W$ a large amount of momentum is even transferred at $1000m$ depth owing to rise of the Mid Atlantic Ridge at this latitude, which is also visible in Fig. 5.8. In the zonally averaged sense, though, the lee waves generates the largest pseudo-momentum flux of around $10^{-4}m^2/s^2$ close to $60°N$ between $1800m$ depth and the surface. This large activity is also visible as the bottom lee wave stress and energy flux in North Atlantic and Denmark Strait in Fig. 5.1 and Fig. 5.3.

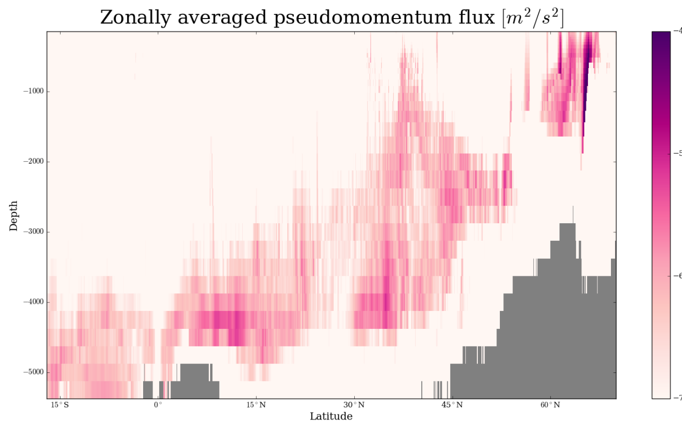

Figure 5.9: The zonally averaged pseudo-momentum flux shows a large drag the mean flow between roughly $5000-2000m$ depth and between the equator and $55° N$. The largest drag on the mean flow, though, occurs close $60° N$ between $1800m$ depth and the surface.

The zonally averaged lee wave energy is plotted in Fig. 5.10, which shows that on average, the lee wave activity is largest below $4000m$ depth, where it reaches $10^{-3} - 10^{-2} m^2/s^2$ on average. In the regions where the depth of the Atlantic reach $5000m$, the lee wave energy is on average $10^{-2} m^2/s^2$ almost everywhere. This is the lee wave energy generated in the very deep western Atlantic. One must bear in mind, though, the spatial distribution of the lee wave activity indicated in Fig. 5.1 and Fig. 5.3. The zonally averaged lee wave energy does show, however, that despite hotspots in the mid-latitudes lee waves are also present and provide significant energy in the tropical Atlantic, although they exchange most of their energy before before reaching mid-depth. Towards the northern Atlantic the lee wave energy is concentrated at shallower depths all the way close to the surface north of $65° N$. This is the lee waves generated near and in the Denmark Strait

Interestingly, there are certain discrepancies between the depths at which the lee wave energy and the pseudo-momentum is largest. As mentioned previously, the pseudo-momentum flux depends on the difference in the upward and downward propagating lee wave energy and on the parameter λ_0. Naturally the energy difference is largest near the bottom, but the effect of a lower λ_0 causes the pseudo-momentum flux at the very deep Atlantic to be vanishing. It is also worth mentioning that the the very large pseudo-momentum flux at $1800 - 1000m$ depth close to $60° N$ is not as prominently seen in the zonally averaged lee wave energy.

To give a full understanding of the spatial distribution of lee wave activity the zonally averaged lee wave energy in Fig. 5.10 must be considered in combination with the vertically integrated lee wave energy shown in Fig. 5.5. The lee wave energy is most heavily concentrated in the subtropical western Atlantic which is an

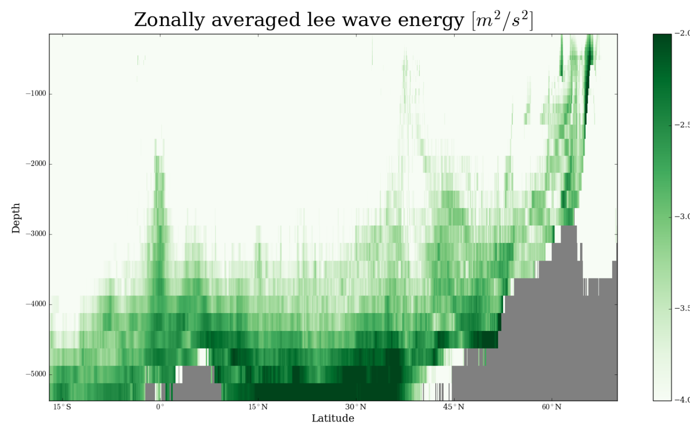

Figure 5.10: The zonally averaged lee wave energy is largest near the bottom. Contrary to the pseudo-momentum flux it is nearly everywhere largest in the bottom most grid cells

area dominated by strong eddies, the signal of which is still somewhat visible in Fig. 5.2 of the bottom flow. In this region the lee wave energy is located at depths below 4500m. Besides the western Atlantic there is a hotspot of lee wave close to and in the Denmark strait, where the lee wave energy is located close between roughly 1500m depth and the surface. The bottom flow in this area is not to the same degree dominated by the eddy field, but there is a strong bottom mean flow.

The lee waves are allowed to exchange energy with the background wave-field assumed to attain a GM shape via the third term on the right hand side in Eq. 2.46, $\alpha_{ww} E_{GM} E_{lee}$. In other words, the energy exchange between the lee wave field and the background internal wave field is given by the product of the two. Therefore, the distribution of the background internal wave energy, and a sense of proportions of the magnitudes of the lee wave and background wave field energy is important in order to gain a full perspective of the role of lee waves. To compare the two, the zonal average of the background internal wave field is shown in Fig. 5.11.

The first thing to notice is the vertical distribution; whereas the lee wave energy is largest below $4000m$ depth, the background internal wave field is largest in the uppermost 1500m or so. It is also noticeable, that the background internal wave field is strongest south of 15°N, while the lee wave activity is strongest northward of that latitude. It also seems clear that the background internal wave energy is much more evenly distributed throughout the water column (keeping the logarithmic color scale of the zonally averaged lee wave energy in mind). It should be kept in mind, though, that the zonally averaged quantity does not capture the zonal distribution, and that both the two wave fields and the pseudo-momentum flux are three dimensional fields. There area also indications that the lee wave field is able

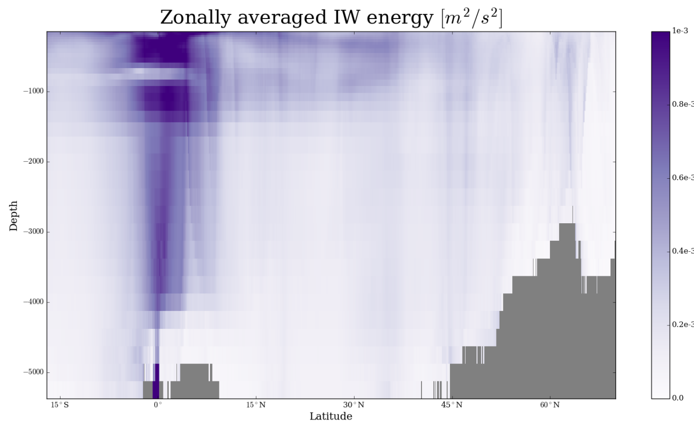

Figure 5.11: The zonally average internal wave energy

to significantly influence the background internal wave field - even in a zonally averaged sense. Close to $48°N$ and $60°N$ there are clear deep reaching tongues of high internal wave energy correlating very well with regions of large amounts of lee wave energy.

5.1.4 Energy transfers

So far I have mostly touched upon the lee wave energy itself, and only briefly mentioned the energy transfer between the lee wave and the background wave field, and the momentum transfer between lee waves and the mean flow. To put the lee wave energy field into perspective also requires a description of the energy transfer from the lee wave field to both the background internal wave field and to the mean flow. These energy transfers will be highlighted in the following section.

The propagation and energy transfer of the lee waves are determined by Eq. 2.46, where the second and fourth term on the right hand side represent the energy exchanges with the mean flow and the background internal wave field, respectively. The energy exchange with the mean flow can be of either sign (for both the up- and downward propagating lee waves), but a non-zero exchange requires wave breaking according to the non-acceleration theorem (Andrews and Mcintyre, 1976; Boyd, 1976). Fig 5.12 shows the energy transfers from the lee wave field at $37°N$. The *upper panel* shows the transfer to the background internal wave field, which follows very closely the distribution of the lee wave field itself. It reaches its maximum of $10^{-7} m^2/s^3$ over the Mid-Atlantic Ridge and below $4000m$ near $45°N$. Both the energy transfer to (*middle panel*) and from the mean flow (lower panel) are everywhere at least an order of magnitude lower than to the internal wave field. Both are located (in significant magnitudes) almost exclusively over the Mid-Atlantic Ridge.

The first and third terms on the right hand side of Eq 2.46 are the vertical diver-

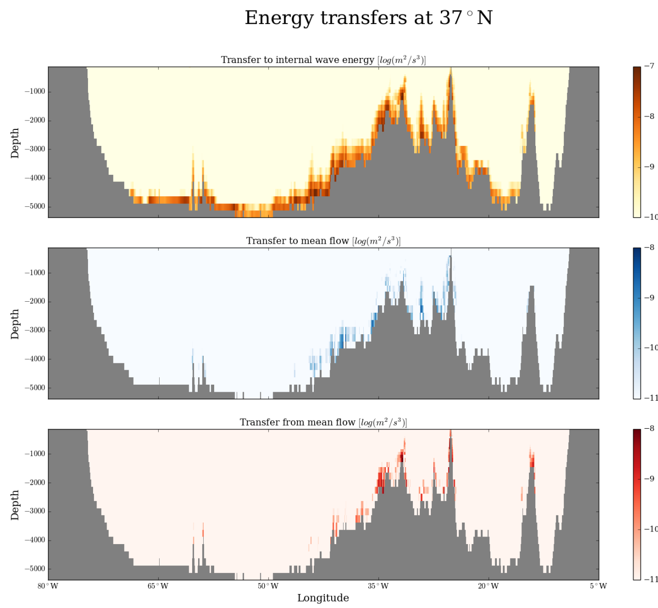

Figure 5.12: The *upper panel* shows the energy transfer to the background internal wave field. Its distribution follows very closely the distribution of the lee wave field and reaches maxima of $10^{-7} m^2/s^3$ near the bottom over the Mid-Atlantic Ridge and below $4000m$ depth near $45°N$. The *middle panel* shows the transfer to the mean flow, which is very localized over the Mid-Atlantic Ridge. The *lower panel* shows the transfer from the mean flow to the lee wave field. This transfer also shows maxima over the Mid-Atlantic Ridge. In general the mean flow exchanges are at least an order of magnitude smaller than the transfer to the internal wave field.

gence in lee wave energy flux and the exchange between up- and downward propagating lee wave energy respectively. Whereas the vertical divergence is visible in the transect, it vanishes when integrating vertically. Furthermore, the exchange between up- and downward propagating energy does not alter the total energy. As such, vertically integrating Eq. 2.46 leaves only the the energy exchange with the background internal wave field and the mean flow as the true ways in which the lee wave field loses energy (keeping in mind that the interaction with the mean flow can also transfer energy to the lee wave field).

Fig. 5.13 shows the vertically integrated lee wave energy (*upper left panel*) along with the vertically integrated energy transfers to the internal wave compartment (*upper right panel*) and to (*lower left panel*) and from the mean flow (*lower right panel*) for the base experiment. The magnitudes of the energy transfer rates amount to roughly 10^{-5} times the lee wave energy itself (in a vertically averaged sense) and their magnitude correspond well with the lee wave bottom energy flux shown in Fig.

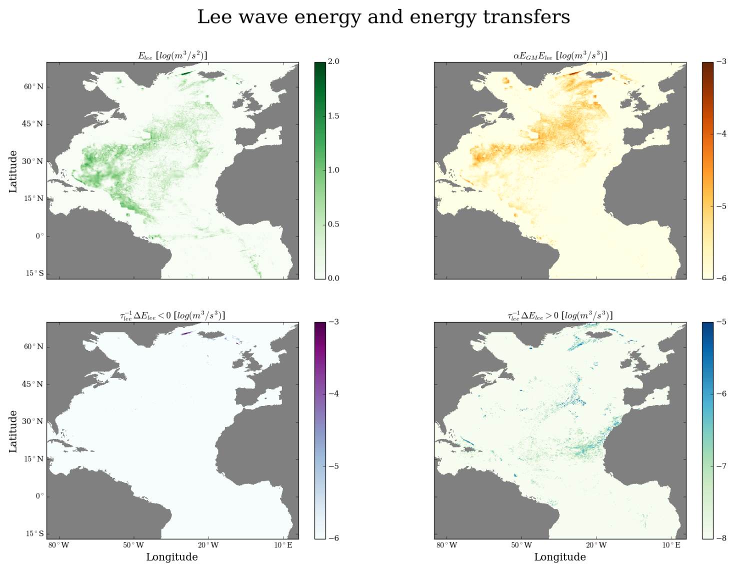

Figure 5.13: The *upper left panel* shows the vertically integrated lee wave energy. The *upper right panel* shows the energy transfer to the background internal wave field, which is the largest energy transfer in a vertically integrated sense. The *lower left panel* shows the energy transfer from the lee wave compartment to the mean flow. This is very localized with a very large transfer in the Denmark Strait but very small in the rest of the model domain. The *bottom right panel* shows the energy transfer from the mean flow to the lee wave compartment. This transfer happens predominantly in the eastern subtropical or in the Northern Atlantic, but it is in general a factor of 10 or more smaller than the transfer to the internal wave compartment.

5.1 (there should naturally be a balance between the energy flux at the bottom and the total transfers in a vertical average).

Overall the largest energy transfer is clearly that to the background internal wave compartment. This transfer reaches magnitudes of $10^{-3}\, m^3/s^3$ in the Denmark Strait and is an order of magnitude or two lower along the North Atlantic Current. Over much of the model domain, the transfer to the background internal wave field is two or three orders of magnitude larger than the transfer both from and to the mean flow, although the Denmark Strait is an outlier in this regard. Here, the energy transfer to the mean flow roughly equals that to the background internal wave domain. Interestingly, the energy transfer to the mean flow in the Denmark Strait, which is roughly $10^{-3}\, m^3/s^3$, is two orders of magnitude larger than the energy exchange with the mean flow (to or from) in any other region (in the vertically integrated sense). The energy transfer from the mean flow to the lee wave compartment is largest in the north Atlantic and near the Mid Atlantic Ridge, where it is around $10^{-5}\, m^3/s^3$. In general the energy transfer to and from the mean flow seems more localized than than to the background internal wave compartment. Considering the magnitudes of the energy transfers the total lee wave energy field can thus be considered, as an approximation, to be in a balance between the bottom energy flux and the transfer to the background internal wave field in many regions except the Denmark Strait. There are, however, geographical differences between the total lee wave energy and the transfer to the internal wave field, which are interesting. South of $30°N$ there are many regions where the lee wave energy is quite large, but the transfer away from lee waves is quite small. This again correspond well with the bottom energy flux shown in Fig. 5.1 also being small in these regions, but it is interesting that significant amounts of lee wave energy is able to persist here nonetheless. This of course matters little for the diffusivity simulated by the model, but it still acts as a good example of how the amount of lee wave energy in a water column is not only a function of the bottom energy flux, but a balance between the bottom flux and the energy transfers.

The amount of energy provided by the lee wave field for mixing is proportional to the energy transfer to the background internal wave field determined by the fourth term in Eq. 2.46, and thus governs the increase in diffusivity due to lee waves in the current formulation. As such, the *upper right panel* of Fig. 5.13 also represents an image of where the lee wave field is able to affect the diffusivity as modelled by IDEMIX. The separation of the lee wave energy from the background energy is due to their different spectral shapes, although the influence on diffusivity of the lee wave and background (or GM) internal waves, does maybe not warrant this separation (more on this in section 7).

Together Fig. 5.12 and 5.13 provides a clear image of the energy transfer to the internal wave compartment as the largest energy transfer and thus main route through which lee wave energy dissipates in the current model formulation.

5.1.5 Summary of description of the base experiment

All in all the base experiments show a lee wave energy flux at its largest along the North Atlantic Current, in the northern Atlantic and the Denmark Strait, where it reaches $10^{-4}W/m^2$. Over the entire model domain the total lee wave eneryg flux amounts to $0.0628TW$ (this is roughly a quarter of previous estimates of a *global* lee wave energy flux (Scott et al., 2011; Trossman et al., 2013)). In the current model implementation the lee wave field exist in a balance predominantly between the bottom energy flux and the energy transfer to the background internal wave field, since this transfer constitutes by far the largest route, through which the lee wave energy dissipates. On average the lee wave energy is by far largest below $4500m$ depth, whereas the pseudo-momentum flux, the vertical divergence of which enters the mean residual momentum equation, is largest above $4200m$ depth. This energy is potentially able to significantly alter the internal wave field, though. Vertically integrated the lee wave energy can be up to 100 times larger than the background internal wave energy depending on the region in question.

5.2 Effect of a lee wave module - difference from control run

After the thorough description of the base experiment, I now turn my attention to the effect of adding a lee wave module to IDEMIX. This is best done by a comparison with the control experiment (i.e. the experiment without lee waves). In theory the control experiment can be compared with any of the topography sensitivity experiments, but for simplicity I have opted to only compare the control experiment with the base experiment - that which I will also use as a reference in the comparison with other experiments in sections 5.3 and 5.4. In the following section I will focus on the mean flow, the buoyancy frequency and the diffusivity.

The effect of the lee waves as a function of depth is important, not only because of the removal of momentum from the mean flow, but also because of the fact that the internal wave field gives rise to a vertical mixing via their breaking. As mentioned in the introduction internal wave breaking is and important driver of the large scale ocean circulation, and one of the important aspects in this process is the depth at which this mixing occurs. This raises the question of whether or not the breaking of lee waves increases the diffusivity in the interior ocean, and if so where the increase occurs. The difference in vertical diffusivity is therefore an important aspect of the experiment, although, as mentioned, the lee wave field is only indirectly linked to the diffusivity via the energy transfer to the background internal wave field. It is important to remember that, in the control run the internal wave field is still modelled by IDEMIX, so the vertical diffusivity is still calculated on the basis of internal wave dynamics caused by winds and internal tides.

5.2.1 Linking the lee wave energy field with the diffusivity

To complete the understanding of the spatial distribution and magnitude of the lee wave energy field and the effect on stratification and diffusivity, the transect at $37°N$, showing lee wave energy and pseudo-momentum flux in Fig 5.8, is broadened to include other quantities as well and supplemented with another transect at 58°N. A more thorough and clearer image of the effect of the lee wave field on diffusivity is presented (by comparing them directly with other key quantities) in Fig. 5.14 and Fig. 5.15. The first latitude was chosen because of the large amount of lee wave energy apparent in Fig. 5.5, and the second was chosen due to the difference in lee wave flux across the Atlantic from west to east as apparent in Fig. 5.1.

In Fig. 5.14 the lee wave energy in the *upper left panel* is largest near the bottom in the western section of transect. Almost no lee wave energy is generated on the eastern side of the Mid Atlantic Ridge. This panel is similar to the upper panel in Fig. 5.8. The energy transfer from the lee wave to the internal wave compartment is plotted in the *upper middle panel* and correlates fairly well with the lee wave energy itself. The internal wave energy is shown in the *upper right panel*, with magnitudes between 10^{-4} and $10^{-3} m^2/s^2$ in much of the western part of the transect. In Fig. 5.14 is also shown the relative differences in both internal wave energy (*lower right panel*) and in the buoyancy frequency (*lower middle panel*). Here

- and in the rest of this section - the difference and relative difference between the base experiment and the control experiment is calculated as $\Delta X = X_{I075} - X_{ctrl}$ and $\Delta X_{rel} = (X_{I075} - X_{ctrl}) / X_{ctrl}$, respectively. In other words, a positive difference in a certain quantity indicate that adding the lee wave module caused an increase in the quantity in question. There is a clear increase in internal wave energy at $45°W$ of more than three times the internal wave energy from the control experiment throughout the entire water column, which coincides very well with a transfer of lee wave energy near the bottom. A smaller but still visible transfer of lee wave energy close to 60°W also contributes to increase the background internal wave energy in the entire water column. In general the internal wave energy is increased in the entire transect and by more than 50% in most of the western part of the transect, where energy transfer from lee waves is prominent near the bottom.

The fact that the relative increase in internal wave energy persists through out the water column shows that the vertical propagation of internal wave energy is potentially very important to consider, when estimating the influence of lee waves on the diffusivity. The diffusivity difference, $\kappa_{I075} - \kappa_{ctrl}$, shown in the *bottom left panel*, can be as large as $\pm 0.1 m^2/s$ near the bottom, but in the interior such large values are not present. The large differences in diffusivity correlates very well with the relative difference in buoyancy frequency (*bottom middle panel*). Although the internal wave energy shows a large increase, relative to control run, in the interior, this does not translate into diffusivity differences, which are numerically as large as those at the bottom. Although not shown here, it is the case that the relative difference in diffusivity in the interior is large even though the numerical difference is not (as compared to that near the bottom), while the relative difference near the bottom is not very large (this is shown in section A of the Appendix). With this in mind, the energy transfer from the lee wave to the internal wave compartment serves to increase the diffusivity in the interior rather than near the bottom.

A second transect at $47° N$ is shown in Fig. 5.15. The lee wave energy (*upper left panel*) reaches magnitudes of $10^{-2} m^2/s^2$ near the bottom between 40° and $15° W$ and generally decrease by an order of magnitude within the bottom most $500m$. The energy transfer to the internal wave field (*upper middle panel*) is largest on the western side and at the top of the ridge near $28° W$, where it reaches $10^{-7} m^2/s^3$. On the eastern side of the ridge the energy transfer decreases towards the east. This is mirrored in the internal wave energy (*upper right panel*) which is elevated on the western side of the ridge as opposed to the eastern side (disregarding the very large values at the eastern shelf, which has not correlated to the lee wave energy at all). The internal wave energy is increased by more than a factor of three throughout the water column in most of the western side of the ridge (*lower right panel*). On the eastern slope of the ridge the increase is smaller but still significant, until roughly $15° W$ east of which changes are insignificant. This is in almost perfect alignment with the energy transfer from the lee wave field, which is lower on the eastern side of the ridge and more than two orders of magnitude lower than its maximum east of $15° W$.

Despite this large increase in internal wave energy on the western side of the ridge the diffusivity exhibits largest numerical differences (*lower left panel*) near the bottom on the western side of the ridge, where it is decreased by up to $0.05 m^2/s$.

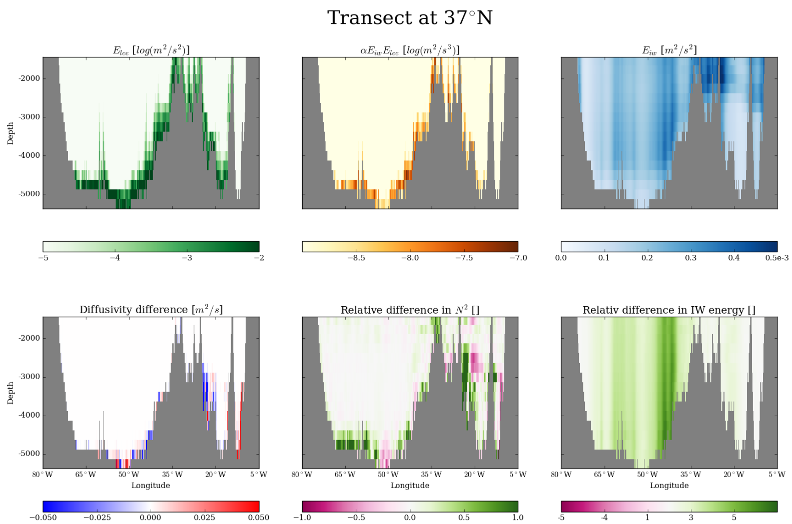

Figure 5.14: Key variables at 37°N: *Upper left*: Lee wave energy is largest near the bottom west of 40°W; *upper middle*: The energy transfer between the lee wave and background internal wave domain follows largely the distribution of the lee wave energy; *upper right*: the background IW energy is fairly evenly distributed over the transect, but the magnitude is significantly lower than the maximum lee wave energy and it decreases towards the bottom; *lower left* the diffusivity difference is by far numerically largest near the bottom, where it is both negative and positive. Values of $\pm 0.1 m^2/s$ are significantly higher than the canonical Munk value of 10^{-4}; *lower middle*: the relative difference in N^2 is little throughout much of the transect but near the bottom it is of larger magnitude (both negative and positive). Close to 20°W there is a region of rather large magnitude, which is replicated as a decrease in diffusivity; *lower right* the relative difference in background internal wave energy is very large throughout the western part of the transect. It is very clear that the transfer of lee wave energy near the bottom just west of $40° W$ is seen throughout the water column in as an increase in internal wave energy. It is, however, not as apparent in the diffusivity.

This decrease correlates well with an increase in buoyancy frequency (*lower middle panel*) near the bottom here of roughly an order of magnitude. There are also large difference in the diffusivity in the interior near $1500 m$ depth, which correlate well with changes in the buoyancy frequency. As is the case at 37°, the largest numerical differences in diffusivity is thus related to changes in the buoyancy frequency, but these differences occur in regions with already very high diffusivity due to a low buoyancy frequency. In section A of the Appendix, it is shown that the relative difference in diffusivity is by far largest in the interior on the western side of the ridge, where it is increased by more than an order of magnitude, and is thus clearly related to the energy transfer from the lee wave field to the internal wave field.

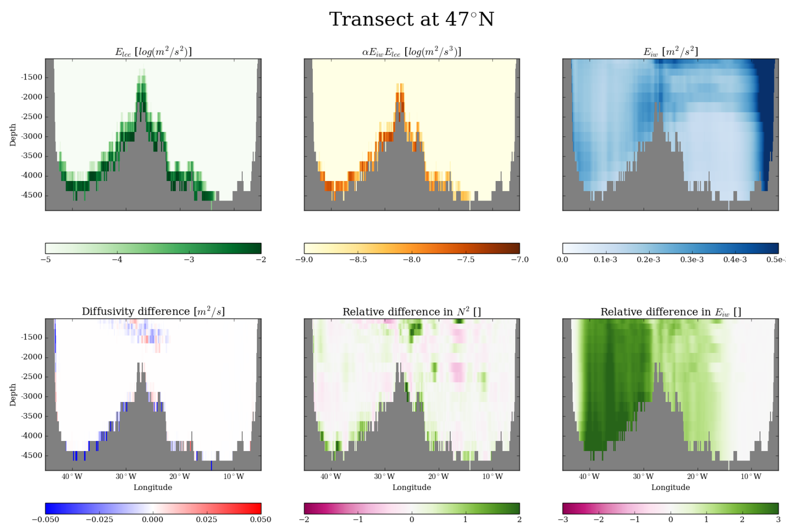

Figure 5.15: The lee wave energy (*upper left panel*) is largest on the west of roughly 15°W, where it reaches $10^{-2} m^2/s^2$ near the bottom. The energy transfer to the background internal wave energy (*upper middle panel*) reaches $10^{-7} m^2 s/^3$ on the western side of the ridge, but decreases towards the east on the eastern side. This is mirrored in the internal wave energy (*upper right panel*), which is elevated on the western side of the ridge, with relative increases by more than a factor of three (*lower right panel*). The diffusivity is decreased (*lower left panel*) near the bottom on the western side, though, which correlate with increase in buoyancy frequency (*lower middle panel*).

5.2.2 Differences in zonally averaged quantities

Whereas the above section thoroughly describe the interdependence of the lee wave energy, the diffusivity and the buoyancy frequency, Fig. 5.14 and 5.15 only provide images at single latitudes. To keep in line with previous figures and to keep the same sense of overview, I want to show here the variation of the effects of lee waves with depth and latitude, as well. As in section 5.1, I will therefore show zonal averages of the difference in diffusivity and buoyancy stratification. This will provide insight to the overall effect of lee waves in the vertical-meridional plane.

The difference in the zonally averaged diffusivity is shown in Fig. 5.16 (*upper* *panel*). Since the diffusivity above 2000m depth is dominated by large local changes possibly due to a varying eddy or internal wave field, which does not elucidate the point made here, only the depths below 2000m is shown. The first striking aspect is that difference in diffusivity is negative towards the very bottom - meaning that the diffusivity is largest in the control run - where the lee wave energy is largest. Secondly, the magnitude of difference is very large - on the order of $\mathcal{O}(10^{-1})$ - considering values of $\kappa_\rho > 10^{-3}$ are quite uncommon (in the interior at least).

Also in Fig.5.16 is shown the relative difference in (zonally averaged) diffusivity (*lower panel*). The pattern of the relative difference in diffusivity follows relatively closely that of the numerical difference. The large numerical decrease below $4500m$ depth is not rendered as significant, though, but is nonetheless of at least 30% of the diffusivity in the control experiment. As such, the largest difference relative to the control experiment is the large increase from about $3000m$ depth to above $200m$ depth between 55° and $60°N$. Here the difference is more than three times the diffusivity from the control experiment (i.e. an increase of 200%). This increase takes place in the Labrador Sea, which is subjected to strong convection in the winter time. The increase in diffusivity here is (although not shown) due to a decrease in buoyancy frequency over a large area not related to the internal wave field. In the interior the relative differences although more moderate can still be up to ±50%. Between 3000 and $2000m$ depth at $30° - 40°N$, however, there are also significant increases in diffusivity, which could easily be correlated with lee wave activity presented previously. It is however still striking that in the zonally averaged sense the lee wave energy shown in Fig. 5.10 seems to be more correlated with a decrease rather than an increase in zonally averaged diffusivity, although there is no theoretical argument for this.

It is important to keep in mind that the zonally averaged diffusivity can eschew the sense of total diffusion of energy, because the zonal extent is not equal at all depths. In theory, the addition of lee waves should lead an increase in mixing and therefore a more homogeneous ocean represented by a lower buoyancy stratification near the bottom.

In the bottom most $3000m$ the image of this is a bit more unclear though. The difference and relative difference in zonally averaged buoyancy stratification is shown in Fig. 5.17. Near the bottom the numerical difference in (the square of the) buoyancy stratification is between 10^{-8} and 0.5×10^{-7} meaning that the base experiment cause a sharper vertical density gradient. Above this patch of increased stratification is then a layer of decreased stratification, although the magnitude of this decrease is not as large. The aforementioned local changes hypothesized to be caused by a varying eddy or internal wave field can be seen in the *upper panel* near $50°N$ (I have decidedly chosen to leave out change above $2000m$ depth, because they are dominated by these large local differences). In the *lower panel* the relative difference shows that only below $4000m$ depth is the buoyancy frequency significantly altered, as the differences in much of the interior is rendered to a few percentages of that of the control experiment. As such, the numerical increase below $4000m$ depth is translated into somewhere between a 50 and a 100% increase. This is the case from roughly 15 – 50°N.

As mentioned, the increase in diffusivity close to $55°N$ aligns well with a de-

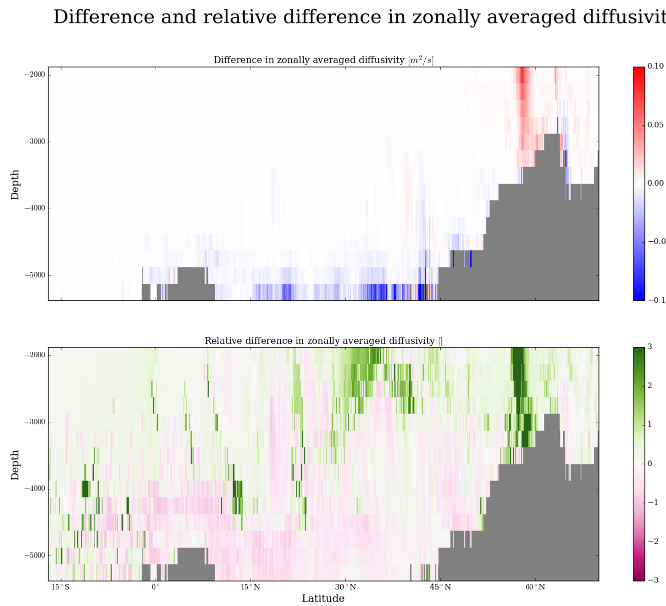

Figure 5.16: The diffusivity is decreased towards the bottom and increased in the northern Atlantic in a tongue between 55° and 60°N extending some 2500m

crease in buoyancy frequency. This deep reaching tongue of decreased buoyancy frequency is not as prominent in the relative difference as in the numerical, since it occurs in a region where buoyancy frequency is in general very low but still visible with a decrease in stratification between 5 and 20% increasing towards the bottom.

In general the differences in diffusivity and stratification are obviously anti-correlated; as given by the Osborne-Cox relation. It was the hypothesis, however, that a large lee wave energy would lead to an increase in diffusivity which in turn would decrease the stratification via mixing. In that sense, there exists a positive feedback between stratification and diffusivity; the lower (higher) the stratification, the easier (more difficult) mixing becomes, which would be evident from a high (low) diffusivity, which would in turn decrease (increase) the stratification even more. As such, it is not always apparent whether a lower stratification, or an increase in mixing would be the first change in this process. On the other hand, there is also a negative feedback involved, since the mechanism responsible for the mixing - the internal waves - feeds of the stratification. This is evident from Eq. 2.34, where the factor $(N^2 - u^2k^2)^{1/2}$ is a quarter-circle with radius $N^2 - f^2$, and thus a larger N^2 implying a larger integral over k. A physical interpretation of this would claim that a higher stratification allows for more energetic internal waves, which in turn are able to provide more mixing leading to a lower stratification. This negative feedback is also mentioned by Trossman et al. (2013) and Melet et al. (2015). In this study it

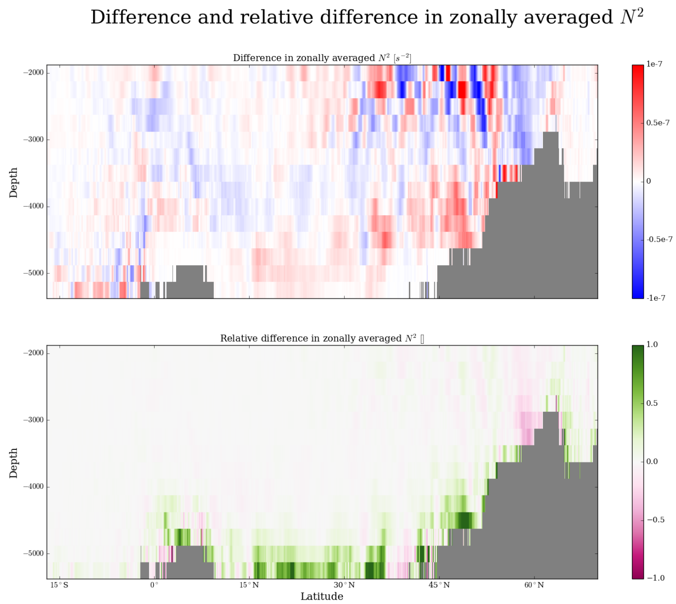

Figure 5.17: The numerical difference in N^2 is larger at intermediate depth, but the relative difference remain largest at the bottom. The decrease in N^2 close to 55° is a a decrease of about 2 – % relative to the control run.

is evident, that both the largest decreases and the largest increases in diffusivity is caused by the increase and decrease in stratification, respectively.

The zonally averaged differences must be taken with some reservation, though, when trying to form a comprehensive picture of the three dimensional effect of the lee waves. They are still zonally averages and, as such, it is important to be aware of the fact that the zonal extent of the model is not equal at all depths because of land/seafloor barriers. A shorter zonal extent - which is not visible in figures of zonal averages - thus makes a larger difference in zonal averaged quantities possible. The zonal averages must therefore be paired with the Fig. 5.1 and Fig. 5.3 of the lee wave bottom flux and stress in order to obtain a more thorough image of the spatial distribution of the lee waves and their effect.

Together, though, the transects shown in Fig. 5.14 and 5.15 and the zonal averages in Fig. 5.17 and 5.16 form a very thorough image of the influence of lee waves on the diffusivity and buoyancy stratification with the current model implementation. In contrast to the background internal wave energy, the lee wave energy is concentrated in certain geographical hotspots in the model; namely the Denmark Strait and the western Atlantic. While the background internal wave energy is largest in the upper part of the ocean, the lee wave energy is concentrated near the bottom - at whatever (varying) depth the bottom is. Although the energy transfer from lee waves to the background internal waves depends on both both fields, it is almost exclusively largest in the bottom model layer, where the lee wave energy field is largest. Nonetheless, the energy transfer at the bottom is able to increase the internal wave energy by up to 5 times and thus the diffusivity throughout the water column. These large increases in internal wave energy does increase the diffusivity, although the largest differences in diffusivity is more closely linked with changes in the buoyancy frequency and take place in regions with already very large diffusivities.

5.2.3 Effects on the mean flow

So far the effect of the lee waves has been focused on diffusivity and stratification. However, the pseudo-momentum flux will also directly affect the transport by removing momentum from the mean flow via the (residual) momentum equation (in addition to the removal of momentum from the mean flow at the bottom via the bottom boundary condition given by Eq. 2.55). This should result in a lower velocities. The difference in bottom velocity between experiment $I075$ and the control run, $\Delta|U|_{z=-H} = |U_{I075}|_{z=-H} - |U_{ctrl}|_{z=-H}$, is plotted in Fig. 5.18, and it is clear that in most regions the bottom velocity is significantly decreased. It should be kept in mind here, that in several regions where the bottom current is originally strong (for instance the Deep Western Boundary Current, but in near coastal regions in general), lee waves are inhibited due to the topographic data. Nevertheless we see a decrease in the bottom velocity on the order of $\mathcal{O}(0.1 m/s)$ in several regions, which naturally coincide with the distribution of the bottom stress. Most noticeable is the large area of decrease in the Western Atlantic, along the North Atlantic Current, and in the overflow regions of the North Atlantic. Particularly interesting is the decrease in velocity in the East Greenland Current when compared with the West Greenland Current, where the bottom speed is increased a little, when taking into account the lack of lee wave generation in the Labrador Sea. This shows that the lee wave are able to remove momentum from and significantly reduce bottom ocean currents with the current model setup. A few regions show an increase in bottom velocity, but this difference almost exclusively occurs in shallow regions and take a characteristic eddy-shape, and it is therefore taken as a result of the varying eddy field.

The difference in velocity between experiment $I075$ and the control run is also plotted along with the pseudo-momentum flux in a transect at 37°N in Fig. 5.19. Between longitudes $75°W$ and $50°W$ there are two vertical sections of a significant decrease and increase in velocity, which seem uncorrelated with the pseudo-momentum flux from the lee waves. Both the increase and decrease in these areas are interpreted as a result of a varying eddy field, but this is an example of the correlation between the velocity and the lee waves not being exactly clear and of the varying eddy field still playing a role in the average quantities over the simulation length. If such large velocity differences can persist, where the pseudo-momentum from lee waves is negligible, to what degree is the velocity difference then attributed to lee waves *in* the regions where lee waves are present? This is impossible to answer, but as mentioned the integration length should ideally be so long as to single out the influences of lee waves over average quantities, although this does not seem to be the case here. At the longitudes and depths, where a significant pseudo-momentum

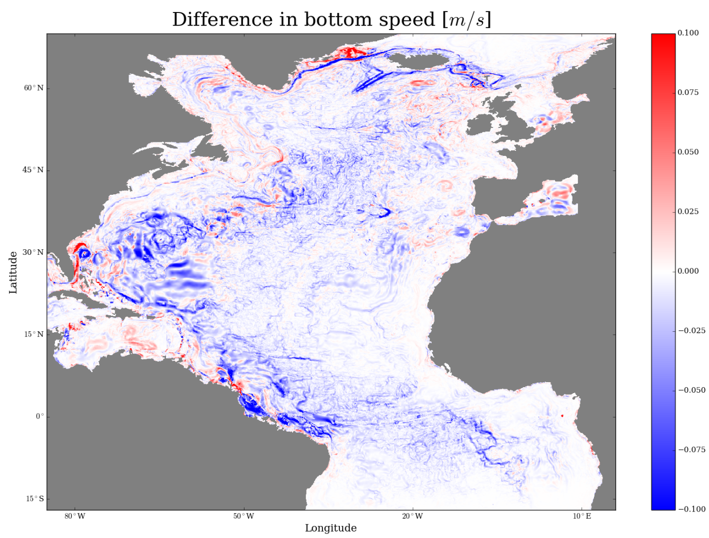

Figure 5.18: The difference in bottom velocity shows a general sink of bottom momentum over the model domain, but especially in the Western and Northern Atlantic.

flux is present, there is however a clear correlation between the pseudo-momentum flux and a decrease in velocity.

The fact that the correlation between velocity differences and pseudo-momentum flux caused by lee waves is clear in some regions, while not clear in others, is also the reason why only depths below $1000m$ is shown in Fig. 5.19. At shallower depths velocities will be higher and fluctuations associated with a varying eddy fields will be more apparent, while the effect of lee waves will be smaller and less clear. This pattern will of course differ from region to region, since the depth of the ocean varies. Velocity differences caused by lee waves are thus difficult to obtain as a function of depth. Nonetheless, the velocity difference $\Delta|U| = |U_{I075}| - |U_{ctrl}|$ is plotted at four different depths, $4000m$ (*bottom right panel*), $3000m$ (*bottom left panel*), $2000m$ (*upper right panel*), and $1000m$ (*upper left panel*), in Fig. 5.20 in order to asses the capacity of lee waves to remove momentum as a function of depth. The varying ocean depth should here be kept in mind. At $4000m$ depth the largest decrease in velocity occurs in the western Atlantic, and interestingly the decrease in this area persist fairly clearly at $3000m$ and even at $2000m$ depth. The region coincide very well with the region of large bottom stress highlighted in Fig. 5.3-5.23. Decreases in other region at $4000m$ depth are also visible at $3000m$ although less clearly, and at $2000m$ and 1000 they are not very apparent. At $1000m$ on the other hand it becomes just possible to see a clear decrease in velocity southwest of Ice-

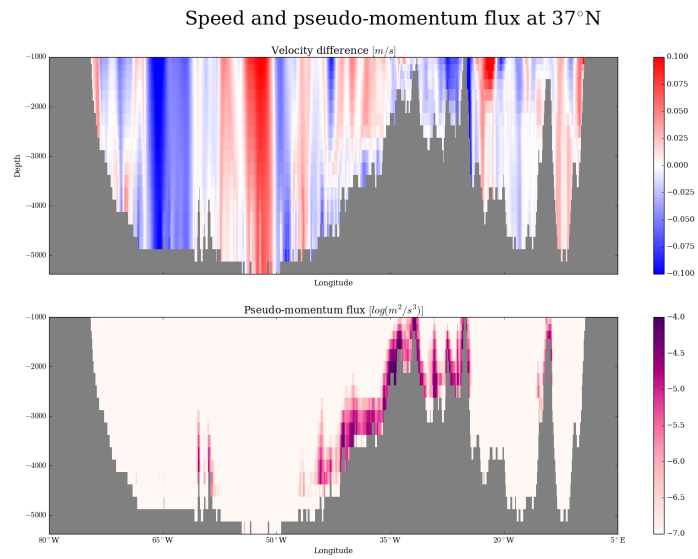

Figure 5.19: The difference in velocity between experiment $I075$ and the control a 37°N is clearly negative where the pseudo-momentum flux is largest over the Mid Atlantic Ridge, showing the effect of lee waves.

land, which also coincide very precisely with an area of large bottom stress in Fig. 5.3.

The direct influence of lee waves on the mean flow field is thus in general fairly clear. A decrease in bottom speed is clearly visible in almost all regions where lee wave generation is permitted by the topography data, and in many regions the decrease is as large as $0.1 m/s$. Considering the magnitudes of the the bottom speed presented in Fig. 5.2 these are very large decreases. Although a few regions where no pseudo-momentum flux is present does show fairly large velocity differences, the correlation between a decrease in velocity and a large bottom stress is very apparent. This is most easily seen in the western Atlantic, where a significant decrease in velocity persists from the bottom to $2000m$ depth and coincides very well with a large bottom stress caused by lee waves. Away from the bottom smaller local fluctuations become more and the effect of lee waves less apparent in most regions.

5.2.4 Intermediate conclusions on the differences between the base experiment and the control run

All in all, the effect of adding a lee wave module are very large on both the mean flow and the background internal wave field. Near the bottom - at whatever depth this is - significant momentum is removed from the mean flow resulting in decreases in bot-

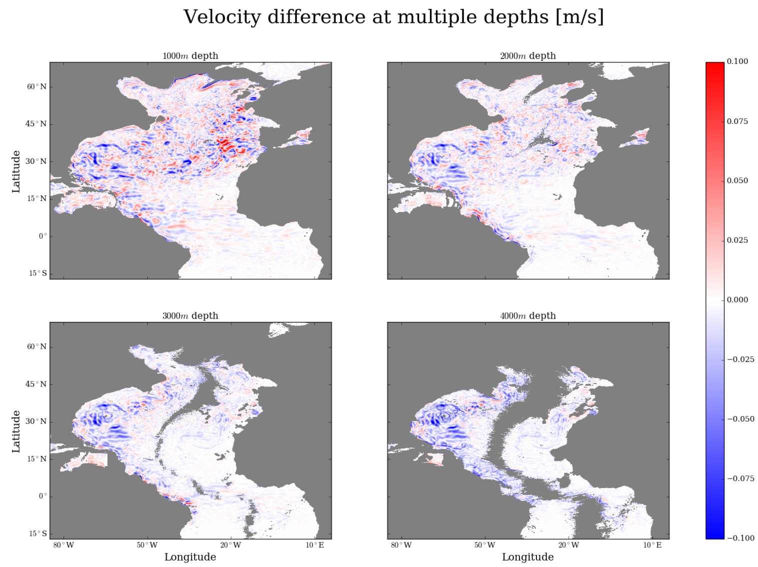

Figure 5.20: Velocity difference $\Delta|U| = |U|_{ctrl} - |U|_{I075}$ at four different depths. *bottom right panel* shows $\Delta|U|_{z=-4000}$. Here the largest decrease is found in the western Atlantic. *Bottom left panel* shows $\Delta|U|_{z=-3000}$, where the decrease in the western Atlantic persist clearly. Decreases found at $4000m$ in other regions does not as clearly persist. *Upper right panel* shows $\Delta|U|_{z=-2000}$, where smaller local fluctuations emerge and the effect of lee waves is less clear. The decrease in the western Atlantic does still persist to some degree, though. *Upper left panel* shows $\Delta|U|_{z=-1000}$, where the effect of lee waves is even more unclear, although a few areas of clear decrease in the central Atlantic. At this depth a clear decrease southwest of Iceland, which coincide with a region of large bottom stress, is also just possible to see.

tom velocities of $0.1 m/s$ in many regions. Furthermore, the internal wave field have been shown to increase by up to 5 times in regions where a large lee wave energy transfer is present. Even though such energy transfer takes place almost exclusively near the bottom, the increase in internal wave energy persists throughout the water column. The effect of this is to increase the diffusivity in the interior - where it can be increased by an order of magnitude - rather than near the bottom, although the largest numerical differences in diffusivity is seen to be more closely correlated with change sin the buoyancy frequency.

5.3 Sensitivity to lee wave parameters

Whereas the previous two sections have focused on the base experiment and the difference between it and the control experiment, the following section will elucidate the difference between the topography sensitivity experiments themselves. In all cases the base experiment, $I075$, has been used as a reference, and as such a difference in a certain quantity between the base experiment and another experiment, *EXP*, are calculated as $\Delta X = XEXP - X_{I075}$, meaning that positive differences (in bottom energy flux, for instance) indicate that the experiment in question shown larger magnitudes of the quantity in question than the base experiment and vice versa.

5.3.1 Sensitivity of the energy flux

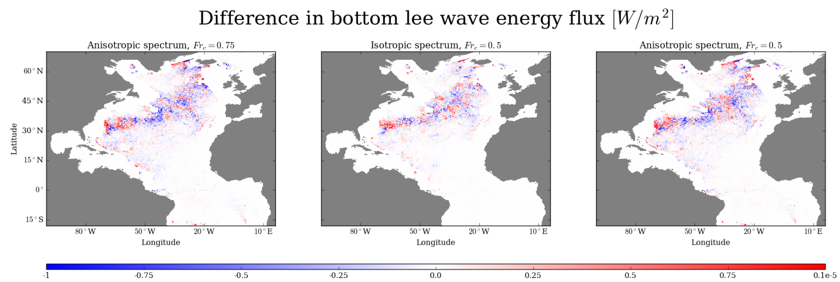

Figure 5.21: The difference in the lee wave energy flux at the bottom is largest along the North Atlantic Current and in the Denmark Strait. The sign of the difference vary locally, however.

The difference in lee wave energy flux at the bottom between the four topography sensitivity experiments is shown in Fig. 5.21. The the energy flux in the base experiment - which is shown in Fig. 5.1 - was used as a reference, and the three images show the difference in energy flux between the base and the other three topography sensitivity experiments; the *left panel* shows the difference with experiment $A075$, *middle panel* with $I05$, and *right panel* with A05. The magnitude of the difference between the runs is locally up to the order $\mathcal{O}(10^{-5})W/m^{-2}$, which amounts to roughly to 10% of the flux, but it seems like the difference is in general more clearly visible when the topography spectrum is changed, rather than when the critical inverse Froude Number is changed. It is not obvious from Fig. 5.21, however, if one parameter setting produces a significantly larger flux than another.

The difference is in all cases largest along the North Atlantic current and in the Denmark Strait (where the flux itself is also largest) but the sign of the difference here varies very locally. In the eastern and tropical Atlantic and in the Southern Atlantic basin the difference is at least an order of magnitude lower. In other words, no region systematically exhibits a neither lower nor higher bottom energy. There is rather a clear geographical correlation between the magnitude of the energy flux in one experiment and the magnitude of the difference between experiments. The fact that the sign of the difference vary locally, while the magnitude of the difference is the same regardless of the sign (for instance along the North Atlantic Current), seems to indicate that using the anisotropic spectrum instead of the isotropic does not produce substantially different results. Rather, the sign of the difference seems locally to be resemble a natural variance which is to be expected.

The bottom energy flux integrates to roughly $0.06TW$ over the model domain in all four topography sensitivity experiments and this total energy flux differ only a few percentages the experiments in between. A globally integrated lee wave energy flux at the bottom between $F_{glob,A075} = 0.0612TW$ and $F_{I05} = 0.0641TW$ shows a significant contribution to the energy cycle of the ocean in all regards. The horizontally integrated energy flux is summarized in table 5.1. Although the differences are only of a few percentages, there is a systematic increase both when using isotropic rather than the anisotropic topography spectrum and when using a critical inverse Froude Number of $Fr_c = 0.5$ rather than $Fr_c = 0.75$. Although small the systematic increase with a lower critical inverse Froude Number is intuitive, since a higher critical inverse Froude Number would act to suppress lee wave generation on a larger amount of the bottom flow. As such the largest difference in total energy flux between all four topography sensitivity experiments is that between experiment $A075$ and experiment $I05$. Between these two experiments there is a difference in total lee wave energy flux of $0.0029TW$, which roughly corresponds to 4.5% of the total energy flux.

To put these differences into perspective, I quickly remind the reader, that the additional two experiments using coarser resolution models - the $1/3°$ eddy-permitting FLAME model of the North Atlantic and the $2°$ coarse resolution global model - both carried out using the isotropic topography spectrum and critical inverse Froude Number $Fr_c = 0.75$ showed a global lee wave energy flux of $F_{glob,1/3°} = 0.0117TW$ and $F_{glob,2°} = 2.93MW$ respectively. Comparing with the results from the topography sensitivity experiments clearly validates that the lee wave energy flux is significantly increased with a finer horizontal resolution most likely to be associated with resolving the eddy field and as a result thereof a stronger bottom flow. In a coarse resolution model a parameterized lee wave energy flux ought thus to be dependent on the eddy kinetic energy.

5.3.2 Sensitivity of the bottom stress

Similar to Fig. 5.21, the difference between the four experiments in bottom lee wave stress is shown in Fig. 5.22, where as previously the *left panel* shows the difference with experiment $A075$, the *middle panel* with $I05$, and the *right panel* with experiment $A05$. It is obvious that changing the topographic spectrum has a much larger influence than changing the critical Froude number. There is hardly any geographical bias, since the bottom lee wave stress increases in basically every region if using the anisotropic topography spectrum rather than the isotropic, and since sign of the difference between the base and experiment $I05$ varies locally. Nonetheless, the western Atlantic and the Denmark Strait are two regions where both the bottom stress, the energy flux and their respective differences the experiments between are among the largest. The bottom stress in these two regions, which are specifically marked out as black boxes in Fig. 5.3, have been examined closer in order to exem-

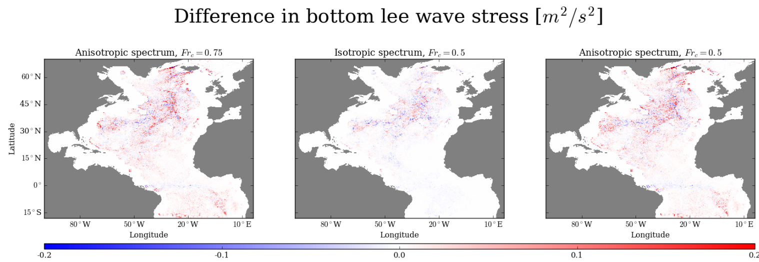

Figure 5.22: The difference in bottom lee wave stress, $F_{diff} = F_{exp} - F_{base}$, between the base lee wave run $F_{base} = F_{I075}$ and the other three experiments is clearly largest when the topographic spectrum is changed rather than the critical Froude number.

plify the differences highlighted in Fig. 5.22.

The square of the magnitude of the bottom stress from experiment $I075$ was used as a reference, $\tau^2_{I075} = \tau^2_{x,I075} + \tau^2_{y,I075}$, and is plotted against the square of the magnitude of the bottom stress from the other three topography sensitivity experiments in Fig. 5.23. As such, the top row shows bottom stresses in the Western Atlantic region and the bottom row shows that in the Denmark Strait region. In all cases τ^2_{I075} is plotted along the x-axis and the square of the magnitude of the bottom stress of the other experiment and region in question is plotted along the y-axis. The *upper and lower left panel* shows bottom stress τ^2_{A075}, the *upper and lower middle panel* shows bottom stress τ^2_{I05}, and the *upper and lower right panel* shows bottom stress τ^2_{A05}. A single dot in the figure thus represent the bottom stresses of a single (bottom) grid point in the two experiments and regions in question. Noticing the different axis values in the upper and lower rows it is first of all clear that the stress are larger in the Denmark Strait than in the western Atlantic. The most important aspect to notice, however, is first of all that the difference in bottom stress brought about by changing the topography spectrum is much larger than that of the Froude Number. This is clear since there is systematically a longer distance from every dot to the diagonal line representing equal stresses in the panels comparing the base experiments with experiments $A075$ and $A05$ than that comparing the base experiment with experiment $I05$. This is the case in both regions. Second of all, it is clear that the bottom stress is increased when changing the topography spectrum. The bottom stress is inherently shifted towards larger values when changing the topography spectrum, whereas the bottom stress is neither increased nor decreased significantly when changing the critical Froude Number. This image is also apparent in both regions.

In the same regions the angle of the bottom stress with the horizontal was also examined. Fig. 5.24 compares the angles obtained in experiment $I075$ with the other three topography sensitivity experiments as a histogram. As in Fig. 5.23 the upper panels contains the angles obtained in the western Atlantic, whereas angles obtained in the Denmark Strait are plotted in the bottom panels.

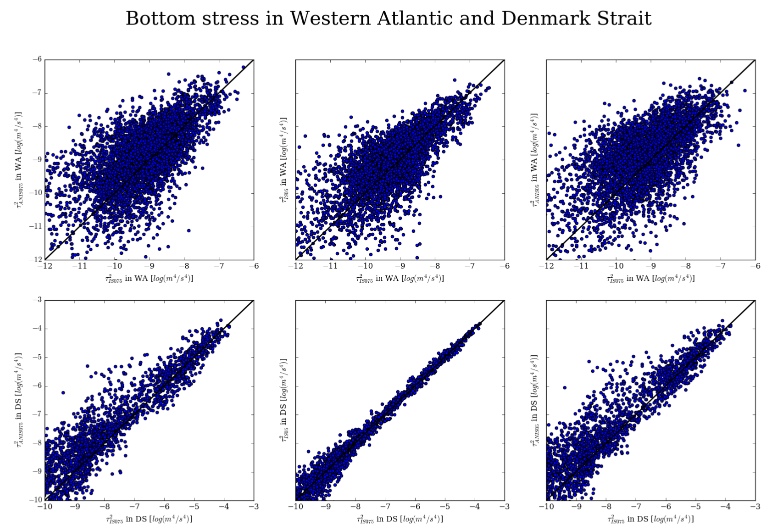

Figure 5.23: Difference in bottom stresses in the four topography sensitivity experiments are shown for two distinct regions; the western Atlantic and the Denmark Strait. Upper panels shows bottom stress in the western Atlantic and bottom panels the Denmark Strait. τ^2_{I075} is plotted along the x-axis in all panels - in the *leftmost panels* against τ^2_{A075}, in the middle panels against τ^2_{I05}, and in the *rightmost panels* against τ^2_{A05}. A single dot represents the (square of) the bottom stress in the respective experiments. Changing the topography spectrum clearly shifts the bottom stress towards larger values, whereas changing the critical Froude Number does not significantly change the bottom stress.

Each panel is a histogram showing the number of bottom grid points on the y-axis with an angle of bottom stress within a certain range as shown by the x-axis. The dark green color of bars indicate the number of grid points within a certain range of bottom stress angle, which both experiments in question had. A light green color above the dark green in a certain angle range indicates that the base experiment had such a number of grid points more than the other experiment in question, whereas a blue color above the dark green indicate that the other experiment in question had such number of grid points more than the base experiment.

In the western Atlantic (*upper panels*) the angle of the stress, θ, is predominantly directed in the half-space $[-\pi, 0]$, i.e. southwards. The stresses of experiments $I075$, $A075$ and $A05$ are directed in a very similar manner, but the differences between experiments $I075$ and $I05$ display a fairly clear rotation of the stress from southward towards the East. The biggest difference in the direction of the stress thus clearly occurs when the critical Froude Number is changed. In the Denmark strait (*lower panels*) the change with the critical Froude Number appears to be minimal, though. The *lower middle panel* containing the stresses from experiments $I075$ and $I05$ are remarkably similar and so are the differences shown in the *lower left* and lower right panels indicating basically no change with the critical Froude Number. There is on the other hand a systematic change in angle with the topography spectrum in the Denmark Strait. In the half-space $[0;\pi]$ angles are switched from northwards to eastwards and in the half-space $[-\pi;0]$ the angles are shifted westward direction, although this change is not as prominent as that in the other half-space. In other words stress angle is shifted towards an even more meridional direction, than was already the case, when using the anisotropic spectrum instead of the isotropic one.

Overall this indicates that a possible systematic change in angle with either topography spectrum or critical Froude Number is very much dependent on the region in question. In the western Atlantic there is no clear systematic change with topography, since the *upper left panel* shows the smallest differences in angle, whereas in the Denmark Strait the shift of the bottom stress is very systematic with topography.

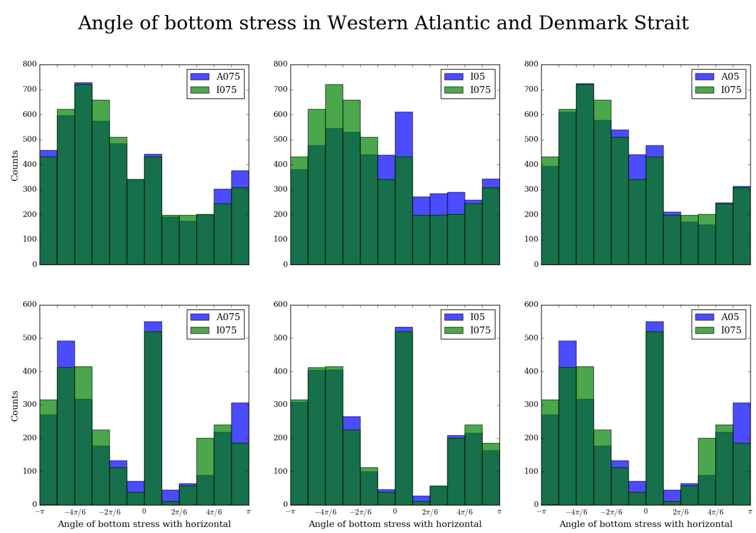

Figure 5.24: Angle of the bottom stress with horizontal for two distinct regions; the western Atlantic and the Denmark Strait. *Upper panels* show the direction of the stress in the western Atlantic. The difference between the respective experiments is largest between experiment $I075$ and $I05$, where there is a clear rotation of the stress towards the East. This rotation is not apparent in any of the other experiments. The *lower panels* show the direction of the stress in the Denmark Strait. Here the change with the critical Froude Number is minimal, but there is a systematic change with the topography spectrum. This is concluded from the very low differences seen in the *lower middle panel* and the large similarities between the *lower left* and *lower right* panels. Overall the change in direction of the bottom stress with either topography or critical Froude Number thus depends on the region examined.

Contrary to the integrated bottom energy flux the magnitude of the bottom lee wave stress differs substantially between the topography sensitivity experiments - up to 40% - when using the anisotropic spectrum rather than the isotropic. This is also the case for both the x- and y-component of the stress. Where the x-component decreases by up to $10^{10} m^4/s^2$ over the model domain - or up to 65% of the base x-stress, the y-component increases (numerically) by $3.5 \cdot 10^{10} m^4 s^2$, resulting in a larger magnitude of the stress caused by the lee waves. This image of a decrease in the x-component of the stress but a larger increase in the y-component of the stress is persistent in the isotropic vs. anisotropic comparisons no matter the critical Froude number. The globally, i.e. vertically and horizontally, integrated pseudo-momentum flux, $T_{glob} = \int_x \int_y \int_z \tau \partial x \partial y \partial z$, has also been computed for the four topography sensitivity experiments and is shown in the two last rows in table 5.1. It is noticeable here that the large differences in the bottom stress are not only diminished in magnitude, they are even of opposite sign when integrating the momentum flux in the vertical with the four experiments varying only in critical Froude number and topography spectrum. Within the four topography sensitivity experiments the maximum of the difference in globally integrated pseudo-momentum flux is thus 4.35% of $T_{glob,I075}$.

The lee wave energy as a function of depth can be seen for all four topography sensitivity experiments in Fig. 5.25. This figure reinforce the zonally averaged image, and it is clear that far most of the lee wave energy is found below 3000m. Notice how the experiments using the anisotropic spectrum seem to have a slightly larger fraction of lee wave energy at depths below 4000m. This would indicate that an even large fraction of the lee wave energy is generated at the very deep ocean in the anisotropic cases, whereas in the isotropic cases a larger fraction would be generated at shallower depths, since the total lee wave flux at the bottom is of similar magnitude. Despite this, the distribution of lee wave energy with depth is remarkably similar across the experiments and reinforce the point already made that the lee wave generation seem insensitive to the topography parameters.

5.3.3 Intermediate conclusions on the topography sensitivity

All in all the lee wave generation seems to shows little sensitivity to changing the topography spectrum and the critical inverse Froude Number. A maximum difference in the total energy flux (integrated over the model domain) of 4.5% between the experiments is not significant considering a natural variance is to be expected, although the sensitivity is systematic with varying both the topography and the critical inverse Froude Number. Regarding the stress exerted by the lee waves on the mean flow, the sensitivity with topography parameters is more complicated. The zonal component of the bottom stress is significantly reduced when using the anisotropic topography spectrum instead of the isotropic, but the meridional component is numerically increased a lot more in order to increase the magnitude of the bottom stress with the anisotropic topography spectrum by up to 38.6% of that of the base experiment . This could point towards the bottom stress being shifted towards the meridional direction, but this has proven to be dependent on the region in question. When also considering the vertical dimension the stress exerted by lee waves

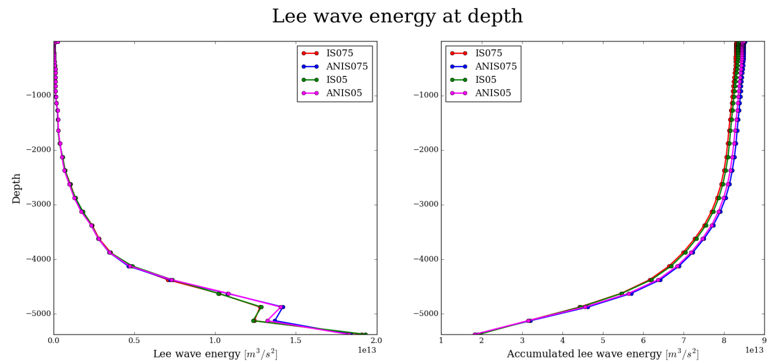

Figure 5.25: Amount of lee wave energy at each depth index (*left panel*) and the cumulative lee wave energy (*right panel*). Most lee wave energy is found in the deep ocean, and only about 10% at depths shallower than 2000m

.

on the mean flow is suddenly not nearly as sensitive to the topography parameters, with the magnitude of the total pseudo-momentum flux (horizontally and vertically integrated) varying only with a maximum 4.35% of that of the base experiment.

5.4 Sensitivity to IDEMIX parameters

Pollmann et al. (2017) evaluated the internal wave energy as simulated by the IDEMIX model and compared it with that estimated from ARGO-float data in order to determine optimal values of the three IDEMIX parameters μ_0, j_{star} and τ_v. In short the parameter values used by Olbers and Eden (2013) led to too little internal wave energy simulated by IDEMIX compared with the ARGO data, and new parameter values were to remedy that. Besides the four topography sensitivity experiment, two additional experiments using the IDEMIX parameter values found in Pollmann et al. (2017) were carried out - one with the isotropic spectrum and one with the anisotropic spectrum, and both with $Fr_c = 0.75$ - were also conducted. The purpose of these two additional experiments was to investigate the sensitivity of the lee wave field to the IDEMIX parameters, and to estimate whether the internal wave energy was in accordance with the ARGO data.

The vertically integrated lee wave energy for these two experiments along with that of the base lee wave experiment is shown in Fig. 5.26

Despite the fact that the energy flux at the bottom is not changed much with the new IDEMIX parameters - this is shown in table 5.1 with a decrease of 1.90% and 3.15% for the isotropic and anisotropic spectrum respectively - the vertically integrated lee wave energy is in many regions an order of magnitude larger. This image is similar in the vertically integrated background internal wave energy shown in Fig. 5.27, which is in correspondance with the findings of Pollmann et al. (2017).

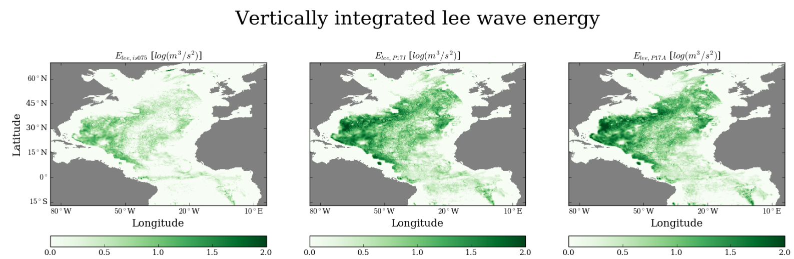

Figure 5.26: The *left panel* shows the vertically integrated lee wave energy in the base experiment ($I075$, isotropic spectrum and $Fr_c = 0.75$). The *middle panel* shows the same for experiment with $P17$ IDEMIX parameter values and isotropic spectrum ($P17I$) and the *right panel* shows it with the $P17$ IDEMIX parameter values and the anisotropic spectrum ($P17A$). The lee wave energy is larger throughout the entire model domain using the parameters values of Pollmann et al. (2017)

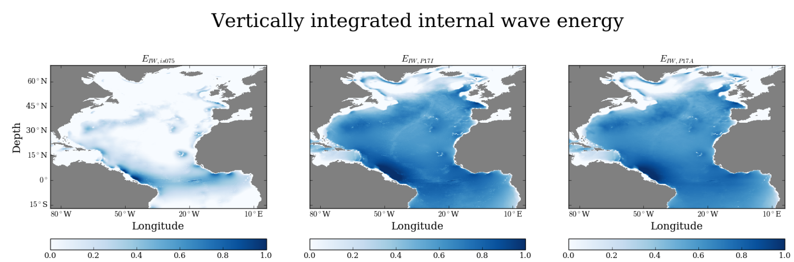

Figure 5.27: The *left panel* shows the vertically integrated internal wave energy in the base experiment ($I075$, isotropic spectrum and $Fr_c = 0.75$). The *middle panel* shows the same for experiment with the $P17$ IDEMIX parameter values and isotropic spectrum, $P17I$ and the *right panel* shows it with the $P17$ IDEMIX parameter values and the anisotropic spectrum, $P17A$

The horizontally integrated lee wave energy and the energy transfer to the internal wave compartment and to/from the mean flow is shown as a function of depth for all experiments in Fig. 5.28. First of all it is very clear that changing the IDEMIX parameters significantly increases the lee wave energy at most depths. This does not, however, increase the energy transfer to the background internal wave field, since this transfer is directly affected by the α- and therefore the IDEMIX parameters. As compared to the lee wave energy this energy transfer is shifted vertically, which can be an effect of both the α-parameter and the background internal wave energy. The energy exchange with the mean flow is much smaller than the transfer to the internal wave field at most depths, but above $1000m$ depth an energy transfer to the mean flow is also significant. Taking the vertically integrated transfer shown in

Fig. 5.13 into account, this is most certainly due to the energy transfer taking place in the Denmark Strait. Furthermore, Fig. 5.28, clearly shows that the lee wave energy and the energy transfers are much more affected by changing the IDEMIX parameters rather than both the topography spectrum and the critical Froude number. At all depths where the largest differences between the experiments are found, the largest differences are found between those with the IDEMIX parameters from Pollmann et al. (2017) and the topography sensitivity experiments rather than between experiments differing in topography spectrum. In the bottom most four model layers the energy transfer is reduced by roughly $20-30\%$ when using the new IDEMIX parameters as compared to the original ones, wheres the lee wave energy itself is roughly tripled. In this figure it is important to remember that energy is not transferred at all depths in all regions. The bottom flux does not occur at equal depths, and the horizontal distribution of lee wave energy as shown in Fig. 5.26 should be taken into account, when forming an image of the distribution of lee wave energy. Furthermore, it might be tempting to view the energy transfer as a result of the lee wave energy itself, but the reverse image is perhaps more elucidating. Rather than considering a large energy transfer a result of a large amount of energy present, the large amount of lee wave energy should be considered the consequence of a small energy transfer. This explains the differences in lee wave energy and energy transfer between the four topography sensitivity experiments and those with the Pollmann et al. (2017) IDEMIX parameters; the energy transfer to the background internal wave compartment is lower below $4000m$ depth, and precisely because of this is the lee wave energy larger.

As was done with the four topography sensitivity experiments, the lee wave energy and diffusivity was examined in a transect at $37°N$ using the new IDEMIX parameters. The lee wave energy at $37°N$ is shown in Fig. 5.29, where the upper panel contains the lee wave energy of the base experiment, *I075*, the middle is the lee wave energy of experiment $P17I$ and the lower panel is that of experiment $P17A$. Clearly both experiments using the new IDEMIX parameters show a more energetic lee wave field, and the difference between the two is not large. There might be a slightly lower decay with above the bottom in experiments $P17I$ and $P17A$, but the horizontal distribution is very similar throughout all three experiments. In general the lee wave energy is simply higher at all depths in experiments $P17I$ and $P17A$.

A central part of the implementation of lee waves in an ocean circulation model, would be the effect lee waves cause on diapycnal diffusivity. As the differences in both lee wave energy flux and energy transfer to the internal wave domain have been very small across the four topography sensitivity experiments, the diffusivity at a certain latitude has not been shown for all these four experiments. Since, however, the lee wave field changes significantly with the IDEMIX parameters, the differences in diffusivity between experiments using the original IDEMIX parameters, the parameters of Pollmann et al. (2017) and the diffusivity from the control run without lee waves is warranted. Fig. 5.30 shows the diffusivity at $37°N$ from base experiment $I075$ (*upper left*), $P17I$ (*upper right*), $P17A$ (*lower left*), and from the control run without lee waves (*lower right*). In the case of no lee waves the diffusivity is at many longitudes near the bottom between $0.1m^2/s$ and $0.01m^2/s$. This magnitude is replicated quite similarly in all the three experiments with lee waves, which corre-

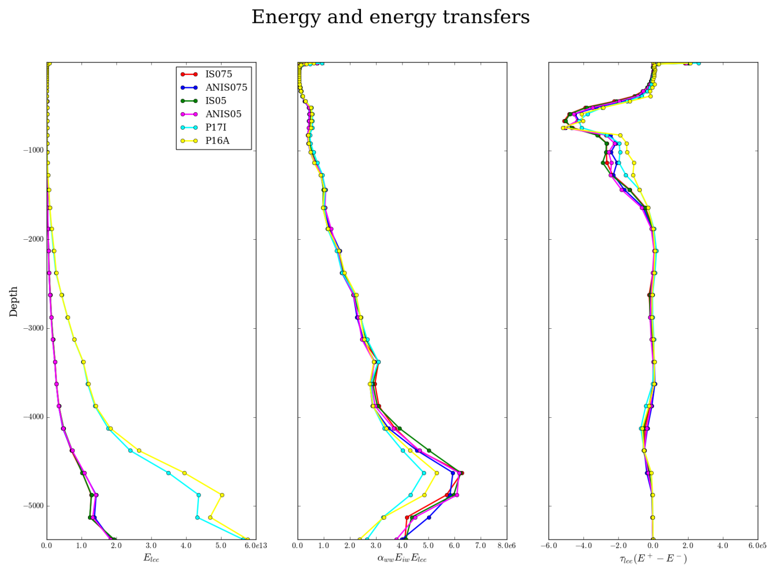

Figure 5.28: The lee wave energy (*left panel*) is much larger in the experiments P17I and P17A than in the rest of the experiments. This does not result in a larger energy transfer to the background internal wave domain (*middle panel*), however. This is due to the α-parameter being directly affected by the new IDEMIX parameters. In general the energy transfer to the internal wave domain is shifted vertically as compared to the lee wave energy. The energy transfer to the mean flow (*right panel*) is very similar in allexperiments, and below $2000m$ depth much smaller than that to the internal wave compartment. At roughly 700 to $500m$ depth the two energy transfer are of equal magnitude (integrated over the model domain)

sponds well with Fig. 5.14. Here it was shown that the diffusivity difference between the control run and the base experiment $\kappa_{I075} - \kappa_{ctrl}$ could be as large as $0.1m^2/s$ but of either sign near the bottom. In Fig. 5.30 it is clearly shown that the diffusivity is in all cases of similar magnitude near the bottom. It is, however, also clear that the diffusivity away from the bottom is often a factor of 10 larger in experiments $I075$, $P17I$ and $P17A$ than in the control run (similar result were found for the three experiments $A075$, $I05$, $A05$ although not shown here). In all panels there are several areas above roughly $1500m$ depth where the diffusivity is somewhat irregular. These patches seem unrelated to the lee wave energy and are present in all cases, why they are could be a result of meridional transfer diffusivity by the background internal gravity wave field.

The increase in diffusivity is even slightly more apparent in experiment $I075$ than in experiments $P17I$ and $P17A$, indicating that the IDEMIX parameters of Pollmann et al. (2017) will cause the lee wave field to provide slightly less energy for

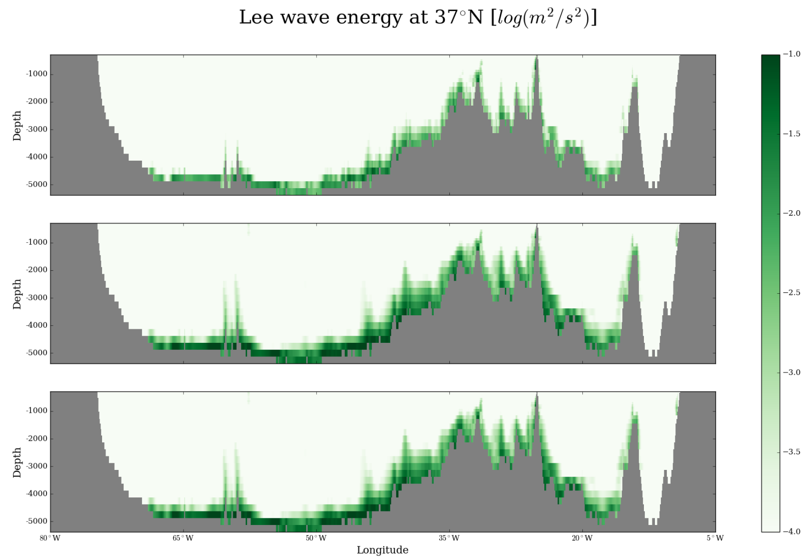

Figure 5.29: The *upper panel* lee wave energy at 37°N in the base experiment ($I075$, isotropic spectrum and $Fr_c = 0.75$). The *middle panel* shows the same for experiment with $P17$ IDEMIX parameter values and isotropic spectrum, $P17I$ and the *lower panel* shows it with the $P17$ IDEMIX parameter values and the anisotropic spectrum, $P17A$

mixing. This effect is also apparent from Fig. 5.13, where the transfer to the internal wave compartment is visibly lower below $4000m$ depth for the experiments $P17I$ and $P17A$. As mentioned before, this is due to the α-parameter being decreased. An increase in diffusivity in the interior ocean as an effect of the addition of lee waves is, nonetheless, not a straightforward result, but it reinforces the image - which was shown in Fig. 5.14 and Fig. 5.15 - that even though the energy transfer to the internal wave compartment is by far largest near the bottom, the internal wave energy - and therefore also the diffusivity - is increased throughout water column. The emphasis should here as much be put on the vertical propagation of internal wave energy as on the energy transfer from lee waves.

The new IDEMIX parameters of Pollmann et al. (2017) does thus have an influence on the lee wave energy, although the influence is not as clear as on the background internal wave energy. The increase in the lee wave energy can be explained via the balance between the energy flux at the bottom and the transfer of lee wave energy to the internal wave compartment, from which the energy can be made available for mixing. Since the energy flux at the bottom largely remain the same - integrated over the entire model domain it is decreased by a few percentages when using the IDEMIX parameters from Pollmann et al. (2017) - the total energy transfer away

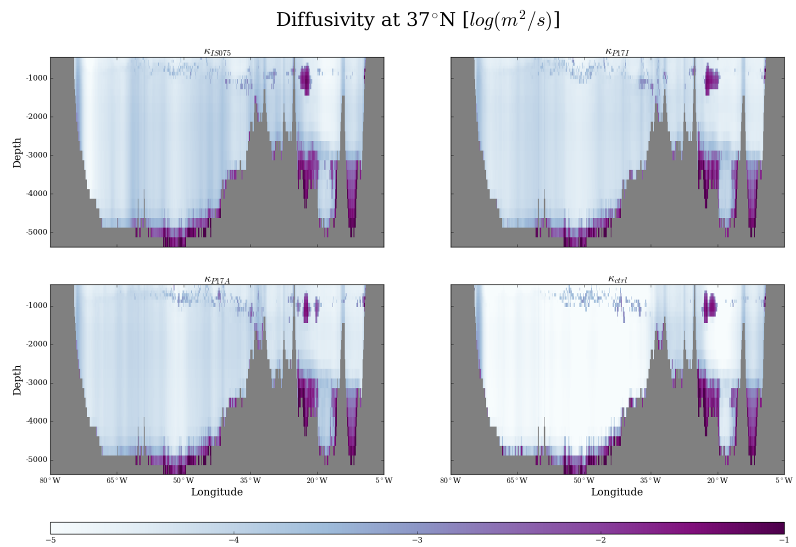

Figure 5.30: The diffusivity at 37° N in the three experiments $I075$ (*upper left*, $P17I$ (*upper right*, $P17A$ (*lower left*, and in the control run without lee waves (*lower right*). In all cases the diffusivity is of similar magnitude near the bottom, but away from the bottom it is in general a factor of 10 (or more) larger in the three experiments with lee waves.

from the lee wave compartment will remain similar as well. This energy transfer is dominated by that to the internal wave compartment, which is determined by the product $\alpha_{ww} E_{GM} E_{lee}$ in Eq. 2.46, where $\alpha_{ww} = \mu_0 |f_e| / c_{star}^2$. With the new IDEMIX parameters, α_{ww} is decreased by a factor of 8, and to keep the dissipation at the same level the energy of the background internal wave field and the energy contained in the lee wave field will thus increase. Since the bottom energy flux does not change much in between the different experiments, it is most illuminating to consider the differences in the vertically integrated lee wave energy as a result of a change in the energy transfer away from the lee wave compartment, rather than the transfer being the result of the lee wave energy. Additionally because of the decrease in energy transfer to the internal wave compartment, the diffusivity in the interior is also lower in experiments $P17I$ and $P17A$ than in the four topography sensitivity experiments, although it is still highar than in the control run. All in all, a changing of the IDEMIX parameters seems to have a larger influence on both the lee wave energy, energy transfer and diffusivity, than the differences arising due to using different topography spectrum or critical Froude Number.

The difference in bottom stress using the new IDEMIX parameters exhibits the same pattern as the other experiments; using the anisotropic topography spectrum decreases the zonal component of the bottom stress, but increases the meridional component much more resulting in a large increase in the magnitude of the bottom stress relative to the isotropic spectrum. Despite the fact that the bottom stress exhibits differences relatively similar to those found with the original parameters, the (horizontally and vertically) integrated pseudo-momentum flux is increased with respectively 27.9% (isotropic spectrum) and 19.3% (anisotropic spectrum) with the new IDEMIX parameters. This is a significant increase. The vertically integrated pseudo-momentum flux is shown in Fig. 5.31. As with the lee wave energy the pseudo-momentum flux is also generally increased over the entire domain. Especially in the western and central Atlantic is the pseudo-momentum flux increased, while there might be a slight decrease in the northern Atlantic.

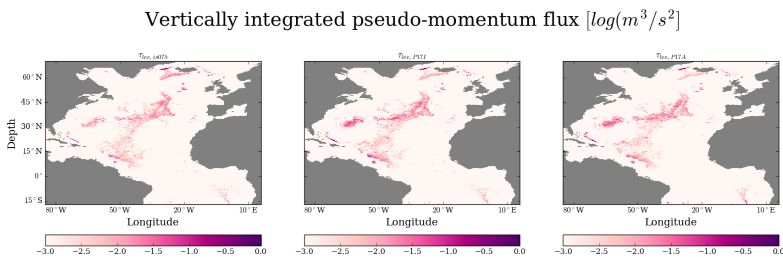

Figure 5.31: The *left panel* shows the vertically integrated pseudo-momentum flux using the original IDEMIX parameters, isotropic topography spectrum and Fr_c = 0.75. The *middle panel* shows the same for experiment with $P17$ IDEMIX parameter values and isotropic spectrum ($P17I$) and the *right panel* shows it with the $P17$ IDEMIX parameter values and the anisotropic spectrum ($P17A$)

.

Changing the IDEMIX parameters thus have a significant effect on the lee wave field. The vertically integrated lee wave energy is in many regions increased by an order of magnitude compared to the base experiment, and in general the lee wave energy is at all depths below 4000m between three and four times as large in experiments $P17I$ and $P17A$ than in the base experiments. This increase in energy is not despite providing less energy per time for mixing, but because the energy per time provided for mixing is decreased. A decreased energy transfer also result in a lower diffusivity in experiments $P17I$ and $P17A$ than in the base experiment, although it is still higher than in the control run. The more energetic lee wave field does, however, remove more momentum from the mean flow. These changes are significantly larger than the changes brought about from simply changing the topography spectrum or the critical Froude Number, although the general pattern of the differences in bottom stress is similar to those caused by changing the topography spectrum and critical Froude Number. An overview of this is also recorded in table 5.1.

5.5 Comparison with ARGO-derived data

Ideally the results of the global model simulation should be held up against solid data from observations. It should in general be the aim for all modellers to hold their results agains observational data, in order to test the validity of the theoretical assumptions and the technical implementation. If model data is not tested against real world observations, a modeller runs the risk of only being able to show the consequences of his or her assumptions, and not whether the assumptions themselves were realistic in the first place. If not careful this can ultimately lead to the trap of validating ones assumptions via the assumptions themselves. A model can be constructed in a number of ways, more or less complex and sophisticated, but the aim is and should always be to learn something new about the real world and not only about the model itself, which is why model results should be tested against observational data.

In the real world observations of lee waves are very sparse, however. Several studies have carried out observations of near bottom diffusivity (notably the DIMES project in the Southern Ocean) and have called out lee waves as the prime driver of this diffusivity, because of the conditions in the Southern Ocean being particularly favourable for the generation of lee waves in this region. Despite a qualitatively reasonable argument for lee wave driven mixing, observation do also show a discrepancy between observed and predicted diffusivity (Waterman et al., 2013). But these are only observations of the consequences of lee wave breaking or indirect or inferred observations.

Two obvious difficulties in obtaining credible estimates of lee wave driven mixing are the intermittency of the waves and the process of separating them from other internal waves. In our model we assume the spectral shape to stay close to that at the generation site (which is given by the Bell flux) throughout the water column. This is an assumption which might or might not hold true, but no observational evidence exists (to the author's knowledge) to directly discredit this assumption.

The ARGO program currently deploys close to 4000 floats around the world capturing salinity, temperature and pressure as a function of depth, from which density profiles can be calculated. From a Fourier transform of the strain, a measure of the degree to which wave motions can distort isopycnals, the strain is expressed in terms of vertical wavenumber and frequency. Using the polarization vector the energy as a function of depth, vertical wavenumber and frequency (what is referred to as the energy spectrum) can be expressed in terms of the strain spectrum. By factorizing the energy spectrum into a depth dependent, vertical wavenumber dependent and a frequency dependent part, and thereafter integrating over each domain, the internal wave energy can be estimated from strain variance recorded by the CTD measurements from the Argo floats. This method captures the effect of all wave-like motions on density and thus make an ideal way to compare model results to real world observations of internal wave energy. The difficulty of how to separate density variations caused by one type of wave rather than another, say lee waves and internal tides for instance, still persists, though. The current model formulation assumes the lee wave energy spectrum throughout the water column to be given by the Bell formula, that is a spectral shape as that of the energy flux at the bottom, which is again dependent on the bottom topography spectrum. In other words the spectral shape of the lee waves is different from that other internal waves. The spectral shape of the GM-model, as modified by Cairns and Williams (1976), is defined by two shape functions determining the dependence on frequency and vertical wavenumber, respectively. The scaling of the two shape functions depends on the so-called spectral slope, which can be filtered in the ARGO data.

If the topography spectrum is assumed isotropic the lee wave shape function gets a (horizontal) wavenumber dependence

$$A(k,\phi) \sim \frac{k^2 U_n^2}{k^2 U_n^2 - f^2 + r^2} k^{-2\nu-1} \tag{5.1}$$

where the dependence on ϕ enters via U_n. Given the relation between vertical and horizontal wavenumber $m_{lee} = k(N^2 - k^2 U_n^2)^{1/2}(k^2 U_n^2 - f^2)^{-1/2}$, this does not translate into a single power dependence on vertical wavenumber. As such, the spectral slope of the GM-model is not present in the shape functions of lee waves, which make the comparison of ARGO data to the model output difficult. Another difficulty in comparing the ARGO data of internal wave energy with the modelled lee wave energy is the depth at which the ARGO floats measure strain and shear spectra. Pollmann (2020) estimates internal wave energy from ARGO floats over the entire world ocean averaged in depth intervals. The map of internal wave energy provided by the ARGO data covers a much larger area in the depth range $300-500m$, than in the range $1000-2000m$. The best covered regions are the Pacific and Indian Oceans. In this study we have focused mostly on the Atlantic and the Southern Ocean, since this is where the lee wave generation is strongest, but these are unfortunately not covered as well by the ARGO data. In section 5 I also highlight especially the Denmark Strait as an area of high lee wave activity, and this is also a region where the lee wave generation takes place at a fairly shallow depth.

The average lee wave energy, as simulated in the base experiment $I075$, is plotted for four different depth bins in Fig. 5.32. The depth bins have been chosen so to better compared the energy levels with that derived from the ARGO data as shown in Pollmann (2020). The *upper left panel* in Fig. 5.32 shows the average lee wave energy between 2000 and $300m$ depth which is considered to be the full depth range of the ARGO floats. The remaining three images show lee wave energy in the depth ranges $2000-1000m$ (*upper right panel*), $1000-500m$ (*lower left panel*), and $500-300m$ (*lower right panel*). In the full depth range the energy is largest in the Denmark Strait, north Atlantic and midlatitude central Atlantic. It is apparent from the differences between the *upper right* and *lower left* panels that the energy in most of the north and central Atlantic is below $1000m$ depth. Some of the energy in the north Atlantic is still visible between 1000 and $500m$ depth, but almost all the energy in the central Atlantic is only present below $1000m$ depth. The lee wave energy present in the Denmark Strait emerges somewhere between 2000 and $1000m$ depth but is only fully visible above $500m$ depth, although the average magnitude in this region does not really change in the different depth ranges. The energy levels derived from ARGO data in Pollmann (2020) does not allow for much comparison below $1000m$, because the ARGO data does not fully cover all regions (the coverage is better at shallower depths; especially above $1000m$ depth), but in the depth range $1000-500m$ some comparison is possible although mostly in the central Atlantic. Lee wave energy simulated in this region in this study is extremely localized, however.

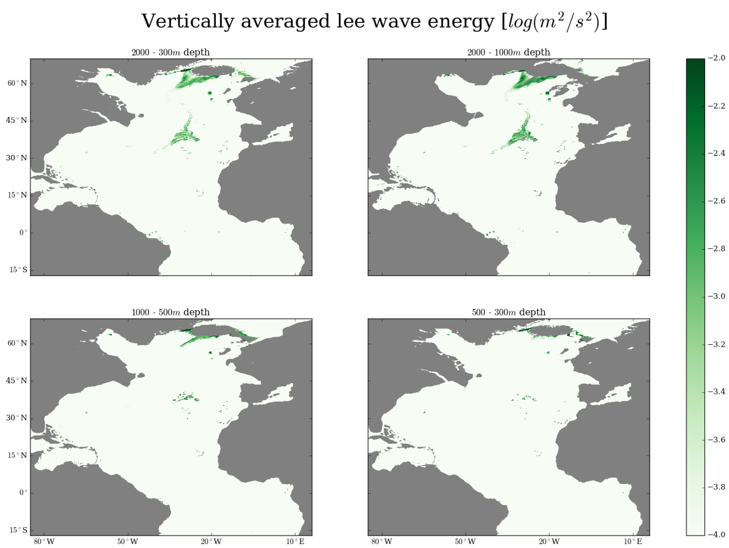

Figure 5.32: Lee wave energy has been vertically averaged in four different depth ranges in order to compare with ARGO data from Pollmann (2020). Lee wave energy in the midlatitude central Atlantic is present between 2000 and $1000m$ depth (*upper left panel*), where the majority of energy in the northern Atlantic is also present. In the Denmark Strait the lee wave energy emerges above $1000m$ (*lower left panel*) but is only fulle visible above $500m$ depth (*lower left panel*). The average lee wave energy in the between 2000 and $300m$ depth is shown in the *upper left panel*, where lee wave energy in midlatitude and northern Atlantic and in the Denmark Strait is largest. The energy levels at these depths are not easily comapred with those found by Pollmann (2020), since internal wave energy derived from ARGO data does not fully cover all these regions at the depths in questions. In the particular regions and depths where comparison is possible, energy levels here do not contradict those derived from ARGO data.

The energy levels derived from ARGO data in mid-latitude and northern Atlantic is mostly available between 1000 and $500m$ depth but especially above $500m$ in Pollmann (2020) and are on the order of magnitude $\mathcal{O}(10^{-3})\,m^2/s^2$, which is not in contradiction, with that shown in Fig. 5.32, where lee wave energy is (in most regions) at least an order of magnitude lower. These are however energy levels found in experiment $I075$, which are considerably lower than those found in experiments $P17I$ and $P17A$. Furthermore, Fig. 5.32 only shows lee wave energy, but a more accurate and fair comparison would also include the background internal wave energy, since the estimates made in Pollmann (2020) does not separate lee wave energy from internal wave energy. Hence, the vertically averaged total internal wave energy (i.e. lee wave plus background internal wave energy) in the same depth bins is shown in Fig. 5.33 for experiment $P17I$. The *upper left panel* shows the vertically averaged energy between 2000 and 300m depth. Here it is noticeable that the mid-latitude and northern central Atlantic stand out, why it is obvious that the large amount of lee wave energy in these regions provide a significant share of the total wave energy. In the *upper right panel* showing the wave energy between 2000 and 1000m depth, these regions are even more prominent, which corresponds well with the image provided by Fig. 5.32. Above 1000m depth these two regions are not nearly as prominent. Here the addition of lee wave energy is mostly seen in the Denmark Strait. Although not clearly corresponding with the results of Pollmann (2020) the current model results does not strictly contradict them either. The vertically averaged energy levels larger than $10^{-2} m^2/s^2$ between 1000 and 2000m depths shown in Fig. 5.33 are not reflected in the ARGO data, but as mentioned before the ARGO data does not fully cover the regions in which these energy level are found in the current model simulation.

Although not shown here, a similar plot was made using lee wave and internal wave energy from experiment $I075$, where the energy levels in most of the model domain was found to be between a half and an entire order of magnitude lower. The energy levels were not significantly different in the mid-latitude central and northern Atlantic, however, making the regions in which lee wave energy is high even more prominent. This reinforces the image of the lee wave energy as a function of depth shown Fig. 5.13 showing that the lee wave energy is particularly increased below 3000m depth in experiment $P17I$ and $P17A$ as compared to experiment $I075$ and not as much above 2000m depth (although this is an integral over the entire model domain not focusing on particular regions). Since (a large portion of) the lee wave energy is transferred to the background internal wave compartment below 3000m depth, the prominence of lee wave energy will wane at shallower depths, where the prominence of internal wave energy will increase. When comparing with ARGO derived internal wave energy, of which coverage is significantly worsened below 1000m depth, this means that even though energy levels might seem somewhat high in experiment $P17I$ (and $P17A$), they are closer to the ARGO derived data than that of experiment $I075$.

5.6 Overview of and conclusions on the parameter sensitivity analysis

Averaged over a simulation of one year the implementation of a lee wave module in the internal wave model IDEMIX coupled to an eddy resolving regional model of the North Atlantic has shown a horizontally integrated bottom energy flux over the model domain between $F_{glob,I075} = 0.0641 TW$ and $F_{glob,A075} = 0.0612 TW$, a magnitude of the bottom stress between $\tau_{glob,I05} = 0.596 \cdot 10^{12} m^4/s^2$ and $\tau_{glob,A075} =$

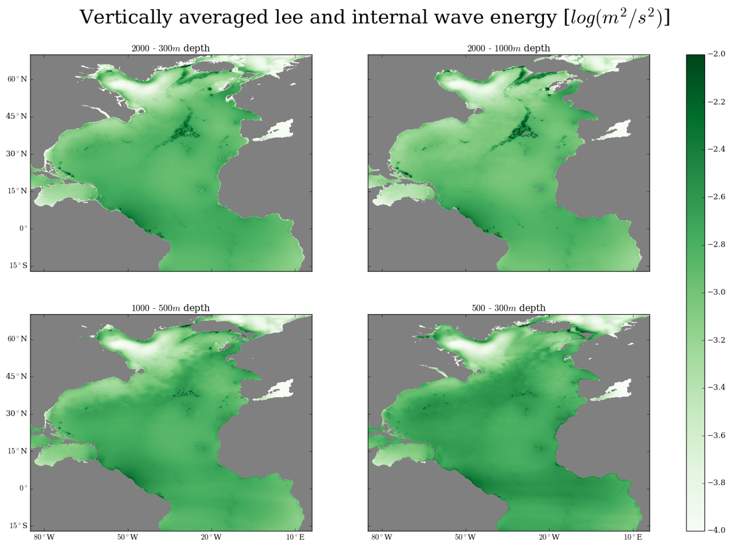

Figure 5.33: The vertically averaged internal and lee wave energy in four depth bins shows the prominence of lee wave generation in the central midlatitude and northern Atlantic in both the full depth range $2000-300m$ (*upper left panel*) but espeically in between 2000 and $1000m$ depth (*upper right panel*). Above $1000m$ the prominence of these two regions subsides. In the *lower left panel* showing average energy levels at $1000-500m$ the prominence of the Denmark Strait is more visible, and above $500m$ depth (*lower right panel*) this region is fully visible, but not as prominent. Values of between $10^{-3}m^2/s^2$ and $10^{-2}m^2/s^2$ at depths at $1000-300m$ reflects well those of the ARGO derived data. Below $1000m$ depth the coverage of the ARGO data is substantially lowered making a comparison more difficult.

$0.859 \cdot 10^{12} m^4/s^2$, and a vertically integrated pseudo-momentum flux between $T_{glob,A075} = 5.15 \cdot 10^{13} m^5/s^2$ and $T_{glob,I05} = 5.55 \cdot 10^{13} m^5/s^2$ in the four topography sensitivity experiments using the IDEMIX parameter values from Olbers and Eden (2013). These four different experiments were carried out differing by the isotropic vs. anisotropic topography spectrum and the critical inverse Froude Number $Fr_c = 0.75$ or $Fr_c = 0.5$. The so-called base experiment - using the isotropic spectrum and the critical inverse Froude Number $Fr = 0.75$, showed neither the lowest nor the highest bottom energy flux or stress, and while the total energy flux changed by a maximum of -2.57% of that of the base experiment between the four topography sensitivity experiments, the bottom stress changed by a maximum 41.4%. By far the largest differences in bottom stress comes about from using the anisotropic topography spectrum rather than the isotropic; the effect of changing the critical inverse Froude Number remains small. The differences in the bottom stress are seen in both the zonal and the meridional component; whereas the zonal component is decreased when using the anisotropic spectrum, the meridional is largely increased. While the bottom stress differs substantially in these four topography sensitivity experiments, by and large due to the anisotropic topography spectrum, the vertically integrated pseudo-momentum remains quite similar throughout them only differing a maximum of -4.45% Details of this is summarized in table 5.1. Despite changes in both the zonal and meridional component of the bottom stress, a clear systematic change of the angle of the bottom stress with either the topography spectrum or the critical inverse Froude Number has not been detected. This rather depends on the specific geographical location.

The spatial distribution shows a large energy flux and stress along the North Atlantic Current, in the northern Atlantic and the Denmark Strait. The pseudo-momentum flux is generally deposited 500 – 1000m upwards from the bottom, and is zonally averaged largest just below 4000m, although there is a substantial amount between 500 and 1500m depth close to and north of 60°N. This spatial distribution of both energy and pseudo-momentum flux remains similar in all four topography sensitivity experiments.

Since the differences in bottom energy flux and stress were by far largest when altering the topography spectrum rather than the critical inverse Froude Number, two additional experiments dubbed *P17I* and *P17A* using the IDEMIX parameters found by Pollmann et al. (2017) were only carried out using a critical inverse Froude Number of $Fr_c = 0.75$. Changing the IDEMIX parameters reduces the lee wave energy flux, but only a small amount. Experiment $P17I$ and $P17A$ showed a total bottom energy flux of 0.0616 and $0.0608TW$, respectively, and therefore the largest difference between all the experiments is $0.0033TW$, which amounts to 5.14% of the largest bottom energy flux. The tendency in these two additional experiments were similar as the four topography sensitivity experiments; the difference in bottom energy flux did not change much, but the magnitude of the bottom stress increased by 38.6% when using the anisotropic topography spectrum (i.e. in experiment $P17A$). The vertically integrated pseudo-momentum flux were increased by respectively 27.9 and 19.3% relative to the base experiment, and is as such much more sensitive to changes in the IDEMIX parameters than to the topography parameters. Also the vertically integrated lee wave and background internal wave energy is much sensitive to changes in IDEMIX parameters, than it is to altering the topography spectrum or the critical inverse Froude Number. The pseudo-momentum flux increases, because it is directly dependent on the lee wave energy (or rather on the difference in upward and downwards propagating lee wave energy), and not on the energy flux at the bottom. Even though the bottom energy flux remain similar the lee wave energy itself is increased in experiments $P17I$ and $P17A$.

Energy transfer to the background internal wave field has proven to be the main route, through which the lee wave field loses its energy, as it is often an order of magnitude larger than the energy transfer to the mean flow. IDEMIX calculates diffusivity based on the internal wave energy, and the lee wave module is implemented as an energy compartment itself linked with the background internal wave energy via a energy transfer given by $\alpha E_{iw}E_{lee}$., where the transfer coefficient, α, is dependent on the IDEMIX parameters μ_0, $s_\star$, and τ_v. The change in diffusivity due to the

Bottom lee wave energy flux and stress									
Quantities \ Experiments	$I075$	$A075$	$I05$	$A05$	$P17I$	$P17A$	$1/3°$	$2°$	$1/10°$
F_{glob} $[TW]$	0.0628	0.0612	0.0641	0.0621	0.0616	0.0608	0.0117	0.0114	0.262
Change in relation to base flux	-	−2.57%	2.10%	−1.15%	−1.90%	−3.15%	–	–	–
$\tau_{x,glob}$ $[10^{10} m^4/s^2]$	−1.57	−0.54	−1.58	−1.25	−1.55	−1.08	–	–	–
Change in relation to base x-stress	-	−65.7%	0.481%	−20.4%	−1.22%	−31.2%	–	–	–
$\tau_{y,glob}$ $[10^{10} m^4/s^2]$	−9.10	−12.6	−9.41	−12.0	−8.82	−12.5	–	–	–
Change in relation to base y-stress	-	38.6%	3.50%	31.8%	−3.07%	37.5%	–	–	–
τ_{glob} $[10^{12} m^4/s^2]$	0.608	0.859	0.596	0.838	0.610	0.842	–	–	–
Change in relation to base stress	-	41.4%	−1.97%	37.9%	0.355%	38.6%	–	–	–
T_{glob} $10^{13}[m^5/s^2]$	5.39	5.15	5.55	5.26	6.98	6.43	–	–	–
Change in relation to base pseudo-momentum flux	-	−4.35%	2.96%	−2.36%	27.9%	19.3%	–	–	–

Table 5.1: Summary of difference in bottom lee wave energy flux and stress and pseudo-momentum flux between the different topography sensitivity and IDEMIX parameter sensitivity experiments. Whereas the bottom energy flux is roughly $0.06TW$ in all estimates and differs only a maximum of 3.15% between the experiments, the bottom stress differs up to 40% between the difference runs. Using the anisotropic topography spectrum instead of the isotropic leaves large differences in the two components of the bottom stress throughout all the different experiments. Even though the bottom stress is increased with the anisotrpoic stress the pseudo-momentum throughout the water column remains fairly similar. The exception to this stems from using the new IDEMIX parameters found by Pollmann et al. (2017) with which the pseudo-momentum flux is increased by 27.9 and 19.3% respectively. The last three columns show the bottom energy flux integrated over the model domains of the 1/3° regional model of the North Atlantic and the 2° and 1/10° global models, respectively. From these, the increase of lee wave energy flux with model resolution i obvious.

addition of lee waves is thus also dependent on the background internal wave energy and the IDEMIX parameters. There is a very clear link between an increase in background internal wave energy (as compared with a the control run without lee waves) and energy transfer from lee waves to internal waves. Although the energy transfer takes predominantly takes place near the bottom, the background internal wave energy can be increased by up to as much as 5 times through the entire water column over the energy transfer.

Across the four topography sensitivity experiments the difference in the influence of lee waves on diffusivity remains very small, but changing the IDEMIX parameters, μ_0, $s_\star$, and τ_v, in experiments $P17I$ and $P17A$ alters the influence of lee waves on diffusivity. Although the lee wave energy itself is increased in experiments $P17I$ and $P17A$, the energy transfer to the background internal wave field is decreased (because α is decreased) and so is the difference in diffusivity. Actually, the more energetic lee wave field should be seen as a response to a lower energy transfer to the background internal wave compartment, rather than the other way around. Because of this lower energy transfer the diffusivity is clearly larger in experiment $I075$ than in $P17I$ and $P17A$ all of which shows diffusivities clearly larger than in the control run. It is most noticeable, however, that the diffusivity is mostly increased in the interior rather than near the bottom (relatively speaking). In a zonally averaged sense, on the contrary, it is shown that the diffusivity near the bottom is actually often decreased. This could be because of the weaker mean flow, on which the effect of the lee waves is more apparent.

The bottom velocity is in many regions reduced (compared with the control run) by as much as $0.1m/s$, and the correlation between a large bottom stress and a large decrease in bottom speed is very clear. This is the case all along the North Atlantic Current, but especially in the Western and Northern Atlantic. Furthermore, comparing the East and West Greenland Currents (where lee waves generation is allowed in the region of the former but not the latter) shows very clearly that the lee waves remove significant momentum from deep currents. If this hypothesis is accepted, the current model implementation should see lee waves as removing energy from the mean flow near the bottom, transferring it to the internal wave field in which it propagates and is ultimately transferred to the turbulent domain, where it is available for mixing. In this way, the addition of lee waves just as much increase the diffusivity in the interior (at least below $2500m$ depth) as it will near the bottom.

The integration length of one year was chosen in order to eliminate seasonal changes, but it has allowed a varying eddy signal to have an impact on average quantities above 1000m depth. However, since the lee wave generation is already inhibited in near coastal regions, where the ocean is shallower, the difference in the impact of eddies over the different experiments in the uppermost 1000 meters is mitigated in many regions. A longer integration is therefore recommended if the aim is to study the impact of lee waves in shallower seas, but it is not necessarily paramount in global models. As to whether which setting should be used for further investigation, it is clear that despite a larger bottom stress, the difference between the isotropic and anisotropic topography spectrum remains small in the North Atlantic. It is clear that changing the original IDEMIX parameters, μ_0, $j_\star$ and τ_v has a much larger influence on both the lee wave field itself and its influence on other variables, than changing the topography spectrum and especially than the critical inverse Froude Number.

Vertically averaging lee and internal wave energy in four depths bins does not directly contradict the ARGO-derived data from Pollmann (2020); neither using the lee and internal wave energy from experiments $I075$ and $PI17$. However, it does also not validate either one setting or the other. The difficulty in comparing the energy levels simulated by the model with those found by Pollmann et al. (2017) lie in the discrepancy between the depth of the ARGO data and the depth at which the lee wave energy is most heavily concentrated; whereas the ARGO data has its best coverage above $1000m$ depth in the northern Atlantic basin, the lee wave energy is in most regions primarily situated below $2000m$ depth. As such, in vertical averages above $1000m$ depth, the lee wave energy only directly constitutes i minor fraction of the total internal wave energy (i.e. lee wave plus background internal wave).

Chapter 6

Regional focus on the Southern Ocean

The Southern Ocean has previously been highlighted as a region of intense lee wave generation due to the deep reaching eddies in the region (Nikurashin and Ferrari, 2010a; Trossman et al., 2013). Additionally, several observational studies focusing on lee wave driven mixing have been carried out in this region. Cusack et al. (2017) made direct observations of the upward energy flux in a lee wave in Drake Passage, which aligned with that predicted from linear theory if the topographic blocking effect (the Froude Number limiter function applied in eq. 2.34) was taken into account. Although there seems to be agreement over the large lee wave generation here, multiple studies found discrepancies between the observed dissipation rates and the energy flux predicted from linear theory (Waterman et al., 2013; Sheen et al., 2013; Brearley et al., 2013). The interaction of the lee wave field with the mean flow has been suggested as a cause for this discrepancy. In the global 1/10° model the region does also show a large lee wave generation and a closer investigation of this region is therefore warranted. In this study this done in the global 1/10° model and the results are shown in the following section. All values are temporal averages taken over the last year of a four year simulation.

The lee wave energy flux on the entire model domain is shown in Fig. 6.1. The flux in the Southern Ocean is (along with that in the North Atlantic) the largest across the entire model domain with values reaching $10^{-4} W/m^2$ in many areas. The yellow line circumpassing the Southern Ocean is the path along which transects of the Southern Ocean (which will be shown later) are taken across. The magnitudes reached in the North Atlantic are similar to those calculated from the regional 1/12° model shown in the previous chapter.

To get an image of the effect of lee waves with depth, a transect of the Southern Ocean along the yellow line visible in Fig. 6.1 is shown in Fig. 6.2. The *upper left panel* shows the lee wave energy (notice the logarithmic scale), which is prominent in most of the transect and reaches maximum values of $10^{-1} m^2/s^2$. The lee wave energy is as a rule of thumb reduced by a factor of 10 within the deepest kilometer

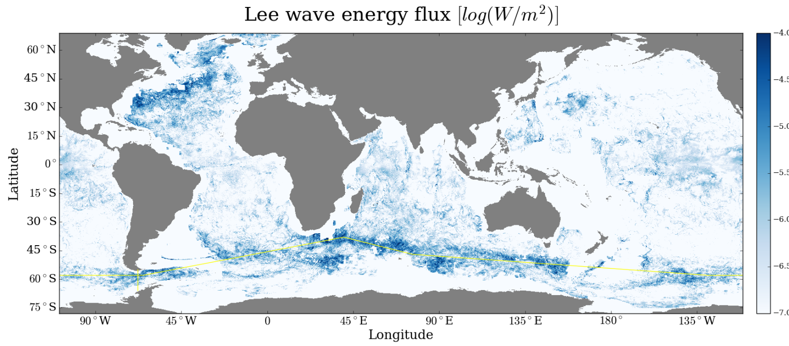

Figure 6.1: The bottom lee wave energy flux is largest in the Southern Ocean and in the North Atlantic, where it reaches values of $10^{-4} W/m^2$, and barely present in much of the Pacific. The yellow lines indicates sections across which transects were made.

in the water column. Along with the lee wave energy itself is shown the transfer to the internal wave domain (*upper right panel*), from which additional energy will be available for mixing, and the transfer to (*lower left panel*) and from (*lower right panel*) the mean flow. The vertical distribution of the transfer to the internal waves follows very closely that of the energy except for at roughly $2500m$ depth from about $60°$ to $80°E$, where the energy transfer seems reduced. In general the energy transfer is a factor of $10^{-6}s^{-1}$ times the lee wave energy.

The energy transfer to and from the mean flow (*lower left* and *lower right panel*) is generally lower than the transfer to the internal wave domain (*upper right panel*), although both can locally be as large. This depends very much on the region in question, though. But first and foremost it is more localized, and its vertical distribution much more irregular making the correlation with the lee wave energy lower. The transfer from the lee wave domain to the internal wave domain bears more or less the same vertical pattern as the lee wave energy itself, and this is not the case for the interaction with the mean flow. In general the transfer the mean flow occurs near the bottom, while the transfer from the mean flow will take place in the interior. This indicates that while lee waves can loose significant amounts of energy to the mean flow near the bottom, vertically propagating lee waves can in the interior ocean gain significant energy exchanges with the mean flow potentially affecting both the mean flow and the internal wave field in the interior. Areas where lee wave energy is persists more than $1500m$ above the bottom also show large energy transfer from the mean flow, indicating the importance of the energy exchange with the mean flow in the vertical profile of lee wave field.

The image shown here is not dissimilar to that shown at $37°N$ in the Atlantic in section 5.1.4. The lee wave energy field is in many areas in an approximate balance between the energy flux at the bottom and the transfer to the background internal wave field, but the mean flow interaction can locally upset this balance and provide or extract energy form or to the mean flow. But it is clearer here, how the exchange with the mean flow is able to alter vertical profile of the lee wave field.

Southern Ocean transect

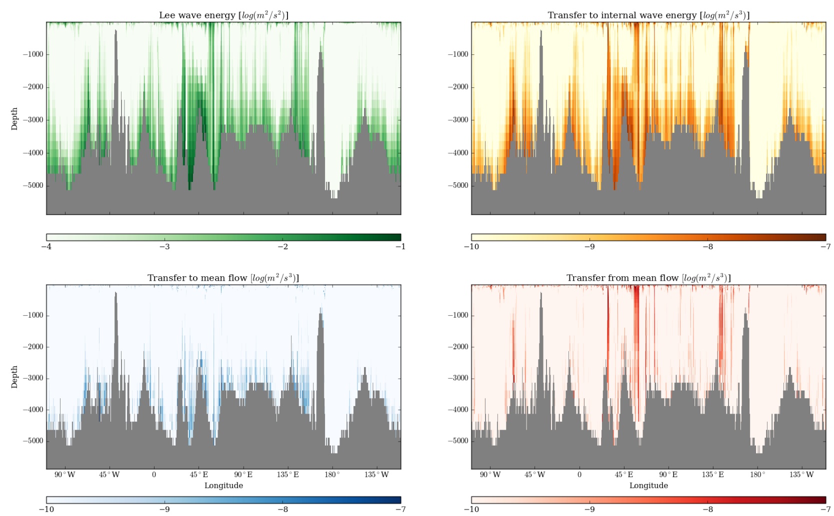

Figure 6.2: The lee wave energy (*upper left panel*) is present along the entire transect line and often acts on the lowest kilometer in the water column. It is mostly present in the regions of rough topography. The transfer to the internal wave domain (*upper right panel*) shows a very similar vertical distribution and is generally a factor of 10^{-6} times the energy itself. The energy transfer to (*lower left panel*) and from (*lower right panel*) the mean flow is lower and its vertical distribution more irregular, and the correlation with the lee wave energy obviously lower.

Both the transfer to the background internal wave compartment and the mean flow transfer were integrated vertically and horizontally over the entire model domain (i.e. globally) and amounts to $T_{IW} = \int_x \int_y \int_z \alpha_{ww} E_{iw} E_{lee} \partial x \partial y \partial z = 2.2 GW/s$ and $T_U = \int_x \int_y \int_z \tau_{lee}^{-1} E_{lee} \partial x \partial y \partial z = 0.086 GW/s$. In the latter the direction of the transfer has been taken into account, which means that over the entire model domain the energy transfer of the mean flow interaction is from the mean flow to the lee waves. Integrated globally, however, the energy transfer from the mean flow is roughly 1/25 of the transfer from lee waves to the background internal wave domain.

Along with the lee wave energy and the energy transfers to and from the lee wave domain, the internal wave energy (*upper left panel*), buoyancy frequency (*upper right panel*), diffusivity (*lower left panel*), and the dissipation rate of turbulent kinetic energy (TKE) (*lower right panel*) is presented in Fig. 6.3. The internal wave energy reaches maximum values of around $10^{-2} m^2/s^2$, but the vertical distribution is much more uniform than that of the lee wave energy. Increased values of internal wave energy can be seen at the regions of rough topography near $70° W$, $50° E$, and $170° E$ which coincides very well with regions of large energy transfer between the two compartments. The diffusivity shown is clearly elevated in several near bottom regions. It reaches values of or close to $0.1 m^2/s$ near the bottom in particular at $70° W$, $170° E$, and $125° W$. At the first and last of these three longitudes an elevated diffusivity is persistent throughout much of the water column, which is mirrored by the large amount of internal wave energy, while the second is characterized by the diffusivity being very large solely near the bottom. The cause of the large diffusivity here seems to be a very low buoyancy frequency rather than large amount of internal wave energy. This shows perfectly well how the diffusivity depends on the ratio of internal wave energy to the stability frequency. Furthermore, both the first and the third of these regions coincide with regions of a large lee wave energy transfer. Thus, the lee wave field and its subsequent energy transfer to the internal wave field - as present at roughly $50° E$ and $170° E$ - is very well able to have a significant impact on the diffusivity. The dissipation of TKE reaches values between $10^{-8} m^2/s^3$ and $10^{-7} m^2/s^3$ at several longitudes in the transect, which coincide with large amounts of internal wave energy and high diffusivities.

The Drake Passage has long been acknowledged for both its particular role in Southern Ocean dynamics (Pedlosky, 2013) and as a region of intense lee wave generation (Nikurashin et al., 2013). Furthermore, it was also the region in which the first unambiguous observation of a lee wave was made (Cusack et al., 2017). Thus, it is only appropriate to apply special attention to this region. In a cross section of the Southern Ocean at $68° W$ over the Drake Passage (this section is marked with a yellow line in Fig. 6.1) lee wave generation and dissipation has been examined.

As with the transect of the Southern Ocean, the lee wave energy (*upper left panel*), the transfer from lee waves to internal waves (*upper right panel*) and the transfer to (*lower left panel*) and from the mean flow (*lower right panel*) is presented in the cross section of the Drake Passage in Fig. 6.4. Lee wave energy is present in almost the entire cross section reaching maximum values of $10^{-1} m^2/s^2$ in the central and northern part of it. The large lee wave energy also results in a large transfer to the internal wave domain of $10^{-7} m^2/s^3$ in the central part of the cross section. Noticeable in this exact area, though, is also the large energy transfer from the lee wave field to the mean flow. This transfer is only present in the bottommost kilometer (or so), but its magnitude is in at several latitudes in the entire cross section equal or at least close to that of the internal wave transfer.

The energy transfer from the mean flow to the lee wave field reaches maxima around $10^{-8} m^2/s^3$ close to $60° S$. Here the transfer persists in most of the water column. This also result in the lee wave energy, and subsequently the transfer to the internal wave field being elevated throughout the water column. Close $57° S$ the transfer from the mean flow is close to the same magnitude near the bottom with similar effect on the lee wave field and transfer to the background internal wave field.

Although the transfer to/from the mean flow over the entire cross section is lower and still more localized than the transfer to the internal wave domain, it is also clear

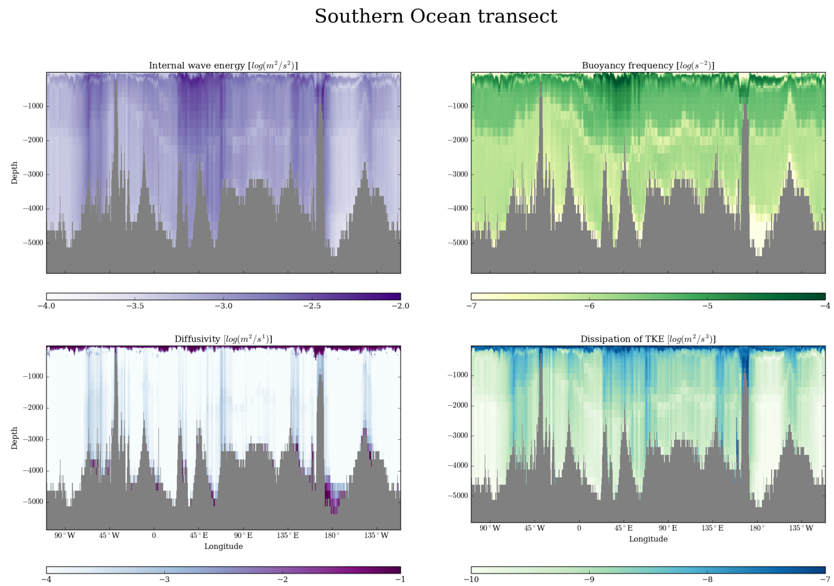

Figure 6.3: The *upper left panel* shows the background internal wave energy at the transect along the Southern Ocean. The energy is in general more evenly distributed in the vertical than the lee wave energy, but is also lower than the lee wave energy is near the bottom. Regions of very large background internal wave energy correspond very well with regions of very high energy transfer from the lee wave field. The *upper right panel* shows the (square of the) buoyancy frequency, which exhibits a clear pycnocline and a minimum of $10^{-7}s^{-2}$ near 180°. The *lower left panel* shows the diffusivity, which is clearly increased in regions of very high internal wave energy and regions of very low buoyancy frequency. The *lower right panel* show the dissipation rate of TKE, which is elevated to local maxima between $10^{-8}m^2/s^3$ and $10^{-7}m^2/s^3$ in regions of high internal wave energy and high diffusivity.

here, that the energy exchange between lee waves and mean flow can locally be of the same magnitude as the transfer to the background internal wave field. The interaction with the mean flow also show here to have a significant effect on the vertical profile of lee wave energy in specific locations.

In figure 6.5 the internal wave energy, stratification, diffusivity, and dissipation rate of TKE is shown in the same cross section of the Drake Passage. The southern part of the cross section shows both less internal wave energy (*upper left panel*) and lower buoyancy frequency (*upper right panel*) compared to the northern part of the section. The internal wave energy increases towards the north at all depths, and this image is mirrored in the the buoyancy frequency. There are, however, traces of increased internal wave energy in the lowest $1500m$ or so from roughly $61°S$ north-

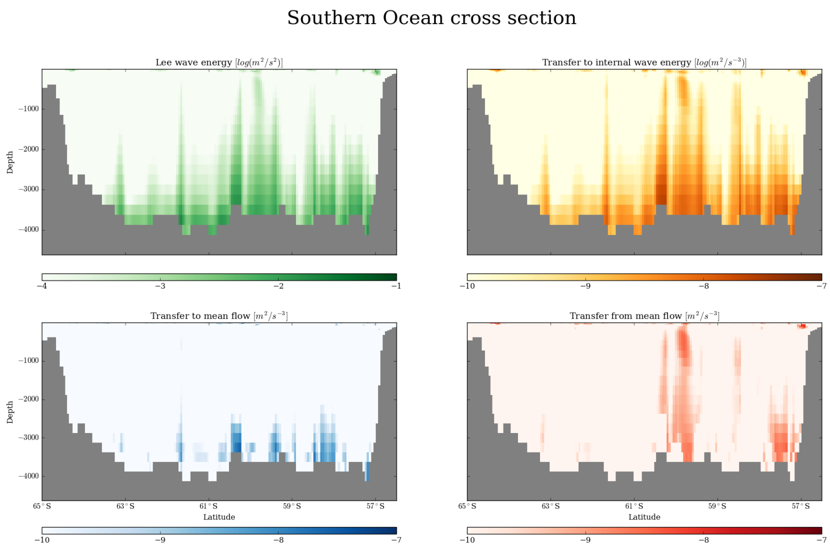

Figure 6.4: Over basically the entire cross section of Drake Passage at $68°W$ lee wave energy (*upper left panel*) is present in the bottommost $1000m$. The vertical profile of the transfer to the background internal wave energy (*upper right panel*) is very similar to that of the lee wave energy. The transfer to the mean flow (*lower left panel*) can locally be as large as that to the internal wave field, but it mainly occurs in the bottommost kilometer. The transfer from the mean flow to the lee wave field (*lower right panel*) can also have the same magnitude, occurs both near the bottom and in the interior. As such, large energy transfer from the mean flow significantly impacts the vertical profile of the lee wave field and subsequently the transfer to the internal wave field.

wards. This clearly correlates with the large energy transfer from the lee wave field, and shows the ability of the lee wave field to impact the internal wave field. The diffusivity (*lower left panel*) is close to the canonical Munk value of $10^{-4}m^2/s$ in much of the southern half of the section. In several near bottom locations in the northern half of the section the diffusivity reaches $10^{-1}m^2/s$. In the interior of the northern half (especially below $2000m$ depth) the diffusivity remains around $10^{-3}m^2/s^2$, but the traces of increased internal wave energy is clearly visible. As such, the impact of the lee wave field on the diffusivity is clearly seen. Close to $60°S$, for instance, the internal wave energy is elevated through out the water column as is the diffusivity. This coincide very well with a large lee wave energy transfer throughout the water column. Similarly the TKE dissipation rate is increased towards the north reaching magnitudes above $10^{-8}m^2/s^3$ in the interior. As in Fig. 6.3 the TKE dissipation rate is increased in regions of high internal wave energy and diffusivity.

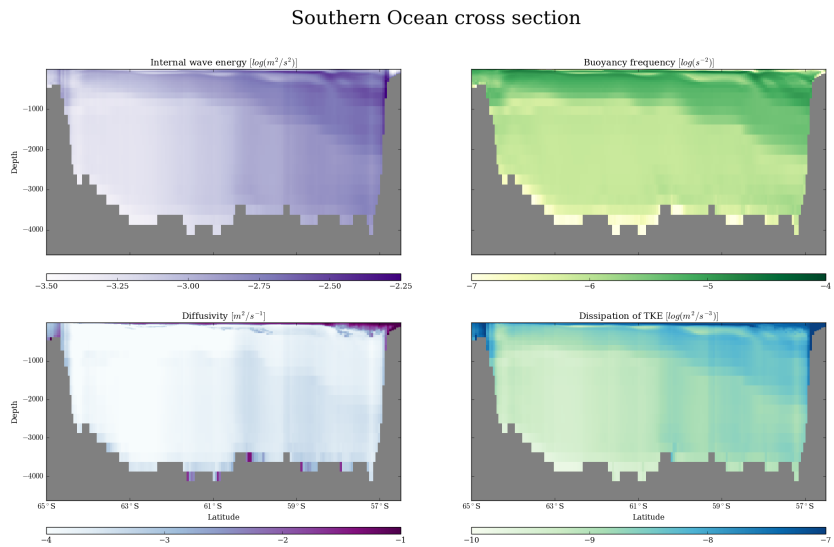

Figure 6.5: The background internal wave energy (*upper left panel*) increases at all depths towards the north in the northern part of the cross section. This is mirrored by the buoyancy frequency (*upper right panel*). The diffusivity (*lower left panel*) is near the Munk value of $10^{-4} m^2/s$ in most of the southern half of the section. In the northern half it is increased in much of the interior and exhibit near bottom maxima close to $10^{-1} m^2/s$. Regions of increased internal wave energy and increased diffusivity also show a high dissipation rate of TKE (*lower right panel*), which reaches magnitudes of 10^{-8} in the interior. These regions coincide very well with regions of large energy transfer from lee waves, highlighting the ability of the lee wave field to affect the diffusivity and dissipation of TKE.

In general the energy of the lee wave field simulated in the Southern Ocean 1/10° POP model resembles those in the 1/12° regional North Atlantic FLAME model. Energy transfer from the lee wave to the background internal wave field remain the dominant route of lee wave dissipation. It is, however, also clear the the interaction with the mean flow plays a larger role here, than was the case in the North Atlantic. This energy exchange is still more localized than the energy transfer to the background internal wave field, but it is significant throughout a much larger area. In general, the mean flow extract more energy from the lee waves towards the bottom, and provide more energy for lee waves in the interior. This reinforce claims in previous studies, that lee wave-mean flow interaction could play a role in the discrepancy between observed TKE dissipation rates and that calculated from lee wave theory (Waterman et al., 2013; Sheen et al., 2013). Dissipation rates of TKE modelled by IDEMIX exhibit magnitudes of $10^{-8} m^2/s^3$ at several locations in the Southern

Ocean. Regions of high TKE dissipation rates coincide with those exhibiting large amounts of internal wave energy and high diffusivity. These magnitudes are comparable to observations in both the Drake Passage and Kerguelen Plateau (St. Laurent et al., 2012; Sheen et al., 2013; Cusack et al., 2017; Waterman et al., 2013), where lee waves has been highlighted as primary a source of internal mixing.

Chapter 7

Discussion and outlook

While some aspects of the investigation of the different settings in the lee waves implementation are clear - the bottom energy flux does not change much regardless of the lee wave parameters, but a change in the IDEMIX parameters significantly alters the lee wave field - other aspects are less clear. A few of the research questions thus have a clear answer, while others reveal a complexity in the model implementation and a discussion of possible reasons for this ambiguity is warranted. There are also several sources of uncertainty in both the lee wave energy flux, in IDEMIX, and in topography data, which needs to be addressed. Furthermore, the results presented in the previous chapters ought to be put in a broader scientific context. That is the purpose of this chapter.

The assumptions made in the derivation of the lee wave energy flux have their foundation primarily in the work by Bell (1975) and Olbers (1976), while a few were of a practical nature. While the scheme from Bell (1975) has laid the foundation for most studies on lee waves (Nikurashin and Ferrari, 2010b; Scott et al., 2011; Wright et al., 2014) a scheme originally used to parameterize mountain drag in the atmosphere - the scheme of Garner (2005) - has also proved useful in calculating lee wave energy fluxes (Trossman et al., 2013). In the formulation of the energy equation it is assumed that the energy density spectrum of lee waves stay close to that at the bottom. This is not necessarily the case in the real ocean. Although the GM-model (Garrett and Munk, 1975) suffers from regional biases and discrepancies (Polzin and Lvov, 2011), it is nonetheless widely accepted as a standard lense, through which internal wave energy spectra is calculated. The GM-model does not capture the density spectra of the Bell flux, and to the author's knowledge no attempt exists to measure energy density spectra in accordance with the Bell flux. The ratio of background internal to lee wave energy simulated in this study, indicate that the lee wave energy constitute a major fraction of the total internal wave energy (background plus lee wave) in many regions - the central northern Atlantic and Southern Ocean, for instance - in the interior ocean (taking the entire water column into account). Since the interior ocean is where the GM-model fares best (Polzin and Lvov, 2011), an overestimation of the total lee wave energy is a possibility. The need for detailed observations of lee waves (their energy flux, their propagation and their dissipation) to constrain the dissipation of lee wave energy and thus to calibrate an internal wave model to arrive at a realistic energy field, is obvious, but their dependence on a time-varying eddy-field and their generation in the deep ocean make such observations challenging (Legg, 2021). Quantifying a potential discrepancy between observed internal wave energy and that simulated in the model was attempted in section 5.5, but is, as mentioned, also difficult because of the discrepancy between the depth at which measurements of internal wave energy exists, and the depth at which the lee wave energy is located in the model simulation. The observational data compared with here was based on fine-scale parameterizations of internal wave dissipation, but this method has previously been hypothesized to not capture the physics behind lee wave dissipation (Waterman et al., 2014).

The formulation of the energy equation for lee waves introduces the parameter, r, in the denominator of the shape function $A(k,\phi)$ to avoid singularity when lee waves are generated at a frequency $\omega = f$. This does, however, also introduce a dependence of the mean flow interaction on this parameter, r, which is of course not ideal, but it is necessary when integrating in order to formulate the very neat expression for the isotropic flux. Quantifying this dependence thoroughly has not been attempted, but it is noted that the dependence is weak especially in the high energy wavenumber domain.

7.1 Eddies and resolution

The integration length of a single year was chosen to eliminate possible seasonal influences. It is not viable to claim, for instance, that the addition of lee waves in an internal wave model increase the diffusivity by such and such an amount in the North Atlantic, if one only looks at winter months, where mixing is generally larger. But it seems that the integration length still permits a varying eddy field to have an effect on the average of some quantities in some regions in the topography and IDEMIX parameter sensitivity experiments. This shows itself in large differences in stratification seen as tongues of varying sign stretching down to about 2000m depth, although not shown in Fig. 5.17. The varying eddy field is more apparent at shallower depths as seen in Fig. 5.20, where it is also clear that the effect of lee waves on the mean flow increases with greater depths. In essence this means that variances in both stratification, diffusivity and other quantities above a certain threshold is more likely to be the result of a varying eddy field rather than changes in the internal wave field. The depth of this threshold also depends on the region in question. It is of course desirable to isolate the effect of lee waves on the rest of the variables, but it seems like the integration length still permits the varying eddy field to have some impact on average quantities above a certain depth. The effect of eddies on the generation of lee waves are, however, also of general interest. The *right panel* in Fig. 5.2 shows the bottom speed in regions where lee wave generation is permitted by the topographic spectrum data.

Traces of an eddy field is apparent in the bottom speed, but it does not seem as if particular eddies in particular regions stand out in the average speed over the integration period, where lee waves are generated. This would have been a cause for such a region to not be representative for a mean state or a mean lee wave generation. It could (and is probably more likely to) be the case in shallower seas, but here the lee waves are already inhibited by the topography data. Put differently, the topographic data already inhibits lee wave generation close to coastal areas, where the ocean is shallower, and where a varying eddy field would be more likely to have an effect on the variance of lee wave generation (at least in the current model domain), which should not be considered representative for a mean state. This means that while eddies are considered necessary for the generation of lee waves, it is not the case that a varying eddy field produces an irregular lee wave field. The global lee wave energy flux and stress at the bottom are plotted as a function of time in Fig. 5.4. The lee wave bottom stress is remarkably steady throughout the entire simulation only varying a few percentages, with the lee wave flux varying up to $20-25\%$. A certain variance is to be expected, though, especially given that the bulk of the lee wave generation takes place in only a few regions in the model domain. Indeed several authors have pointed out the need for deep reaching eddies to create lee waves, although the focus have primarily been on the Southern Ocean (Yang et al., 2018; Nikurashin et al., 2013). In this study it is obvious that lee wave generation is especially strong in regions where the eddy field is strong as well. This is mainly the western Atlantic, along the North Atlantic Current and in the Southern Ocean. Lee wave generation is can also be strong in areas where the eddy field is not the primary driver, for instance the Denmark Strait. It is again noted that, in general the lee wave generation is supressed in near coastal regions by the topography data, where one finds shallow depths, and where it would thus be reasonable to assume that eddies would more often be able to reach the bottom and contribute to lee wave generation. Regarding the effect of eddies in high latitudes, it is also worth having in mind, that the Rossby radius of deformation, which determines the scales of the eddies varies from around $100km$ in the tropics to a few kilometers in the high latitudes (Hallberg, 2013). This means that eddies are not nearly as well resolved in high latitudes as in mid-latitudes or southward thereof, which can have an effect on the bottom flow in the high latitudes and therefore on the lee wave generation. The magnitude of the bottom stress is, in the isotropic case, given as the bottom energy flux divided by the bottom speed, $\tau = F \cdot |U_0|^{-1}$. The fact that the bottom stress varies less than the flux means that (on average) the bottom speed act as a damping factor. This could point toward the eddy field having a smaller impact on the generation of lee waves. A detailed examination of the correlation between the distribution of unresolved eddy kinetic energy in coarse and high resolution models and the lee wave energy flux in higher resolution models could prove fruitful in qualitatively determining the effect of the eddy field on lee wave generation. This would be the first step in a parameterization of the lee wave energy flux in coarse resolution models.

The two experiments using coarser resolution models (the $1/3°$ FLAME setup and the $2°$ setup) clearly shows that the lee wave energy flux is not simulated properly in coarse resolution models most likely due to the absence of a resolved eddy field. A formulation of a parameterized lee wave energy flux, which is dependent of the eddy kinetic energy should therefore be examined. An attempt at such a parameterization has - to the author's knowledge - not been undertaken, but could be carried out within the pyOM-IDEMIX framework. Indeed, pyOM already couples the parameterized eddy kinetic energy to the internal gravity wave domain, which is modelled by IDEMIX, so an additional energy energy flux from the EKE to a lee wave domain would be completely in line with the current model formulation. The meso-scale eddy energy and its role in larger energy cycle in pyOM is presented in Eden and Olbers (2014). The governing equation for eddy kinetic energy E_{eke} in pyOM is given as

$$\rho_0 DE_{eke} = -\nabla\cdot F + \rho_0 A_h (\nabla_h \overline{\mathbf{u}})^2 + \rho_0 g^2 K_{gm} \frac{|\mathbf{e}_h|^2}{N^2} - \rho_0 \epsilon_{eke}$$

where the first term on the right hand side, the flux divergence term, only signifies a lateral diffusion. The second term on the right hand side represents the energy flux from the mean kinetic energy due to lateral friction, with A_h being the lateral viscosity, the third term on the right hand side is the eddy mixing term, which draws energy from the dynamic enthalpy, and the last term on the right hand side is the dissipation to the internal gravity wave domain. Adding a negative term on the right hand side of this equation to account for the energy flux to lee waves should be possible, even while keeping the coupling of the lee wave domain and the background internal wave domain intact. In a coarse resolution model, an additional term in a lee wave energy equation could be a mean energy flux term, but the balance between fluxes from mean and eddy kinetic energy would require consideration. In the $1/10°$ global model in this study the total lee wave energy flux amounts to $0.24TW$, which is in line with previous estimates, and the two terms representing mean and eddy kinetic energy fluxes should amount to a similar figure when integrated over the model domain. Both an eddy-lee wave flux term and a mean flow-lee wave flux term should be dependent on the eddy and the mean energy themselves, and also on the topography data to ensure a realistic geographical distribution. Further specification of such formulation of the two terms is not the scope of his study, and requires further investigation of the results from the eddy resolving model.

7.2 Bottom stress

The question of why the bottom stress increases significantly, while the bottom flux does not, when using the anisotropic topographic spectrum instead of the isotropic one, is not straightforward, since their respective dependence on the topography spectrum are similar. As mentioned, the bottom stress is given by the bottom energy flux divided by the dot product of the bottom velocity and $\mathbf{n}$. In the isotropic case, the flux is approximated and in the anisotropic case it is evaluated numerically over both wavenumber and propagation angle, which the bottoms stress then also is. This raises the question of what effect the numerical scheme and the numerical resolution in k- and ϕ-space has on the bottom energy flux and therefore on the bottom stress in the anisotropic case. An apparent way to test this would be to vary this resolution, but this is computationally very expensive. Indeed it is one of the reasons why IDEMIX to begin with divides and analytically integrates the internal wave energy into angular compartments in the first place. Quantitative numerical experiments of the energy flux and bottom stress as a function of the resolution in k- and ϕ-space (although not presented here) does not show a significant difference to the resolution used in anisotropic experiments, however.

Fig. 5.25 tells us that, besides the bottom most grid points, the lee wave energy is generated in equal amounts at depth in the case of the two spectra, so above 4500m depth, the energy generated at each depth index is most likely very similar in all experiments. This would point to the difference in bottom stress resulting from the relation between the direction of propagation and the the direction of the mean flow, i.e. a difference in the dot product $\mathbf{U_0} \cdot \mathbf{n}$. The angle of the bottom stress as examined in two different regions (the western Atlantic and the Denmark Strait) over the four topography sensitivity experiments only shows a clear systematic difference between using the iso- and anisotropic topography spectrum in one of the regions, the Denmark Strait, whereas in the western Atlantic the change with the critical inverse Froude Number is much clearer and more systematic. Despite this, an angular shift in the bottom stress towards a more meridional direction with the anisotropic spectrum (which the *average* increase in the meridional component and the decrease in the zonal component of the stress indicate), could be the result of a shift in the dot product $\mathbf{U_0} \cdot \mathbf{n}$. Such a detailed investigation has not been carried out, however. The question of why the bottom stress increases with the anisotropic spectrum is also rendered less important, by the fact that the vertically (and horizontally) integrated pseudo-momentum flux varies much less over the topography sensitivity experiments.

7.3 Diffusivity

The lack of increase in diffusivity - in a zonally averaged sense - despite a very energetic lee wave field (especially towards the bottom) is interesting. This is in contrast with the result of Nikurashin and Ferrari (2010b), where bottom mixing rates is clearly increased with the implementation of a lee wave energy flux in an idealized model study. With the current implementation the diffusivity is only directly linked with the background internal wave field. The link with the lee wave field comes about from the exchange between lee waves and the background wave field with the term $\alpha_{ww} E_{iw} E_{lee}$ in Eq. 2.46. In other words, the lee waves can only affect the diffusivity indirectly via the background internal wave field. The (horizontally integrated) energy transfer from the lee wave compartment to the background wave field and lee wave energies (which are plotted in Fig. 5.13), show that the energy is mostly transferred in the deep ocean. This is the case for all experiments, although the experiments using IDEMIX parameters from Pollmann et al. (2017) shows a slightly decreased energy transfer below $4000m$. It is evident, however, from Fig. 5.14 and Fig. 5.15 that although the energy transfer mostly takes place near the bottom, the internal wave energy is increased throughout the water column. The largest differences in diffusivity (as compared with the control run) are still seen towards the bottom, however. These differences can be both positive and negative depending on the exact location, and there seem to be little direct correlation between these differences and lee wave energy or energy transfer at the specific locations. Rather they are correlated with changes in the local buoyancy frequency. Furthermore, an increase in diffusivity compared to the control run is still observed in the interior ocean in Fig. 5.30. This shows how the propagation of internal wave energy is of great importance to the diffusivity modelled by IDEMIX. Another sensitivity experiment, which could could be of obvious interest, would therefore be to vary the vertical decay scale of both the lee wave energy and the internal wave energy, or to vary the transfer coefficient α. Changes in these parameters would influence the variation with depth of both lee wave energy and the transfer to the background internal wave field. Previous studies which effectively although not directly involving the propagation of lee waves reveal a weaker although qualitatively similar effect on lee wave driven mixing. In general, little is known about the vertical propagation of lee waves (Melet et al., 2015), and this results in the poor constraints in the implementation. Still, observational studies have shown lee waves to propagate far from their generation site and contribute to internal mixing in the interior (Meyer et al., 2015a).

The specific implementation of the lee wave module into the IDEMIX model is done mainly because of the different shape in wavenumber space of the lee waves and the rest of the internal wave field and because of a frequency mismatch. The practicality of separating the lee wave module with the rest of internal wave model is thus meaningful, but when it comes to wave breaking and subsequently mixing the separation is perhaps somewhat arbitrary. There is no theoretical argument why the breaking of lee waves would not directly affect ocean mixing. Despite discrepancies between observed dissipation rates and that predicted from lee wave theory (Waterman et al., 2013; Sheen et al., 2013), Cusack et al. (2017) reports TKE dissipation rates of $10^{-7} W/kg$ within a lee wave in the Shackleton Fracture Zone in the Drake Passage. As such, the energy transfer from the lee wave to the background internal wave field predicted in this study is not contradicted by what is (to the author's knowledge) the only direct observation of lee wave driven mixing.

The effect on diffusivity (as *best* quantified by the difference between the base and control experiments) due to the lee wave energy transfer at a single grid point is difficult to quantify though, because it relies on the *local* balance of TKE. Before any effects of differences in the local buoyancy frequency and the advection of internal wave energy is taken into account, however, the difference in diffusivity must be proportional to the energy transfer (or rather to the square of the energy transfer, since the diffusivity is proportional to the square of the internal wave energy). A recurring image throughout the study is that contrary to what might have been expected, the diffusivity near the bottom is not increased (*universally*, at least), no matter the IDEMIX or lee wave parameters. This is, however, due to an increase in buoyancy frequency near the bottom. At $37°N$ the diffusivity near the bottom exhibits both significant increases and significant decreases depending on the longitude, but the internal wave energy is significantly increased in the entire water column, where energy is transferred from lee waves at the bottom. The internal wave energy being increased *throughout* the water column, and not just near the bottom, can thus interpreted as a result of the lee waves disturbing the *local* balance of TKE. Because the background internal wave energy is then allowed to propagate upwards, the increase in internal wave energy is also shifted upwards until the local balance of TKE is reached.

Although the largest numerical differences in diffusivity is best correlated with changes in the buoyancy frequency, the lack of increase in diffusivity near the bottom is also some degree the result of the lee wave compartment not being directly linked with the diffusivity. The formulation chosen in this model is based on energy transfer from low to high vertical wavenumbers as shown by Olbers (1976), but the underlying assumption of this scaling is that the internal wave energy takes on a GM-spectrum shape, which is precisely not the assumption for the lee wave energy in the model. In general the energy exchange between lee waves and internal gravity wave or simply between waves of different energy spectra is an unexplored field, and the further research into this area is needed in order to formulate a more robust energy transfer term in this model.

An alternative formulation would, obviously, be to couple the lee wave field *directly* to the diffusivity on par with the background internal wave energy. Such a formulation would most likely increase the sensitivity of the diffusivity to the lee wave parameter settings; the topography and critical inverse Froude Number. Furthermore, it would probably also shift the increase in diffusivity towards the bottom, as the vertical propagation of internal wave energy would become less important. The effect of lee waves on the buoyancy frequency remain an open question, however. The theoretical argument for lee waves increasing buoyancy frequency near the bottom is unclear, but it is possible that a different coupling of the lee wave field and the background internal wave field can elucidate this question as well.

7.4 Outlook

As such, there are two clear further investigations which can be carried out within the framework of the current model formulation; a detailed examination of the correlation and dependence of the lee wave energy flux on the unresolved eddy kinetic energy with the scope of formulating a parameterization of this dependence, and the effect of a *direct* coupling of the lee wave energy field to the diffusivity as calculated by IDEMIX. Whereas the former requires a more thorough statistical analysis than provided here in order to obtain a realistic amount and distribution of lee wave energy, the latter requires a reformulation of the current lee wave-diffusivity coupling, and since such a coupling would likely be dependent on the lee wave energy (as is the energy transfer term in the current formulation) and also an investigation of the effect the transfer coefficient α_{ww}.

Furthermore, the large lee wave energy and energy flux found in every model used in this study in the Denmark Strait is also a potentially rewarding topic. This is a region characterized by the overflows of deep water formed in the Nordic Seas into the Atlantic, which is of great importance to the AMOC, why its representation in ocean models is crucial (Legg et al., 2009; Danabasoglu et al., 2014). Mixing from mesoscale eddies has been reported to modulate water property changes in the region, while also suggesting that internal waves may be important in the water transformation process (Koszalka et al., 2017). In light of this, the diffusivity induced by lee waves as well as the significant wave-mean flow interaction suggested in this study could be of importance in the region.

Chapter 8

Final Conclusions

The implementation of a lee wave module in IDEMIX has been thoroughly investigated across several model setups and experiments using different parameter settings. Comparisons of a coarse non-eddy resolving global model with a horizontal resolution of 2° and an eddy resolving global model of 1/10° horizontal resolution, first and foremost demonstrates how the lee wave generation, as quantified by the bottom energy flux, varies significantly with resolution; from $0.0114TW$ in the coarse resolution model to $0.262TW$ in the high resolution model. The increase in energy flux is in large part due to the resolved eddy field and the high bottom velocities associated with deep reaching eddies. As such, the energy flux is increased by several orders of magnitude along the North Atlantic Current and in the eastern section of the Southern Ocean. Comparing two setups of the regional FLAME model of the North Atlantic adopted in pyOM - one using an eddy-permitting resolution of 1/3°, and one using an eddy-resolving resolution of 1/12° - reinforces this image. The largest differences in lee wave generation are here attributed to the increases in regions of a visible eddying flow. Integrating the energy flux over the two model domains reveal a six time increase in the high-resolution model.

In the 1/12° regional FLAME model setup the lee wave field constitutes a major fraction of the total internal wave field (lee waves plus background internal waves); in some regions even by far the largest part. By far the bulk of the lee wave energy is situated below $3000m$ depth. The lee waves are able to remove significant momentum from the mean flow resulting in decreases in bottom velocities of more than $0.1m/s$ in high generation regions, most noticeably the western and northern Atlantic and the Denmark Strait. In regions of high lee wave energy these decreases can in large part be persistent throughout much of the water column. In the current implementation the lee wave field is connected to the internal gravity wave field via an energy transfer term $\alpha wwE_{iw}E_{lee}$. This energy transfer constitutes the route by which most of the lee wave energy dissipates - the other way being through interaction with the mean flow which can transfer energy both from the mean flow to the lee wave field and vice versa - and the lee wave field is in many areas in an approximate balance between the energy flux at the bottom and the energy transfer to the background internal wave field. This energy transfer also form the connection between the lee wave field and the diffusivity. Although the lee wave energy is most heavily concentrated below $3000m$ the lee waves act mostly, in the current model formulation, to increase the diffusivity in the interior. While diffusivities are often decreased near the bottom (due to an increase in buoyancy frequency), the interior ocean exhibits relative increases in diffusivity by up to a whole order of magnitude. These diffusivity increases in the interior are clearly linked to regions of elevated internal wave energy resulting from energy transfer from the lee wave field.

Four experiments using the IDEMIX parameter values of Olbers and Eden (2013) were carried out to investigate the sensitivity of the lee wave module to the two essential topography settings; the isotropic vs. anisotropic spectrum and the value of the critical inverse Froude Number set to $Fr_c = 0.75$ and $Fr_c = 0.5$, respectively. The bottom lee wave energy flux integrated over the entire model domain was found to vary very little although systematically with both the topography spectrum and the critical inverse Froude Number. Ranging from $F_{glob,A075} = 0.0612TW$ to $F_{glob,I05} = 0.0641TW$ the largest difference across these four experiments was $0.0029TW$. Furthermore, both the horizontally integrated lee wave energy as a function of depth and the geographical distribution of lee wave energy showed very small differences across the four experiments. The bottom lee wave stress on the other hand showed significant differences between the experiments using the isotropic and those using the anisotropic topography spectrum. In general, the zonal-component of the bottom stress was numerically reduced while the meridional component was numerically greatly increased with the anisotropic spectrum, resulting in an increase of the magnitude of the stress by close to 40% of that of the base experiment. This implies a shift in angle towards the meridional with the anisotropic topography spectrum, but a closer investigation of the bottom stress in the western Atlantic and the Denmark Strait revealed that this very much depends on the region in question.

Two additional experiments were carried out using the IDEMIX parameter values found by Pollmann et al. (2017); one using the isotropic topography spectrum and the other using the anisotropic spectrum. Comparing results from these two with those of the base experiment revealed a much larger sensitivity to the IDEMIX parameters. Because of a lower value of the energy transfer coefficient α_{ww} (which depends on the IDEMIX paramters μ_0, $j_\star$ and τ_v) the energy transfer to the internal wave field was significantly reduced, thereby causing an increase by an order of magnitude of the vertically integrated lee wave energy in many regions. The diffusivity is still increased in the interior in the two IDEMIX parameter sensitivity experiments, but not as much as in the previous four topography sensitivity experiments due to the lower energy transfer from the lee wave compartment to the internal wave compartment.

Comparing the vertically averaged total internal wave (i.e. background plus lee wave) energy in the Atlantic with internal wave energy estimates derived from ARGO-data has not revealed a strict contradiction between the two. This comparison has also shown to be troublesome, though, due to the discrepancy between the depth at which the bulk of the lee wave energy is situated and the depth at which the coverage of the ARGO data is satisfactory. Regions in which lee wave energy is situated at relatively shallow depths (for instance over the Mid Atlantic Ridge near the Azores), has exhibited energy levels, which might be an overestimation compared to the ARGO-data.

In the 1/10° model the lee wave-mean flow interaction has been shown to be of greater importance in the Southern Ocean as compared to that in the northern Atlantic in the 1/12° model. In the Southern Ocean the energy energy exchange with the mean flow can locally be as larger as the transfer to the background internal wave field. The general trend is that the lee waves transfer energy to the mean flow near the bottom, while the opposite transfer takes place in the interior. As such, the lee wave-mean flow interaction can significantly impact the vertical profile of lee wave energy. The dissipation rates of turbulent kinetic energy simulated by the model are elevated in regions of high lee wave activity in agreement with several observation estimates (Sheen et al., 2013; Brearley et al., 2013; Waterman et al., 2013). These results reinforce the image that lee waves can have significant impact on mixing in the Southern Ocean, but they also highlight the potential route of lee wave energy removal via mean flow interaction, which has previously been suggested as a possible explanation for the discrepancy between observed and simulated mixing rates (Waterman et al., 2013).

All in all, the combined results presented in this thesis provides a clear image of lee waves being able to significantly affect the mean flow and dissipation. The sensitivity of lee wave generation to model resolution opens a possible investigation of a parameterization of the lee wave field based on the eddy kinetic energy, while possible alternatives to the current implementation, such as a direct link between the diffusivity and the lee wave energy compartment, is also worthy of examination. Furthermore, the difficulty in comparing the ARGO-derived estimates of internal wave energy with the lee wave energy simulated by the model, highlight the need for direct and/or indirect observations of lee waves to provide realistic constraints in ocean models.

Appendix A

Additional results from topography sensitivity experiments

Several figures in section 5 contain images including only results from the base experiment, $I075$. All of these figures have been made with results from all lee wave parameter sensitivity experiments, i.e. using original IDEMIX parameters but varying topography spectrum and inverse Froude Number. They were absent in section 5, because the general image is that the difference between these four experiments is rather small compared to their respective difference to the control run. However a few of them is shown here for documentation purposes.

The biggest difference between the four topography sensitivity experiments is as mentioned in the bottom lee wave stress, where there is an increase of roughly 40% when using the anisotropic spectrum, as already pointed out in table 5.1. Nevertheless, the documentation of said differences (or lack thereof) is important for choice of parameters in the implementation of a lee wave component in IDEMIX. Since the difference in bottom stress is already showed in section 5.3 and the vertically integrated pseudo-momentum flux does not vary much, I show here only the psuedo-momentum flux of the four topography sensitivity experiments in a transect at $37° N$ in Fig. A.1

As an important part of the effect of lee waves on the ocean state the diffusivity at 37° was also calculated for all topography sensitivity experiments at $37° N$. As with the pseudo-momentum flux, the differences between the four experiments remain small, but a comparison is shown in Fig. A.2

As mentioned in section 5.2 the largest differences in the diffusivity between the base and control experiments are found near the bottom, and here the control experiments exhibits the largest diffusivity contrary to what might have been expected. The diffusivity is increased in the interior rather than at the bottom as a result of the implementation of the lee wave module. This is documented in Fig. A.3, which shows the difference (*upper panel*) and relative difference (*lower panel*) in diffusivity

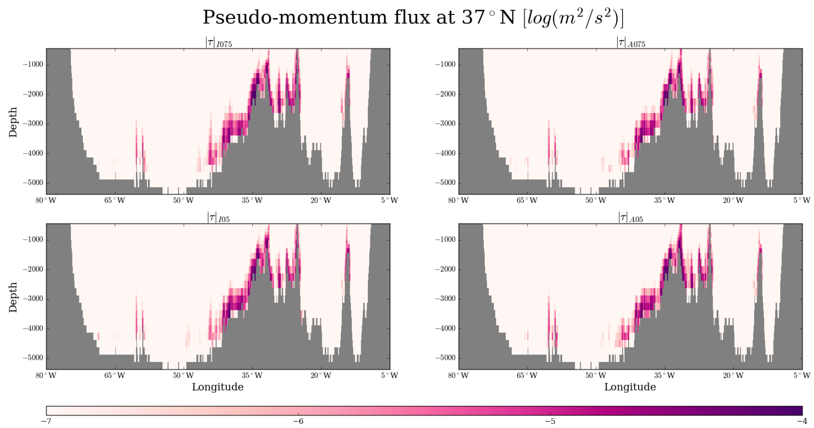

Figure A.1: The pseudo-momentum flux at 37°N for all four topography sensitivity experiments. Even though the bottom stress varies substantially between the four experiment, the variation of the stress is remarkably similar throughout the experiments.

at 37°N. While the largest numerical diffusivity difference occurs near the bottom, the interior displays a relative difference in diffusivity, which is far larger than that at the bottom. At several longitudes the relative difference is more than an order of magnitude larger in the control experiment. The patches of irregular diffusivity between 1500m depth and the surface mentioned in section 5.2 is rendered as negligible numerical differences. The important aspect of this figure, is the documentation of the large increase in diffusivity in the interior relative to that of the control experiment.

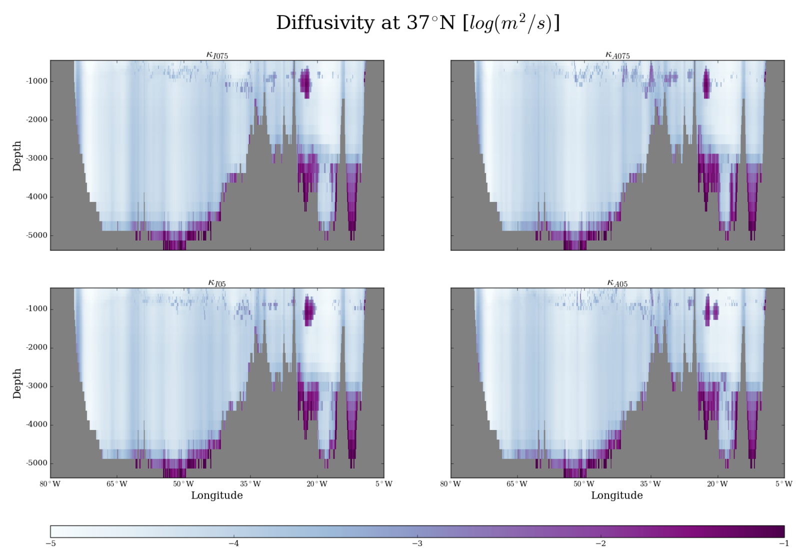

Figure A.2: The diffusivity at 37°N for all four topography sensitivity experiments. In all experiments are the diffusivity in the interior of magnitude $10^{-4} m^2/s$ at many longitudes.

Diffusivity at 37 ° N

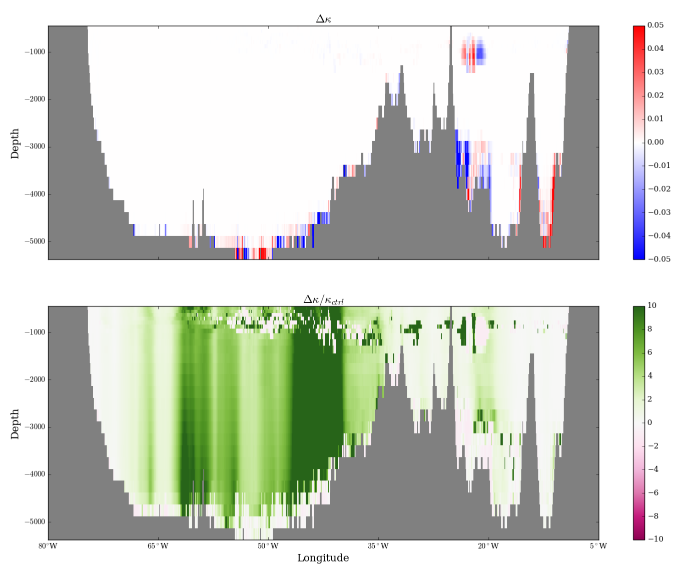

Figure A.3: The difference (*upper panel*) and relative difference (*lower panel*) in diffusivity between the base and control experiment at 37° N. Even though the largest numerical differences are near the bottom, it is clear how in the interior the diffusivity is increased by a factor of 10 or more in the base experiment.

List of Figures

Bibliography

Aguilar, D. and Sutherland, B. (2006). Internal wave generation from rough topography. *Physics of Fluids*, 18(6):066603.

Alford, M. H. (2001). Internal swell generation: The spatial distribution of energy flux from the wind to mixed layer near-inertial motions. *Journal of Physical Oceanography*, 31(8):2359–2368.

Andrews, D. and Mcintyre, M. E. (1976). Planetary waves in horizontal and vertical shear: The generalized eliassen-palm relation and the mean zonal acceleration. *Journal of the Atmospheric Sciences*, 33(11):2031–2048.

Arakawa, A. and Lamb, V. R. (1977). Computational design of the basic dynamical processes of the ucla general circulation model. *General circulation models of the atmosphere*, 17(Supplement C):173–265.

Bell, T. (1975). Topographically generated internal waves in the open ocean. *Journal of Geophysical Research*, 80(3):320–327.

Boyd, J. P. (1976). The noninteraction of waves with the zonally averaged flow on a spherical earth and the interrelationships on eddy fluxes of energy, heat and momentum. *Journal of the Atmospheric Sciences*, 33(12):2285–2291.

Brearley, J. A., Sheen, K. L., Naveira Garabato, A. C., Smeed, D. A., and Waterman, S. (2013). Eddy-induced modulation of turbulent dissipation over rough topography in the southern ocean. *Journal of Physical Oceanography*, 43(11):2288–2308.

Bryan, K. and Lewis, L. (1979). A water mass model of the world ocean. *Journal of Geophysical Research: Oceans*, 84(C5):2503–2517.

Cacchione, D., Pratson, L. F., and Ogston, A. (2002). The shaping of continental slopes by internal tides. *Science*, 296(5568):724–727.

Cairns, J. L. and Williams, G. O. (1976). Internal wave observations from a midwater float, 2. *Journal of Geophysical Research*, 81(12):1943–1950.

Cummins, P. F., Holloway, G., and Gargett, E. (1990). Sensitivity of the gfdl ocean general circulation model to a parameterization of vertical diffusion. *Journal of Physical Oceanography*, 20(6):817–830.

Cusack, J. M., Naveira Garabato, A. C., Smeed, D. A., and Girton, J. B. (2017). Observation of a large lee wave in the drake passage. *Journal of Physical Oceanography*, 47(4):793–810.

Danabasoglu, G., Yeager, S. G., Bailey, D., Behrens, E., Bentsen, M., Bi, D., Biastoch, A., Böning, C., Bozec, A., Canuto, V. M., et al. (2014). North atlantic simulations in coordinated ocean-ice reference experiments phase ii (core-ii). part i: mean states. *Ocean Modelling*, 73:76–107.

D'Asaro, E. A. (1985). The energy flux from the wind to near-inertial motions in the surface mixed layer. *Journal of Physical Oceanography*, 15(8):1043–1059.

De Lavergne, C., Madec, G., Le Sommer, J., Nurser, A. G., and Naveira Garabato, A. C. (2016). The impact of a variable mixing efficiency on the abyssal overturning. *Journal of Physical Oceanography*, 46(2):663–681.

Eden, C. and Greatbatch, R. J. (2008). Towards a mesoscale eddy closure. *Ocean Modelling*, 20(3):223–239.

Eden, C. and Olbers, D. (2014). An energy compartment model for propagation, nonlinear interaction, and dissipation of internal gravity waves. *Journal of Physical Oceanography*, 44(8):2093–2106.

Eden, C. and Olbers, D. (2017). A closure for internal wave–mean flow interaction. part ii: Wave drag. *Journal of Physical Oceanography*, 47(6):1403–1412.

Eden, C., Pollmann, F., and Olbers, D. (2019). Numerical evaluation of energy transfers in internal gravity wave spectra of the ocean. *Journal of Physical Oceanography*, 49(3):737–749.

Ferrari, R. and Wunsch, C. (2009). Ocean circulation kinetic energy: Reservoirs, sources, and sinks. *Annual Review of Fluid Mechanics*, 41.

Garner, S. T. (2005). A topographic drag closure built on an analytical base flux. *Journal of Atmospheric Sciences*, 62(7):2302–2315.

Garrett, C. and Munk, W. (1972). Space-time scales of internal waves. *Geophysical & Astrophysical Fluid Dynamics*, 3(1):225–264.

Garrett, C. and Munk, W. (1975). Space-time scales of internal waves: A progress report. *Journal of Geophysical Research*, 80(3):291–297.

Gaspar, P., Grégoris, Y., and Lefevre, J.-M. (1990). A simple eddy kinetic energy model for simulations of the oceanic vertical mixing: Tests at station papa and long-term upper ocean study site. *Journal of Geophysical Research: Oceans*, 95(C9):16179–16193.

Gent, P. R. and McWilliams, J. C. (1990). Isopycnal mixing in ocean circulation models. *Journal of Physical Oceanography*, 20(1):150–155.

Gill, A. (1984). On the behavior of internal waves in the wakes of storms. *Journal of Physical Oceanography*, 14(7):1129–1151.

Goff, J. A. (2010). Global prediction of abyssal hill root-mean-square heights from small-scale altimetric gravity variability. *Journal of Geophysical Research: Solid Earth*, 115(B12).

Goff, J. A. and Arbic, B. K. (2010). Global prediction of abyssal hill roughness statistics for use in ocean models from digital maps of paleo-spreading rate, paleo-ridge orientation, and sediment thickness. *Ocean Modelling*, 32(1-2):36–43.

Goff, J. A. and Jordan, T. H. (1988). Stochastic Modeling of Seafloor Morphology: Inversion of Sea Beam Data for Second-Order Statistics. *Journal of Geophysical Research: Solid Earth*, 93(B11):13589–13608.

Hall, M. M. and Bryden, H. L. (1982). Direct estimates and mechanisms of ocean heat transport. *Deep Sea Research Part A. Oceanographic Research Papers*, 29(3):339–359.

Hallberg, R. (2013). Using a resolution function to regulate parameterizations of oceanic mesoscale eddy effects. *Ocean Modelling*, 72:92–103.

Hasselmann, K. (1967). Weak-interaction theory of ocean waves. *Schriftenreihe Schiffbau*.

Henyey, F. S., Wright, J., and Flatté, S. M. (1986). Energy and action flow through the internal wave field: An eikonal approach. *Journal of Geophysical Research: Oceans*, 91(C7):8487–8495.

Hogan, P. J. and Hurlburt, H. E. (2000). Impact of upper ocean–topographical coupling and isopycnal outcropping in japan/east sea models with 1/8 to 1/64 resolution. *Journal of Physical Oceanography*, 30(10):2535–2561.

Jayne, S. R. (2009). The impact of abyssal mixing parameterizations in an ocean general circulation model. *Journal of Physical Oceanography*, 39(7):1756–1775.

Jayne, S. R. and St. Laurent, L. C. (2001). Parameterizing tidal dissipation over rough topography. *Geophysical Research Letters*, 28(5):811–814.

Jiang, J., Lu, Y., and Perrie, W. (2005). Estimating the energy flux from the wind to ocean inertial motions: The sensitivity to surface wind fields. *Geophysical research letters*, 32(15).

Jochum, M. and Eden, C. (2015). The connection between southern ocean winds, the atlantic meridional overturning circulation, and indo-pacific upwelling. *Journal of Climate*, 28(23):9250–9257.

Johnson, G. C. and Bryden, H. L. (1989). On the size of the antarctic circumpolar current. *Deep Sea Research Part A. Oceanographic Research Papers*, 36(1):39–53.

Klymak, J. M. (2018). Nonpropagating form drag and turbulence due to stratified flow over large-scale abyssal hill topography. *Journal of Physical Oceanography*, 48(10):2383–2395.

Köhler, J., Mertens, C., Walter, M., Stöber, U., Rhein, M., and Kanzow, T. (2014). Variability in the internal wave field induced by the atlantic deep western boundary current at 16° n. *Journal of physical oceanography*, 44(2):492–516.

Koszalka, I. M., Haine, T. W., and Magaldi, M. G. (2017). Mesoscale mixing of the denmark strait overflow in the irminger basin. *Ocean Modelling*, 112:90–98.

Kuhlbrodt, T., Griesel, A., Montoya, M., Levermann, A., Hofmann, M., and Rahmstorf, S. (2007). On the driving processes of the atlantic meridional overturning circulation. *Reviews of Geophysics*, 45(2).

Kunze, E. and Smith, S. L. (2004). The role of small-scale topography in turbulent mixing of the global ocean. *Oceanography*, 17(1):55–64.

Ledwell, J., Montgomery, E., Polzin, K., Laurent, L. S., Schmitt, R., and Toole, J. (2000). Evidence for enhanced mixing over rough topography in the abyssal ocean. *Nature*, 403(6766):179–182.

Ledwell, J. R., Watson, A. J., and Law, C. S. (1993). Evidence for slow mixing across the pycnocline from an open-ocean tracer-release experiment. *Nature*, 364(6439):701–703.

Ledwell, J. R., Watson, A. J., and Law, C. S. (1998). Mixing of a tracer in the pycnocline. *Journal of Geophysical Research: Oceans*, 103(C10):21499–21529.

Legg, S. (2021). Mixing by oceanic lee waves. *Annual Review of Fluid Mechanics*, 53:173–201.

Legg, S., Briegleb, B., Chang, Y., Chassignet, E. P., Danabasoglu, G., Ezer, T., Gordon, A. L., Griffies, S., Hallberg, R., Jackson, L., et al. (2009). Improving oceanic overflow representation in climate models: the gravity current entrainment climate process team. *Bulletin of the American Meteorological Society*, 90(5):657–670.

Leichter, J. J., Stewart, H. L., and Miller, S. L. (2003). Episodic nutrient transport to florida coral reefs. *Limnology and Oceanography*, 48(4):1394–1407.

Lvov, Y. V. and Tabak, E. G. (2001). Hamiltonian formalism and the garrett-munk spectrum of internal waves in the ocean. *Physical review letters*, 87(16):168501.

MacKinnon, J. (2013). Mountain waves in the deep ocean. *Nature*, 501(7467):321–322.

MacKinnon, J., Alford, M. H., Sun, O., Pinkel, R., Zhao, Z., and Klymak, J. (2013). Parametric subharmonic instability of the internal tide at 29 n. *Journal of Physical Oceanography*, 43(1):17–28.

MacKinnon, J. A., Zhao, Z., Whalen, C. B., Waterhouse, A. F., Trossman, D. S., Sun, O. M., St. Laurent, L. C., Simmons, H. L., Polzin, K., Pinkel, R., et al. (2017). Climate process team on internal wave–driven ocean mixing. *Bulletin of the American Meteorological Society*, 98(11):2429–2454.

Marshall, D. P. and Adcroft, A. J. (2010). Parameterization of ocean eddies: Potential vorticity mixing, energetics and arnold's first stability theorem. *Ocean Modelling*, 32(3-4):188–204.

Marshall, D. P. and Naveira Garabato, A. C. (2008). A conjecture on the role of bottom-enhanced diapycnal mixing in the parameterization of geostrophic eddies. *Journal of Physical Oceanography*, 38(7):1607–1613.

McComas, C. (1977). Equilibrium mechanisms within the oceanic internal wave field. *Journal of Physical Oceanography*, 7(6):836–845.

McComas, C. H. and Bretherton, F. P. (1977). Resonant interaction of oceanic internal waves. *Journal of Geophysical Research*, 82(9):1397–1412.

McComas, C. H. and Müller, P. (1981). Time scales of resonant interactions among oceanic internal waves. *Journal of physical oceanography*, 11(2):139–147.

McDougall, T. J. (2003). Potential enthalpy: A conservative oceanic variable for evaluating heat content and heat fluxes. *Journal of Physical Oceanography*, 33(5):945–963.

Melet, A., Hallberg, R., Adcroft, A., Nikurashin, M., and Legg, S. (2015). Energy flux into internal lee waves: Sensitivity to future climate changes using linear theory and a climate model. *Journal of Climate*, 28(6):2365–2384.

Melet, A., Hallberg, R., Legg, S., and Nikurashin, M. (2014). Sensitivity of the ocean state to lee wave–driven mixing. *Journal of Physical Oceanography*, 44(3):900–921.

Meyer, A., Polzin, K. L., Sloyan, B. M., and Phillips, H. E. (2015a). Internal waves and mixing near the kerguelen plateau. *Journal of Physical Oceanography*, 46(2):417–437.

Meyer, A., Sloyan, B. M., Polzin, K. L., Phillips, H. E., and Bindoff, N. L. (2015b). Mixing variability in the southern ocean. *Journal of Physical Oceanography*, 45(4):966–987.

Müller, P. and Natarov, A. (2003). The internal wave action model (iwam). In *Proceedings, Aha Huliko'a Hawaiian Winter Workshop, School of Ocean and Earth Science and Technology, Special Publication*, pages 95–105. Citeseer.

Munday, D. R., Johnson, H. L., and Marshall, D. P. (2013). Eddy saturation of equilibrated circumpolar currents. *Journal of Physical Oceanography*, 43(3):507–532.

Munk, W. and Wunsch, C. (1998). Abyssal recipes ii: Energetics of tidal and wind mixing. *Deep-sea research. Part I, Oceanographic research papers*, 45(12):1977–2010.

Munk, W. H. (1966). Abyssal recipes. *Deep Sea Research and Oceanographic Abstracts*, 13(4):707 – 730.

Naveira Garabato, A. C., Polzin, K. L., King, B. A., Heywood, K. J., and Visbeck, M. (2004). Widespread intense turbulent mixing in the southern ocean. *Science*, 303(5655):210–213.

Nikurashin, M. and Ferrari, R. (2010a). Radiation and dissipation of internal waves generated by geostrophic motions impinging on small-scale topography: Application to the southern ocean. *Journal of Physical Oceanography*, 40(9):2025–2042.

Nikurashin, M. and Ferrari, R. (2010b). Radiation and dissipation of internal waves generated by geostrophic motions impinging on small-scale topography: Theory. *Journal of Physical Oceanography*, 40(5):1055–1074.

Nikurashin, M. and Ferrari, R. (2011). Global energy conversion rate from geostrophic flows into internal lee waves in the deep ocean. *Geophysical Research Letters*, 38(8).

Nikurashin, M. and Ferrari, R. (2013). Overturning circulation driven by breaking internal waves in the deep ocean. *Geophysical Research Letters*, 40(12):3133–3137.

Nikurashin, M., Vallis, G. K., and Adcroft, A. (2013). Routes to energy dissipation for geostrophic flows in the southern ocean. *Nature Geoscience*, 6(1):48–51.

Nycander, J. (2005). Generation of internal waves in the deep ocean by tides. *Journal of Geophysical Research: Oceans*, 110(C10).

Nycander, J. (2011). Energy conversion, mixing energy, and neutral surfaces with a nonlinear equation of state. *Journal of Physical Oceanography*, 41(1):28–41.

Oakey, N. (1982). Determination of the rate of dissipation of turbulent energy from simultaneous temperature and velocity shear microstructure measurements. *Journal of Physical Oceanography*, 12(3):256–271.

Olbers, D. and Eden, C. (2013). A global model for the diapycnal diffusivity induced by internal gravity waves. *Journal of Physical Oceanography*, 43(8):1759–1779.

Olbers, D. and Eden, C. (2017). A closure for internal wave–mean flow interaction. part i: Energy conversion. *Journal of Physical Oceanography*, 47(6):1389–1401.

Olbers, D., Willebrand, J., and Eden, C. (2012). *Ocean dynamics*. Springer Science & Business Media.

Olbers, D. J. (1976). Nonlinear energy transfer and the energy balance of the internal wave field in the deep ocean. *Journal of Fluid mechanics*, 74(2):375–399.

Osborn, T. R. and Cox, C. S. (1972). Oceanic fine structure. *Geophysical & Astrophysical Fluid Dynamics*, 3(1):321–345.

Palmer, T., Shutts, G., and Swinbank, R. (1986). Alleviation of a systematic westerly bias in general circulation and numerical weather prediction models through an orographic gravity wave drag parametrization. *Quarterly Journal of the Royal Meteorological Society*, 112(474):1001–1039.

Pedlosky, J. (2013). *Ocean circulation theory*. Springer Science & Business Media.

Pollmann, F. (2020). Global characterization of the ocean's internal wave spectrum. *Journal of Physical Oceanography*, 50(7):1871–1891.

Pollmann, F., Eden, C., and Olbers, D. (2017). Evaluating the global internal wave model idemix using finestructure methods. *Journal of Physical Oceanography*, 47(9):2267–2289.

Polzin, K., Toole, J., Ledwell, J., and Schmitt, R. (1997). Spatial variability of turbulent mixing in the abyssal ocean. *Science*, 276(5309):93–96.

Polzin, K. L. and Lvov, Y. V. (2011). Toward regional characterizations of the oceanic internal wavefield. *Reviews of geophysics*, 49(4).

Polzin, K. L., Toole, J. M., and Schmitt, R. W. (1995). Finescale parameterizations of turbulent dissipation. *Journal of physical oceanography*, 25(3):306–328.

Richardson, L. F. (1920). The supply of energy from and to atmospheric eddies. *Proceedings of the Royal Society of London. Series A, Containing Papers of a Mathematical and Physical Character*, 97(686):354–373.

Rimac, A., Von Storch, J.-S., and Eden, C. (2016). The total energy flux leaving the ocean's mixed layer. *Journal of Physical Oceanography*, 46(6):1885–1900.

Rimac, A., von Storch, J.-S., Eden, C., and Haak, H. (2013). The influence of high-resolution wind stress field on the power input to near-inertial motions in the ocean. *Geophysical Research Letters*, 40(18):4882–4886.

Rintoul, S. R. and Garabato, A. C. N. (2013). Dynamics of the southern ocean circulation. In *International Geophysics*, volume 103, pages 471–492. Elsevier.

Russell, J. L., Dixon, K. W., Gnanadesikan, A., Stouffer, R. J., and Toggweiler, J. (2006). The southern hemisphere westerlies in a warming world: Propping open the door to the deep ocean. *Journal of Climate*, 19(24):6382–6390.

Sarkar, S. and Scotti, A. (2017). From topographic internal gravity waves to turbulence. *Annual Review of Fluid Mechanics*, 49:195–220.

Scott, R., Goff, J., Naveira Garabato, A., and Nurser, A. (2011). Global rate and spectral characteristics of internal gravity wave generation by geostrophic flow over topography. *Journal of Geophysical Research: Oceans*, 116(C9).

Sheen, K., Brearley, J., Naveira Garabato, A. C., Smeed, D., Waterman, S., Ledwell, J. R., Meredith, M. P., St. Laurent, L., Thurnherr, A. M., Toole, J. M., et al. (2013). Rates and mechanisms of turbulent dissipation and mixing in the southern ocean: Results from the diapycnal and isopycnal mixing experiment in the southern ocean (dimes). *Journal of Geophysical Research: Oceans*, 118(6):2774–2792.

Smith, R. B. (1989). Mountain-induced stagnation points in hydrostatic flow. *Tellus A: Dynamic Meteorology and Oceanography*, 41(3):270–274.

Smyth, W., Moum, J., and Caldwell, D. (2001). The efficiency of mixing in turbulent patches: Inferences from direct simulations and microstructure observations. *Journal of Physical Oceanography*, 31(8):1969–1992.

St. Laurent, L., Naveira Garabato, A. C., Ledwell, J. R., Thurnherr, A. M., Toole, J. M., and Watson, A. J. (2012). Turbulence and diapycnal mixing in drake passage. *Journal of Physical Oceanography*, 42(12):2143–2152.

Stommel, H. (1961). Thermohaline convection with two stable regimes of flow. *Tellus*, 13(2):224–230.

Talley, L. D. (2013). Closure of the global overturning circulation through the indian, pacific, and southern oceans: Schematics and transports. *Oceanography*, 26(1):80–97.

Teixeira, M. A. (2014). The physics of orographic gravity wave drag. *Frontiers in Physics*, 2:43.

Toggweiler, J. (2009). Shifting westerlies. *Science*, 323(5920):1434–1435.

Toggweiler, J. and Key, R. (2003). Ocean circulation| thermohaline circulation. encyclopedia of atmospheric sciences, 1549–1555.

Toggweiler, J. and Samuels, B. (1995). Effect of drake passage on the global thermohaline circulation. *Deep Sea Research Part I: Oceanographic Research Papers*, 42(4):477–500.

Trossman, D. S., Arbic, B. K., Garner, S. T., Goff, J. A., Jayne, S. R., Metzger, E. J., and Wallcraft, A. J. (2013). Impact of parameterized lee wave drag on the energy budget of an eddying global ocean model. *Ocean Modelling*, 72:119–142.

Watanabe, M. and Hibiya, T. (2002). Global estimates of the wind-induced energy flux to inertial motions in the surface mixed layer. *Geophysical research letters*, 29(8):64–1.

Waterman, S., Naveira Garabato, A. C., and Polzin, K. L. (2013). Internal waves and turbulence in the antarctic circumpolar current. *Journal of Physical Oceanography*, 43(2):259–282.

Waterman, S., Polzin, K. L., Naveira Garabato, A. C., Sheen, K. L., and Forryan, A. (2014). Suppression of internal wave breaking in the antarctic circumpolar current near topography. *Journal of Physical Oceanography*, 44(5):1466–1492.

Whittaker, J. M., Goncharov, A., Williams, S. E., Müller, R. D., and Leitchenkov, G. (2013). Global sediment thickness data set updated for the australian-antarctic southern ocean. *Geochemistry, Geophysics, Geosystems*, 14(8):3297–3305.

Wong, S. H., Santoro, A. E., Nidzieko, N. J., Hench, J. L., and Boehm, A. B. (2012). Coupled physical, chemical, and microbiological measurements suggest a connection between internal waves and surf zone water quality in the southern california bight. *Continental Shelf Research*, 34:64–78.

Wright, C. J., Scott, R. B., Ailliot, P., and Furnival, D. (2014). Lee wave generation rates in the deep ocean. *Geophysical Research Letters*, 41(7):2434–2440.

Wunsch, C. (1975). Internal tides in the ocean. *Reviews of Geophysics*, 13(1):167–182.

Wunsch, C. and Ferrari, R. (2004). Vertical mixing, energy, and the general circulation of the oceans. *Annual Review of Fluid Mechanics*, 36(1):281–314.

Yang, L., Nikurashin, M., Hogg, A. M., and Sloyan, B. M. (2018). Energy loss from transient eddies due to lee wave generation in the southern ocean. *Journal of Physical Oceanography*, 48(12):2867–2885.

Young, W. R. (2010). Dynamic enthalpy, conservative temperature, and the seawater boussinesq approximation. *Journal of physical oceanography*, 40(2):394–400.